FUNDAMENTAL AND QUANTITATIVE ANALYSIS OF GAS-PHASE PROTEIN STRUCTURE AND STRUCTURAL TRANSITIONS USING ION MOBILITY-MASS SPECTROMETRY

by

MICAH DONOR

A DISSERTATION

Presented to the Department of Chemistry and Biochemistry
and the Graduate School of the University of Oregon
in partial fulfillment of the requirements
for the degree of
Doctor of Philosophy

June 2020

DISSERTATION APPROVAL PAGE

Student: Micah Donor

Title: Fundamental and Quantitative Analysis of Gas-Phase Protein Structure and Structural Transitions using Ion Mobility-Mass Spectrometry

This dissertation has been accepted and approved in partial fulfillment of the requirements for the Doctor of Philosophy degree in the Department of Chemistry and Biochemistry by:

Georgy Nazin	Chairperson
James Prell	Advisor
Marina Guenza	Core Member
Anne Zemper	Institutional Representative

and

Kate Mondloch	Vice Provost and Dean of the Graduate School

Original approval signatures are on file with the University of Oregon Graduate School.

Degree awarded June 2020

© 2020 Micah Donor

DISSERTATION ABSTRACT

Micah Donor

Doctor of Philosophy

Department of Chemistry and Biochemistry

June 2020

Title: Fundamental and Quantitative Analysis of Gas-Phase Protein Structure and Structural Transitions using Ion Mobility-Mass Spectrometry

Ion mobility-mass spectrometry has become a capable, powerful tool for studying biomolecular structure and interactions. Preservation of weak non-covalent interactions into the gas phase via electrospray ionization has enabled native mass spectrometry investigations of protein complexes and protein-ligand systems. The coupling of mass spectrometry with ion mobility has allowed measurement of ion size and shape alongside mass. In addition, methods to obtain quantitative energetic information for many systems of moderate size have been introduced. However, the large size, structural dispersity, and conformational flexibility of proteins have greatly limited quantitative studies of their properties using extant methods. An additional contributing factor to this gap in knowledge has been an incomplete understanding of several mechanisms and processes commonly used in ion mobility-mass spectrometry analysis of proteins. These gaps in understanding have, in turn, constrained the range of systems and processes amenable to investigation. Introduction of creative new approaches will continue to expand the set of biological questions addressable by mass spectrometry methods.

Here, novel quantitative methods are developed and used to study the gas-phase structures and structural transitions of proteins, yielding fundamental insights into key gas-phase processes. First, the structures of highly-extended protein ions produced by supercharging electrospray ionization are found to be one-dimensional, and mechanistic insights into supercharging are obtained. Focus is then shifted to manipulating protein structure in the gas phase. The energy scales of two methods that can unfold proteins in the gas phase, collisional and surface activation, are calibrated and the efficiencies of each process studied. Surface activation is found to be much more efficient for larger proteins, and its efficiency is highly dependent on structure. Next, a method for determining activation energies for protein unfolding is introduced. Energies for protein unfolding are found to support the mobile proton model as the universal gas-phase unfolding mechanism. Lastly, the energetics of non-specific binding of lipid head groups to soluble proteins are probed.

This dissertation included previously published and unpublished co-authored material.

CURRICULUM VITAE

NAME OF AUTHOR: Micah Donor

GRADUATE AND UNDERGRADUATE SCHOOLS ATTENDED:

University of Oregon, Eugene
George Fox University

DEGREES AWARDED:

Doctor of Philosophy, Chemistry, 2020, University of Oregon
Bachelor of Science, Chemistry, 2014, George Fox University

AREAS OF SPECIAL INTEREST:

Native Mass Spectrometry
Ion Mobility
Method Development
Ion Energetics
Protein Structure

PROFESSIONAL EXPERIENCE:

Graduate Teaching Fellow, Department of Chemistry and Biochemistry, University of Oregon, 2014-2016, 2019-present

Graduate Research Fellow, Institute for Health in the Built Environment, University of Oregon, 2019

Graduate Research Fellow, Department of Chemistry and Biochemistry, University of Oregon, 2016-2019

GRANTS, AWARDS, AND HONORS:

Graduate Research Fellowship Award, National Science Foundation, 2016-2019

Outstanding Chemistry Student Award, George Fox University, 2014

Dick Van Santen Award, ACS Portland Section, 2013

PUBLICATIONS:

Donor, M. T.; Shepherd, S. A.; Prell, J. S. Rapid Determination of Activation Energies for Gas-Phase Protein Unfolding and Dissociation in a Q-IM-ToF Mass Spectrometer. *J. Am. Soc. Mass Spectrom.* **2020**, *31*, 602-610.

Donor, M. T.; Mroz, A. M.; Prell, J. S. Experimental and Theoretical Investigation of Overall Energy Deposition in Surface-Induced Unfolding of Protein Ions. *Chem. Sci.* **2019**, *10,* 4097-4106.

Donor, M. T.; Ewing, S. A.; Zenaidee, M. A.; Donald, W. A.; Prell, J. S. Extended Protein Ions are Formed by the Chain Ejection Model in Chemical Supercharging Electrospray Ionization. *Anal. Chem.* **2017**, *89*, 5107-5114.

Ewing, S. A.; Donor, M. T.; Wilson, J. W.; Prell, J. S. Collidoscope: An Improved Tool for Computing Collisional Cross-Sections with the Trajectory Method. *J. Am. Soc. Mass Spectrom.* **2017**, *28*, 587-596.

Wheeler, L. C.; Donor, M. T.; Prell, J. S.; Harms, M. J. Multiple Evolutionary Origins of Ubiquitous Cu2+ and Zn2+ Binding in the S100 Protein Family. *PLoS ONE.* **2016**, *11*, e0164740.

Bailey, T. S.; Donor, M. T.; Naughton, S. P.; Pluth, M. D. A simple bioluminescent method for measuring D-amino acid oxidase activity. *Chem. Commun*. **2015**, *51*, 5425-5428.

ACKNOWLEDGMENTS

First, I would like to thank my advisor, Dr. Jim Prell, for his patient mentorship, for enthusiastic scientific discussions, for helpful feedback in the writing of this and other manuscripts, and for challenging me to become a better scientist. I am grateful to the members of my doctoral committee, Drs. George Nazin, Marina Guenza, and Anne Zemper, for their constructive feedback and their contributions to my academic and professional development. I must express my appreciation for the contributions of several collaborators, as well as many current and former members of the Prell lab, which were invaluable to the completion of this work. I would like to thank all the members of the Prell lab for cultivating a supportive, tight-knit, collegial culture from the start, and the Wong lab for their part in creating a fun and vibrant office atmosphere. This research was supported in part by a National Science Foundation Graduate Research Fellowship, DGE-1309047, and by a grant to Dr. Jim Prell from the National Institutes of Health, R21AI125804. The content is solely the responsibility of the author and does not necessarily represent the official views of the National Science Foundation or the National Institutes of Health.

I would be remiss if I neglected to thank all the friends and family who have walked alongside me through the highs and lows of graduate school. I wish to express special thanks to the past and present members of the UO Graduate Christian Fellowship and Emmaus Life Church. I will be forever indebted to my parents for all the ways they have shaped me into the person I am today, as well as for their incisive advice and unfailing care. Lastly, I am profoundly thankful for my wonderful wife, Tai, and for her constant love and support. Further up and further in!

TABLE OF CONTENTS

LIST OF FIGURES

Figure Page

Figure Page

Figure Page

LIST OF TABLES

Table Page

CHAPTER I

INTRODUCTION

Over the past several decades, mass spectrometry (MS) has become one of the most important techniques for analysis of biomolecules. Small sample requirements, short acquisition times, and the ability to identify multiple species within a single sample have been critical to the development of fields such as proteomics,[1] metabolomics,[2] and lipidomics.[3] Hydrogen/deuterium exchange and other labeling techniques have enabled the study of protein structure and dynamics with up to 100% sequence coverage and the ability to distinguish between local and global fluctuations.[4,5] In order to analyze large biomolecules such as proteins, conventional MS approaches include a digestion step that cuts the protein into smaller pieces. These peptides can be analyzed rapidly with MALDI-MS or LC-MS, which are now extremely common tools in the bioanalytical chemistry arsenal (Figure 1).[6] Studying intact proteins can streamline sample preparation and reduce disruption of structures and interactions prior to analysis, a necessary feature for studying high-order structure and other non-covalent or weak covalent interactions.[7] Recent advances in MS instrumentation have made intact protein MS methods, such as top-down sequencing, practical in an ever-growing set of cases.[8,9] Many of these methods utilize conditions that denature proteins in solution (Figure 1). In contrast, native MS seeks to maintain high-order structure into the gas phase by ionizing proteins from solutions near physiological pH and ionic strength (Figure 1).[10] The study of intact proteins using MS, particularly under native but also denaturing conditions, has been limited by gaps in our understanding of gas-phase protein structure and interactions, the effect of processes such as ionization on such characteristics, and limitations in the methods used to study them. For example, determining protein-protein or protein-ligand binding sites and energies or protein structural ensembles remains very challenging. This dissertation will relate my work on understanding the fundamental properties of proteins in the gas phase and developing novel methods to study them more informatively.

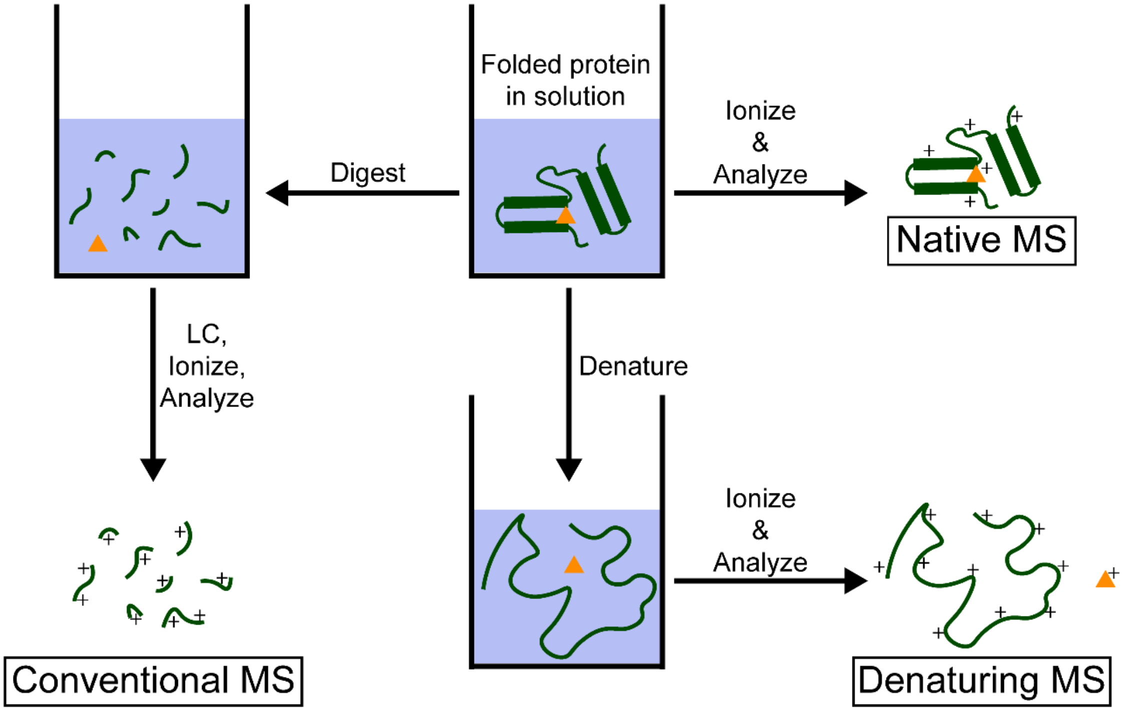

Figure 1. Illustration of conventional, denaturing, and native MS analysis of proteins. While conventional and denaturing MS methods excel at studying primary structure, native MS approaches have greater utility for investigating high-order structure.

Electrospray Ionization

The most common ionization method for mass spectrometry analysis of proteins, for both native and denaturing conditions, is electrospray ionization (ESI).[11] In ESI, a small amount of solution containing the analyte(s) of interest is placed within a capillary that tapers to a narrow tip. Electrical contact with the solution is created and a potential difference of several hundred to several thousand volts is applied, causing a fine plume of charged droplets to flow from the solution towards the entrance to the mass spectrometer, completing an electrical circuit. As the droplets traverse the distance and reach stages of the instrument held below atmospheric pressure, solvent (typically water, polar organics such as methanol or acetonitrile, or some mixture of the preceding) evaporates, causing the charge density of the droplets to increase. This continues until Coulombic repulsion overcomes the surface tension holding the droplets together,[12] at which point the droplet undergoes fission into smaller droplets and the cycle of evaporation followed by fission repeats.[13,14] Small ions or clusters of ions may also be emitted from the droplets, with the rate of emission determined by the interplay between solvation energy and field strength at the droplet surface.[15]

Three models have been proposed to explain ion charging in ESI, and each predominates in different circumstances. In the ion evaporation model (IEM),[15] as described above, ions are emitted from small, nanometer-scale droplets when the electric field at the surface of the droplet overcomes the solvation energy of the ion (Figure 2a).[16] For small ions, the IEM predominates.[14,17,18] However, for larger, hydrophilic species such as peptides and proteins with compact, folded structures (typically found in aqueous solutions), the IEM is not sufficient to explain the observed results. Instead, the charged residue model (CRM) has been proposed (Figure 2b).[19,20] In the CRM, water evaporates from the droplets, which undergo fission cycles until only a thin shell of water remains coating the analyte, which has stayed solvated within the interior of the droplet. At this stage, the remaining charges are transferred to the analyte and the last water molecules evaporate, leaving a bare analyte ion. The CRM predominates for peptides and proteins in native-like conditions.[21-24] Lastly, for analytes composed of long chains that are not well-solvated, such as polymers or denatured proteins, a third model, the chain ejection model (CEM) has been proposed (Figure 2c).[25,26] In the CEM, a portion of the analyte chain ventures outside of the (nanometer-sized) droplet, causing charge migration to the exposed portion and precipitating a stepwise extrusion process. The CEM is likely to be operative for ions that are too large to leave the droplet in a single evaporation event (ala the IEM) but have low solvation energies in the solvent system used and thus can reside at the liquid-vacuum interface.[25,26] The final charge on the ionized analyte is related to the mechanism by which ionization takes place, as well as the size and chemical composition of the analyte.[27]

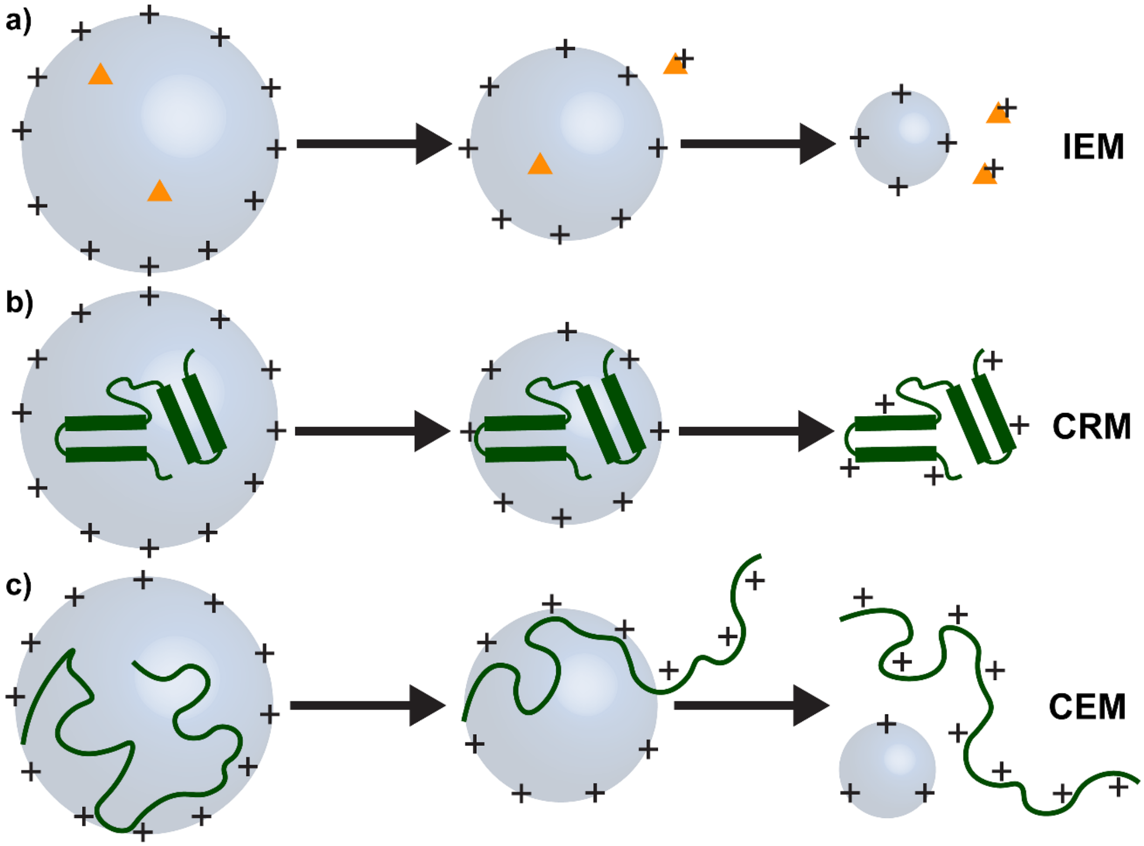

Figure 2. Illustration of three charging mechanisms in ESI. **(a)** ion evaporation model **(b)** charged residue model **(c)** chain ejection model.

Manipulating Charge in ESI

One important characteristic of ESI is that it produces a distribution of charge states for sufficiently large biomolecules. Both the solution conditions as well as the structure of the analyte can affect the extent of charging as well as the breadth of the distribution.[27,28] Characteristics such as resolution and sensitivity as well as the extent and quality of fragmentation/dissociation exhibit some charge state dependence.[29-32] In addition, structural information can often be inferred from the charge state distribution, such as the presence of multiple conformer families.[28,33-37] For proteins, the focus of my research, "native-like" solution conditions (i.e. aqueous solution near physiological pH and ionic strength) produce a low and narrow charge state distribution (Figure 3a). In contrast, denaturing the protein in solution leads to much higher charge states and a broad distribution (Figure 3b). Typically, low charge states correspond to compact, folded conformations, while high charge states correspond to partially or fully unfolded conformations.[36]

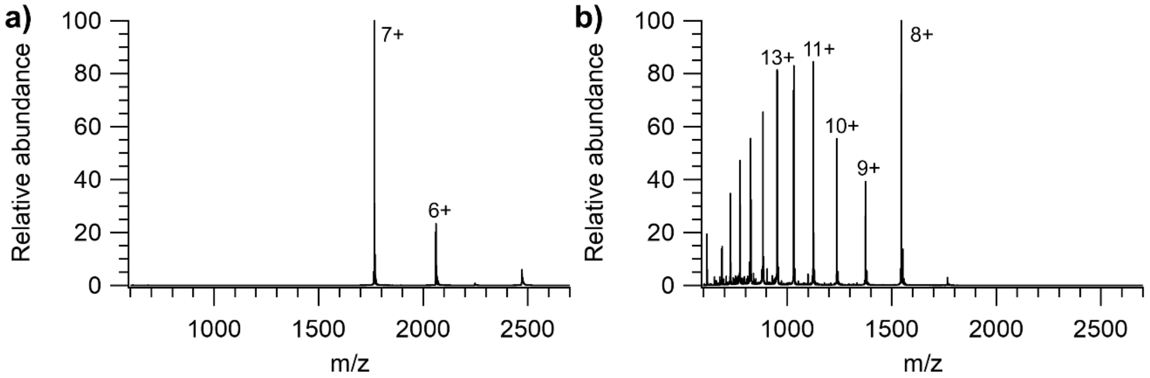

Figure 3. Example mass spectra for cytochrome C showing the effect of **(a)** native-like conditions, with low charge states and a narrow distribution, and **(b)** denaturing conditions, with higher charge states and a broader distribution.

Solution additives to either increase or decrease charging have been introduced. Charge-reducing reagents such as triethylammonium acetate (TEAA)[38] or imidazole derivatives[39] have moderate gas-phase basicities, enabling them to abstract protons and decrease the charge state of proteins. They can aid in preserving weak native-like interactions by increasing resistance to structural disruption,[40-42] which is typically more facile for higher charge states.[40]

Supercharging reagents, in contrast, increase charging in ESI. Chemical supercharging reagents are typically moderately polar organic compounds with low volatility.[43-46] Depending on the identity and concentration (typically <10% v/v) of supercharging reagent and the pH of the solution, the charge state distribution may shift higher by only a few charges or may even surpass the degree of charging for denaturing conditions.[47-50] Supercharging has been used to reduce non-specific adduction,[49] improve fragmentation efficiency,[51] and enable real-time hydrogen/deuterium exchange measurements.[52] However, there has been some dispute over the exact mechanism of supercharging.[43,53,54] As solvent evaporates, the concentration of supercharging reagent in the shrinking droplets will increase due to their low volatility.[43] The debate in the field is over the effect this change in droplet composition will have. One proposal is that the high concentration of organic supercharging reagent will cause chemical and thermal denaturation within the droplet.[44,55-58] The unfolded protein in the droplet will then be ionized by a similar mechanism to that for denatured proteins, likely to be a CEM-like process.[25] A second possibility is that the high concentration of supercharging reagent may shift the location of charges in the droplet from the surface to the interior, close to the protein, due to decreased charge transport.[54] Then, following evaporation of all remaining solvent, i.e., a CRM-like mechanism, the highly-charged protein undergoes a Coulombically-driven structural rearrangement.[54] Understanding the mechanism of supercharging is important for designing and interpreting the results of experiments utilizing the technique. Common to both proposed mechanisms are unfolded final protein ion structures. While the charge state distribution provides some structural information, it is also possible to directly measure ion size.

Ion Mobility

Ion mobility (IM) spectrometry is a complementary separation and analysis method that measures size and shape and can be coupled to mass spectrometry. IM separates ions based on their electrophoretic mobility in a neutral mobility gas such as helium or nitrogen.[59] The most common type of IM, drift tube IM, works by applying an electric potential across a tube filled with gas, at a pressure in the torr range. At the pressures and voltages used ions will quickly reach their terminal velocity. Larger ions experience more friction with the gas due to collisions, while ions with higher charge experience more force due to the potential difference. The result is that ions are separated based on their size to charge ratio.[59] An alternative IM method that is commonly used for protein analysis is traveling-wave IM.[60] Rather than a constant potential, traveling-wave IM uses a sinusoidal potential that moves faster than the ions.[60,61] In this method, the ions do not reach a stable velocity, but instead have periods of time being pulled along by the traveling wave before falling behind, followed by periods of low velocity or even moving in the reverse direction before the next peak of the wave catches up.[61]

Regardless of the approach used, IM provides an orthogonal separation method and is routinely used to separate ions that overlap in *m*/*z*. For example, a protein monomer will have the same *m*/*z* as a dimer with twice the charge, but the dimer will likely not be twice as big spatially, and thus IM will be able to separate the two despite their *m*/*z* overlap. At the cutting edge of IM, a recent report was able to distinguish between isotopomers (molecules differing only in the location of isotopic substitutions).[62] In addition to separating ions, IM can also be used to measure collisional cross section values (CCSs), which are analogous to surface area.[59] CCSs can also be predicted from high-resolution structures generated experimentally (via X-ray crystallography, cryogenic EM, or NMR) or computationally (via quantum mechanical or molecular dynamics calculations).[63-65] Thus, experimentally measured CCSs can be compared with those computed for high-resolution structures.[66] In some cases, this can enable assignment of a particular structure or structures.[67-69] However, for polymer chains, including biopolymers such as proteins and peptides, there may be many different conformations with very similar CCSs, complicating structural assignment.[70] Until recently, this problem went largely unaddressed. However, progress has been made towards understanding the scope of the issue and potential routes to amelioration. Several groups have generated many (hundreds to thousands) of conformers for peptide and protein systems exploring the conformational space and computed CCSs for each.[70] These data can then be used to attempt a reconstruction of the experimental CCS distribution, rather than only matching peak locations.[70] Similarly, CCS can be used to constrain the space of possible structures, often in concert with spectroscopic[71,72] or dissociation[73-75] data.

Scaling Laws

An alternative approach to extracting structural information from CCS or other data for a single analyte is to look for scaling laws – expressions describing how, e.g., the CCS of an ion changes with its mass. A globular, folded protein can be approximated by a sphere, for which surface area (i.e. CCS) is proportional to r^2, while mass (assuming constant density) is proportional to r^3. Thus, CCS should be proportional to $mass^{2/3}$ for globular proteins. The relationship between CCS and mass for native-like proteins has been investigated by several groups and an exponent very close to 2/3 found, providing evidence for globular, structures in the gas phase.[76,77] However, the structures of denatured or unfolded proteins, which can be extended, have received less attention to date.

The relationship of the extent of charging and mass has also been extensively studied for native-like proteins. According to the accepted model for ionization of native-like proteins, the CRM (described above), the charges on the protein ion originate from a thin shell of water (solvent) molecules surrounding the protein. Thus, the charge on the protein should be related to the charge on an equivalently-sized water (solvent) droplet. The Rayleigh limit, which describes the balance of forces between surface tension and Coulombic repulsion, predicts that charge should scale with the square root of mass for globular ions.[21] Experiments have found an exponent closer to 0.57, a slight deviation.[23,78] This deviation from the Rayleigh limit has been explained as arising from emission of small charge carriers from the droplets prior to complete evaporation.[79] This effect is greater for smaller proteins, leading to an exponent greater than 0.5.

The structures of polymers in the gas phase have also been studied using scaling laws, with enlightening results. A number of groups have demonstrated that polymers can adopt a range of structures ranging from globular (2/3 power CCS scaling) to stretched (linear CCS scaling) depending on the degree of polymerization and charge state.[80-82] In between these extremes, polymers fall into a series of self-similar groups following the same trend, with transitions between the groups.[80-82] This has been rationalized as the formation of a series of globular domains in which the polymer chain curls around a charge carrier (often an alkali metal ion) to reduce Coulomb repulsion, eventually leading to collapse into a quasi-globular structure.[81] The de Pauw group has used a similar methodology to investigate the apparent densities of observed polymer structural families, revealing that the ratio of apparent densities for adjacent families is roughly constant and devising a method of identifying structural anomalies.[83] These examples highlight the ways in which the study of scaling behavior can provide insight into ion structure, as well as charging mechanisms, in the absence of atomic-resolution data. In addition, the polymer studies illustrate one of the ways in which structural transitions can prove enlightening.

Gas-Phase Unfolding and Dissociation

Beyond studying static structures with IM-MS, there is great interest in perturbing or disrupting structures and probing the resulting changes. Understanding these changes can often provide a clearer picture of the overall structure and insight into dynamic processes. For proteins in particular, due to the link between structure and function,[84] gas-phase unfolding and dissociation have received recent attention.[85,86] IM-MS has the potential to sensitively and selectively investigate structural changes with the ability to more easily resolve intermediates and coexisting populations compared to more conventional techniques.[87] Much careful work has been performed demonstrating that proteins can be transferred into the gas phase via ESI with little disruption to their native structure.[66,71,88,89] In addition, while the relationship of the gas-phase unfolded structures to those produced in solution-phase unfolding is as of yet unclear, it has been shown, most prominently by the Ruotolo group, that gas-phase unfolding can yield useful structural information.[85,90]

Proteins can be unfolded in the gas phase by increasing their internal energy through a process termed activation (Figure 4). There are many different activation methods, which can be broadly divided into collision-,[91] electron-,[92,93] and photon-based.[94,95] The most common method is collisional activation, in which many energetic collisions with gas convert kinetic energy to internal energy of the ion.[91,96] When collisional activation produces a measurable size change, it is termed collision-induced unfolding (CIU).[85] For proteins, the number of transitions in CIU has been shown to be correlated with the number of domains.[37,90] CIU has also been used to distinguish between different disulfide bond patterns,[97] probe the relative stability of similar proteins or complexes,[97-99] and investigate ligand binding sites and allostery.[100,101] CIU experiments can be performed in minutes or less, making them amenable to high-throughput applications.

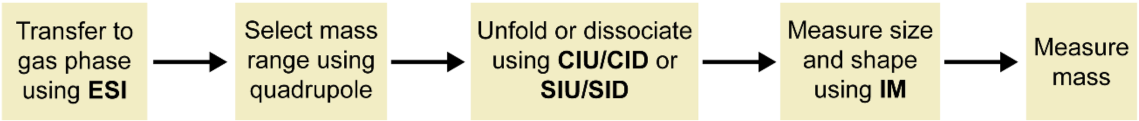

Figure 4. Typical IM-MS workflow for protein unfolding/dissociation. Ionization is followed by mass selection, activation, size measurement, and finally mass measurement.

Collisional activation can also be used to break noncovalent protein complexes into subcomplexes, a process termed collision-induced dissociation (CID). However, CID often disrupts the structure of the complex prior to dissociation, producing a highly charged, unfolded monomer and remaining (n-1)-mer.[40,102] Due to this, CID is not ideal for probing the topology of protein complexes. An alternative method, surface activation, activates ions by a single high-energy collision with a rigid surface.[103] Surface-induced dissociation (SID) of protein complexes, in contrast to CID, breaks the complex into pieces that reflect the overall topology of the complex.[104,105] For examples, while CID would produce monomer and trimer from a tetramer with a dimer-of-dimers architecture, SID would produce a pair of dimers.[104,106] The Wysocki group has shown that SID preferentially breaks the weakest interface (often the smallest) within a complex.[106,107] In addition, SID products often remain compact, allowing the structures of the subcomplexes to be probed.[42] A number of protein complexes, including membrane proteins, both with and without bound ligands, have been investigated using SID.[106,108-112] Recently, ultraviolet photodissociation (UVPD), in which ions are activated by absorption of high-energy photons, has been shown to produce SID-like dissociation products in some circumstances,[113] providing an additional method for studying protein complex architecture.

For all the methods discussed in this section, analyses performed to date on proteins have primarily been qualitative. The collision energies involved have not been related to the internal temperature of the ions, nor have thermodynamic quantities been obtained. While the information gained is valuable, developing the quantitative aspect of these techniques would enhance their usefulness significantly.

Quantitative Energetics Using Mass Spectrometry

Several methods for obtaining quantitative energetic information using mass spectrometry have been developed. Some of the more common ones will be surveyed here. In order to determine such quantitative information, the internal energy and survival yield of the reactant ion, as well as the reaction time, must be known or inferred. The ideal quantitative method allows for direct measurement and precise control of both temperature and reaction time. Blackbody Infrared Radiative Dissociation (BIRD)[114] possesses both of those characteristics. BIRD is implemented in an FT-ICR mass spectrometer, which traps ions and detects their characteristic *m*/*z*-dependent cyclotron frequency. The walls of the ion trap can be heated to a given temperature, and ion within the trap will be heated to the same temperature via absorption of blackbody photons emitted from the wall of the trap. The time between injection of ions into the trap and detection can be varied from milliseconds to many seconds, allowing precise determination of rate constants and therefore activation energies. BIRD has been applied to study the dissociation and fragmentation of numerous ions, from small molecules[115,116] and peptides[117,118] up to proteins[119] and protein complexes.[120,121] Depending on the size of the molecule, additional modeling may be necessary to represent the internal energy distribution and extract meaningful information from the data.[122] Proteins generally fall above the rapid energy exchange limit and thus equilibrate thermally prior to dissociation, simplifying the analysis.[122,123] However, BIRD has a number of limitations which have restricted widespread use. Due to the necessity of thermally equilibrating the ion trap, a full set of BIRD experiments takes a long time to complete, almost prohibitively so. In addition, large protein complexes are difficult to study using FT-ICR instruments, and the lack of a way to measure protein size and shape within the ion trap prevents the study of protein unfolding. Large protein complexes and protein unfolding are areas of particular current interest, and a method for studying them quantitatively would be of great value.

The temporal disadvantages of BIRD could be circumvented by using an alternative method of heating the ions, such as collisional activation (CID), a capability possessed by FT-ICR instruments. The Williams group has shown that ions activated in this way can be thought of as having an effective internal temperature and thus will follow thermally-activated unimolecular kinetics.[124] Determining the actual internal temperature is more complex and typically requires detailed modeling. The vibrational modes of the system are computed quantum mechanically and used in Rice-Ramsperger-Kassel-Marcus (RRKM) modeling to determine the activation energy that would give rise to the observed reaction rates.[125] Similar analysis approaches have been used to extract thermodynamic information from SID, which differs from CID in the collision partner (rigid surface vs. gas) and number of collisions (one vs. many), but likewise yields activated ions with an effective internal temperature in many cases.[126,127] Both CID and SID have been used to study the fragmentation of small molecules and peptides,[126-130] but the need to perform RRKM modeling, which remains intractable for large proteins, has limited their use to smaller systems. In addition, much like BIRD, they have not been implemented on a platform that allows for CCS measurement.

Another technique, one that shares features with both CID and SID, is guided ion beam mass spectrometry (GIBMS),[131] in which a single high-energy collision with a gas atom/molecule activates the ion, leading to fragmentation. This is accomplished by carefully controlling the pressure in the collision region; by controlling the kinetic energy of the ions before and after the collision the energy and reaction time can be determined. The survival yield of the original (precursor) ion can thus be related to the threshold energy for the fragmentation reaction. As with the above methods, GIBMS has been applied to study small molecules,[132] clusters,[133,134] and peptides.[135] GIBMS is even more limited by the size of the ion, however, as the larger the ion, the less efficient is energy transfer between the ion and gas. Additionally, due to the high vacuum environment required for GIBMS, coupling it with IM to allow for measurement of the energetics of structural transitions is not feasible.

In contrast to the gas-phase quantitation methods described above, it is also possible to use IM-MS as a detection method for thermal unfolding of proteins or other biomolecules in solution, specifically within the capillary immediately prior to ESI. This method was originally developed in the early days of native MS[136,137] but has enjoyed a recent resurgence.[138-143] In particular, the Clemmer group has used IM-MS to investigate the thermodynamics of unfolding for several proteins.[139-142] In some respects, this approach provides the best of both worlds. Unfolding occurs in solution, not the gas phase, and IM-MS is able to separate and identify multiple coexisting populations, potentially providing richer information than many conventional detection methods. However, the full effects of the ESI process on protein structure, as well as the exact relationship between structure and charge, are not understood, introducing a possible confounding factor. Partially unfolded or disordered proteins (IDPs) are more likely to exhibit anomalous behavior in ESI than are folded proteins, compounding that confounding effect. In addition, while these experiments are much faster than BIRD, they do not rise to the level of a high-throughput technique, unlike the gas-phase CIU described earlier. Thus, rapid quantitation of protein unfolding and dissociation remains an unaddressed need.

In this dissertation I describe my efforts to address several outstanding, fundamental questions in the field of ion mobility-mass spectrometry. The lack of quantitative analysis tools for gas-phase protein structure and structural transitions has limited both the quality and quantity of information that can be learned about larger, biologically-relevant biological systems using ion mobility-mass spectrometry. Similarly, lack of understanding of the fundamental mechanistic details of commonly used mass spectrometry techniques has also limited their applicability, and in particular has restricted their ability to elucidate subtle details of many important processes. In this dissertation I will describe my work in developing a fundamental and quantitative understanding of gas-phase protein structure, as well several mechanisms by which it can be manipulated. In Chapter II I use charge- and size-scaling behavior to understand the structures of extended protein ions and reveal mechanistic details of supercharging electrospray ionization. Material in this chapter was published in *Analytical Chemistry* and co-authored by James S. Prell, Simon A. Ewing, Muhammad A. Zenaidee, and William A. Donald. In Chapter III I turn my attention to compact, native-like protein ions and uncover details of the relationship between and energetics of collisional and surface activation, two commonly-used methods for perturbing gas-phase protein structure. Material in this chapter was published in *Chemical Science* and co-authored by James S. Prell and Austin M. Mroz. I extend this line of inquiry in Chapter IV by introducing a quantitative method for rapidly determining activation energies for gas-phase protein unfolding and dissociation and utilizing the method to identify common features of gas-phase protein unfolding transitions. Material in this chapter was published in the *Journal of the American Society for Mass Spectrometry* and co-authored by James S. Prell and Samantha O. Shepherd. Lastly, in Chapter V I apply the method introduced in Chapter IV to demonstrate non-specific lipid head group binding to soluble proteins that can be predicted by gas-phase basicities and discuss the implications for studying membrane protein-lipid interactions with native mass spectrometry. A manuscript based on this work is in preparation and will include material co-authored by James S. Prell, Jesse W. Wilson, and Samantha O. Shepherd.

CHAPTER II

EXTENDED PROTEIN IONS ARE FORMED BY THE CHAIN EJECTION MODEL IN CHEMICAL SUPERCHARGING ELECTROSPRAY IONIZATION

Reprinted with permission from Donor, M. T.; Ewing, S. A.; Zenaidee, M. A.; Donald, W. A.; Prell, J. S. Extended Protein Ions are Formed by the Chain Ejection Model in Chemical Supercharging Electrospray Ionization. *Anal. Chem.* **2017**, *89*, 5107-5114.

Copyright 2017 American Chemical Society.

Introduction

Electrospray ionization (ESI) can be used to ionize folded proteins from buffered aqueous solutions at or near physiological pH values while retaining non-covalent interactions and high-order structure.[144,145] Mass spectrometry (MS) can often be used to determine properties such as complex stoichiometry,[146-148] the number and chemical identity of bound ligands,[149-152] and, when coupled with ion mobility spectrometry (IM-MS), the overall size and/or shape of the protein ions or complexes determined from collisional cross section (CCS) measurements.[67,153,154] In contrast to other common ionization methods, such as MALDI, ESI of proteins produces a set of multiply-charged ions with a distribution of intensities (charge state envelope). Furthermore, folded protein ions formed by conventional ESI typically populate relatively low charge states while denatured proteins exhibit higher charge states. The ability to manipulate protein charge states can also be useful. For example, higher charge states can improve mass accuracy in high-resolution MS and lead to greater fragmentation efficiency in electron capture or transfer dissociation or collision-induced dissociation (CID),[29-31] and compact protein ions with lower charge states can be more resistant to gas-phase unfolding due to activation, including in surface-induced dissociation (SID) experiments used to infer oligomer structure.[38,40,41,155] Solution additives to either raise or lower charge states have been found: “supercharging” reagents often increase observed charge states[43-46] while charge reduction reagents tend to decrease charge states and are routinely used to limit unfolding of protein complexes prior to dissociation, as in SID experiments.[38,40,156-158] Supercharging can alternatively be accomplished by raising the nanoESI spray potential (electrothermal supercharging).[159]

Multiple mechanisms have been proposed to explain charging in ESI under native and denaturing conditions. In the ion evaporation model (IEM),[15] charged species are emitted from nanometer-sized droplets. By contrast, in the charged residue model (CRM),[19] the solvent droplet fully evaporates and the residual charges are transferred to the analyte(s) inside the droplet, with the number of charges roughly corresponding to the Rayleigh-limit charge (the charge at which the Coulomb repulsion balances with the solvent surface tension) of an equivalently-sized solvent droplet. In the chain ejection model (CEM),[25,26] a disordered (bio)polymer chain is partially ejected from the droplet, leading to proton migration to the exposed portion of the ion, followed by further extrusion and ultimate ejection of the extended chain. The CEM was proposed to explain the high charge states observed in mass spectra of proteins electrosprayed from denaturing solutions. Much current evidence suggests that folded proteins formed by ESI from buffered aqueous solution ionize by the CRM, small ions by the IEM, and unfolded, disordered proteins by the CEM.[14,21,160] The CRM predicts that charge state is roughly proportional to ion surface area for quasi-spherical ions and thus the charge state should scale as approximately the square root of mass. Similarly, the CCS of a quasi-spherical ion of fixed density should scale approximately as the two-thirds power of its mass. Experimental CCS data for a variety of native-like protein ions follows the two-thirds power law,[76,77,161] while the experimental scaling power for average charge state is slightly greater than one half (0.54-0.57).[21,23,33,78,162-164] These results provide additional support for the CRM and demonstrate the efficacy of inferring structural and mechanistic details based on scaling laws. For highly-charged, unfolded protein ions that likely adopt coil-like and/or extended conformations in the gas-phase, scaling laws for CCS and charge are difficult to predict *a priori*, although empirical scaling laws for similarly-sized intrinsically disordered protein ions have been found experimentally.[33,78] Simultaneous determination of experimental charge state and CCS scaling laws with comparison to theoretical models will improve understanding of the structures of unfolded protein ions and may enable more precise determination of ion structure than either charge state or CCS alone.

Manipulating charge states via conventional, i.e., chemical, supercharging is typically accomplished by adding small amounts (1-5%) of polar, high-boiling point compounds such as *m*-nitrobenzyl alcohol (*m*-NBA) or sulfolane to ESI samples. (Hereafter I use the term “supercharging” to refer to chemical, as opposed to electrothermal, supercharging.) Recently, 1,2-butylene carbonate (BC) and other alkyl carbonates have been shown in some cases to be more effective supercharging reagents than *m*-NBA or sulfolane.[48,50,165] The magnitude of the observed charge state increase can vary from a few percent[45,56] to a two-fold increase,[50,165] depending on solution conditions and the chemical identity of the supercharging reagent. In addition to increasing charge states, supercharging has been used to reduce salt adduction to proteins,[49] and as a way to bypass a solution-phase acidic quench step in top-down hydrogen/deuterium exchange experiments.[52]

Many details of the mechanism of supercharging remain poorly understood, although multiple mechanisms for supercharging have been proposed.[44,53-57] The quantities of supercharging reagents used will have only minor effects on protein structure in bulk solution. It has been hypothesized that chemical and/or thermal denaturation in the droplet during the late stages of ESI is responsible for supercharging.[44,55-57] Recently, Konermann has proposed a mechanism whereby enrichment of the droplets in the supercharging reagent leads to charges becoming trapped on the surface of the folded protein, which after solvent evaporation unfolds due to Coulomb repulsion of the charge sites.[54] This mechanism is supported by molecular dynamics simulations using force fields optimized for bulk solution and in which sodium ions are the charge source. Understanding the mechanism of supercharging, including estimating the timescale of protein unfolding and the chemical environment in which it occurs, is of both fundamental and practical importance.

In order to elucidate the mechanism of supercharging, I show that the effects of supercharging do not depend strongly on protein size or amino acid composition for a variety of monomeric protein ions with masses up to 94 kDa, that largely folded structures are retained in bulk supercharging solution, and that similar starting structures can lead to dramatically different ion charge states and CCSs for protein ions with native and reduced internal disulfide bonds. I derive a simple analytical model that predicts the extent of charging for highly-extended protein ions and accurately reproduces the experimental observations. CD data confirm that supercharging reagents minimally perturb protein structure in bulk solution, while internal disulfide reduction leads to an increase in the extent of protein charging, suggesting that supercharging causes these proteins to unfold within the ESI droplet prior to ejection and proceeds via a CEM-like ionization mechanism rather than a CRM-like mechanism.

Methods

Sample preparation. Head-to-tail-linear $\mathrm{Ubq}_{2\text{-}11}$ were purchased from Enzo Life Sciences, the 31-kDa N-terminal domain of anthrax lethal factor protein ($\mathrm{LF_N}$) and anthrax protective antigen (PA_{63}) were graciously provided by Dr. Bryan Krantz (University of Maryland), and bovine serum albumin (BSA), lysozyme, cytochrome C, ubiquitin, myoglobin (Mg), avidin, concanavalin A, carbonic anhydrase (CA), alcohol dehydrogenase (ADH), and β-lactoglobulin were purchased from Sigma-Aldrich. Lyophilized proteins were reconstituted in ultrapure (18 MΩ) water. In experiments with reduced BSA, β-lactoglobulin, and lysozyme, the protein was incubated with 50 mM dithiothreitol for 2 hr at 37 °C (BSA), 18 hr at 37 °C (β-lactoglobulin), or 18 hr at ambient temperature (lysozyme) to reduce the internal disulfide bonds. CD or mass spectral analysis of reduced bovine serum albumin, β-lactoglobulin, or lysozyme was performed immediately following reduction to limit re-formation of disulfide bonds. For native IM-MS experiments, protein samples were buffer-exchanged using Micro Bio-Spin 6 columns (Bio-Rad) into either 200 mM ammonium acetate/10 mM ammonium bicarbonate at pH 7.0 ($\mathrm{LF_N}$ and PA_{63}) or 200 mM ammonium acetate at pH 7.2 (all other proteins) with a protein concentration of 1-10 µM. For denaturing experiments, protein samples were buffer-exchanged using Micro Bio-Spin 6 columns into 49/49/2 v/v/v water/methanol/acetic acid at a protein concentration of 1-10 µM. For supercharging experiments, protein samples were buffer-exchanged using Micro Bio-Spin 6 columns into 94.5/5/0.5 v/v/v water/1,2-butylene carbonate (BC)/acetic acid at a protein concentration of 1-10 µM. Samples for circular dichroism spectroscopy were prepared using either pure water, 49/49/2 v/v/v water/methanol/acetic acid (denaturing conditions), or 94.5/5/0.5 v/v/v water/BC/acetic acid (supercharging conditions) at a protein concentration of approximately 5 µM.

Mass spectrometry. Ion mobility-mass spectra were acquired at the University of Oregon using a Synapt G2-S*i* ion mobility-mass spectrometer (Waters Corp.) equipped with a nanoelectrospray (nanoESI) source. NanoESI emitters with a tip i.d. of less than 1 µm were pulled from borosilicate capillaries with an i.d. of 0.78 mm using a Flaming-Brown P-97 micropipette puller (Sutter Instruments). For mass spectrometry analysis, 3-5 µL of sample was loaded into an emitter, and electrospray was initiated by applying a potential (relative to instrument ground) of +0.8-1.2 kV to a platinum wire in electrical contact with the solution. For native IM-MS experiments the ion source temperature was equilibrated to ambient temperature, and for denatured and supercharging experiments the source temperature was 150 °C. Mass spectra for the BSA and β-lactoglobulin reduction experiments were collected in “Resolution” mode, and all other mass spectra were collected in “Sensitivity” mode. The Trap and Transfer collision voltages were 5-15 V and 5 V, respectively, and argon trap gas was used at a flow rate of 5-10 mL/min. The maximum charge state for which the signal-to-noise ratio was greater than 2:1 was determined to be the highest-observed charge state.

Travelling-wave ion mobility data were calibrated using an established procedure.[77,161] Cytochrome C, β-lactoglobulin, avidin, BSA, and concanavalin A were used as calibrants for native IM-MS analyses, and denatured (48/48/2 v/v/v water/methanol/formic acid) ubiquitin, cytochrome C, and myoglobin were used as calibrants for supercharged and denatured IM-MS analyses. Nitrogen was used as the buffer gas for ion mobility spectrometry at a flow rate of 50 mL/min. The traveling wave velocity was set to 450-600 m/s and the wave height to 10-20 V.

Gas-phase basicity measurements. Ion-molecule reaction experiments were conducted at UNSW, Sydney, on a linear quadrupole ion trap mass spectrometer (LTQ-MS; ThermoFisher Scientific), modified with an ion funnel (Heartland Mobility) that is equipped with an external nanoelectrospray ionization (ESI) source. NanoESI emitter tips were prepared by pulling borosilicate capillaries (1.2 mm OD, 0.69 mm ID, Harvard Apparatus Limited) to an inner diameter of ~2 μm using a micropipette puller (Narishige PN-3, Narishige Scientific Instrument Labs) and sputter coated with a thin layer of Au and Pd for 20 s using a Scancoat Six (Edwards; Au/Pd alloy target). ESI emitters were positioned ~1-2 mm on axis from the heated capillary entrance to the MS. To establish ESI, a voltage of 1.0 to 1.9 kV was applied between the nanoESI emitter and heated capillary entrance. ESI solutions contained 10 μM of protein (either Ubq_1 or Ubq_3), 1/5/42/42 v/v/v/v acetic acid/BC/water/methanol. Protein charge states were isolated using an isolation window of ~ ± 5 *m*/*z* that was centered on the ion of interest. Ion-molecule reaction times between size-selected protonated protein ions and neutral molecules (propane, water, methanol, hexamine, 3-fluropyridine, pyridine, tri-n-propylamine) were varied between 0 and 30 s. Neutral molecules were introduced into the ion trap of the mass spectrometer through the standard He line that is modified with a custom gas mixer which introduces the neutral molecule into the gas line as a vapor.[166,167] The effective temperature of ions trapped by this type of mass spectrometer have been measured to be near ambient temperature.[168]

The bracketing method was used to determine the apparent gas-phase basicity (GB^{app}, which is the sum of $-\Delta G$ for the addition of a single proton to the ion at 298 K and the repulsive Coulomb barrier) of protein ions by observing proton transfer reactions between protein ions that have an unknown GB^{app} value with bases that have known gas-phase basicity values.[169,170] If proton transfer reactions are observed between the [protein, $(z+1)H]^{(z+1)+}$ and the base, this indicates that the GB^{app} of [protein, $zH]^{z+}$ is lower than the base. If the proton transfer reaction is not observed, the GB^{app} value of the corresponding protein ion is higher than the GB value of the neutral molecule. By use of a series of bases corresponding to a “ladder” of different GB values, GB^{app} values for an unknown ion can be assigned to within 10 kJ/mol.

The rates of proton transfer reactions between protonated protein ions and neutral molecules were calculated by fitting pseudo-first order rates of reaction to the precursor ion decay given by:

$$-kt = \ln\left(\frac{I_0}{\sum I_i}\right) \tag{1}$$

where k is the rate constant of the reaction, t is time in seconds, I_0 is the peak area of the isolated charge state, $\sum I_i$ is the sum of the peak areas of all the product ions. Proton-transfer rate constants were obtained from the linear regression best fits to plots of ln$(I_0/\sum I_i)$ vs. reaction time for a minimum of eight different reaction times. For all kinetic plots used to obtain the rate constants given in Table A3, the R^2 values and y-axis intercepts were greater than 0.97 and near zero, respectively. Reaction rates less than $1.0\text{x}10^{11}$ cm^3 /mol•s were considered to be unreactive for the purposes of obtaining GB^{app} values.[169,170]

Circular dichroism spectroscopy. Circular dichroism (CD) spectra were acquired using a Jasco J-815 CD spectrometer. The spectral window for the experiments with Ubq_1 and Ubq_4 was 175-300 nm, and it was 200-260 nm for the experiments with BSA and β-lactoglobulin. CD spectra for all samples were corrected with a solvent blank.

Charge state and collisional cross section modeling. Linear straight-chain (φ = 180°, ψ = 180°) and α-helical (φ = –60°, ψ = –40°) model structures of $Ubq_{1\text{-}11}$ were constructed in Avogadro.[171] Optimal charge site configurations for the highest-observed charge states of supercharged $Ubq_{1\text{-}11}$ were computed assuming either linear straight-chain or α-helical structure using Collidoscope[64] with proton affinities ($-\Delta H$ for the addition of a single proton to the residue at 298 K) or gas basicities of basic residues from literature values[172,173] and relative dielectric permittivity of 2.0. Corresponding collisional cross sections for linear straight-chain and α-helical $(Ubq_1)^{14+}$, $(Ubq_2)^{26+}$, and $(Ubq_3)^{37+}$ were computed by the Trajectory Method with N_2 as the buffer gas using Collidoscope.[64]

Results and Discussion

Protein structure in native, denaturing, and supercharging solution. Circular dichroism spectra of ubiquitin (Ubq_1) and tetra-ubiquitin (Ubq_4) in water, supercharging solution (94.5/5/0.5 water/BC/acetic acid), and denaturing solution (49/49/2 water/methanol/acetic acid) are shown in Figure 5. The CD spectrum of Ubq_1 in water is very similar to previously reported data for folded $\mathrm{Ubq_1}$,[174] with a peak at 207 nm and a shoulder around 220 nm. $\mathrm{Ubq_4}$ under the same solution conditions has a similar CD spectrum to $\mathrm{Ubq_1}$, with an ellipticity approximately 2.6 times that of $\mathrm{Ubq_1}$, indicating that the secondary and tertiary structures of each Ubq monomer in $\mathrm{Ubq_4}$ are similar to that of $\mathrm{Ubq_1}$. The CD spectra of both proteins in supercharging solution are very similar to those in water, although for both proteins there is a 5-10% decrease in signal at 207 nm and a 15-20% increase at 220 nm indicating a small decrease in ordered secondary structure content. In contrast, the CD spectra in denaturing solution exhibit a marked increase in signal intensity at 207 and 220 nm compared to the spectra in water, consistent with a transition to the highly α-helical A state of $\mathrm{Ubq_1}$ as previously reported for $\mathrm{Ubq_1}$ in alcohol solutions.[174] The CD data indicate that $\mathrm{Ubq_1}$ and $\mathrm{Ubq_4}$ in supercharging solution have very similar secondary structure content to native, folded $\mathrm{Ubq_1}$ and $\mathrm{Ubq_4}$, and dramatically different secondary structure is observed for these proteins in denaturing solution.

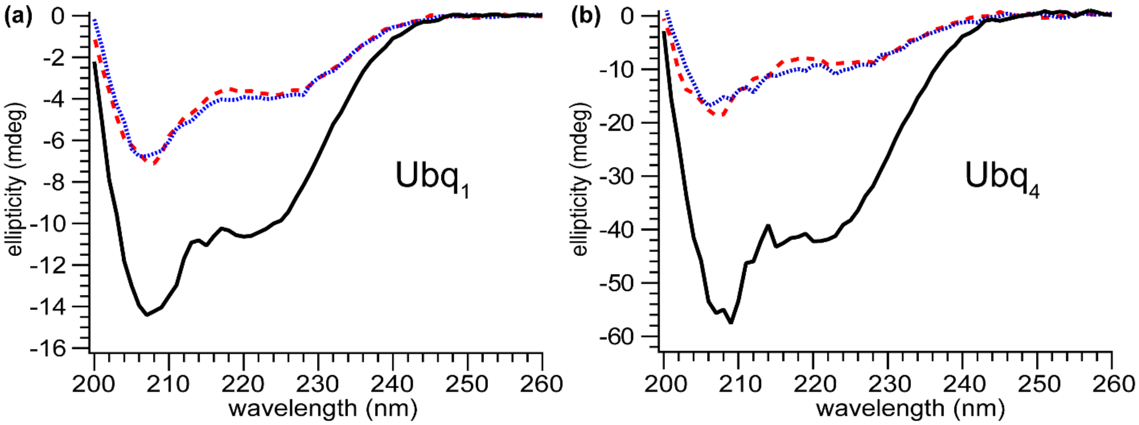

Figure 5. Circular dichroism spectra of **(a)** $\mathrm{Ubq_1}$ and **(b)** $\mathrm{Ubq_4}$ in water (dashed red line), supercharging conditions (dotted blue line), and denaturing conditions (solid black line).

Mass-dependent scaling behavior of charge state distributions. In principle, proteins of different sizes can have different amino acid composition, potentially confounding accurate determination of charge-state or other scaling as a function of mass. To eliminate this potential confounding factor, mass spectra were acquired for head-to-tail-linked poly-ubiquitins ($Ubq_{1\text{-}11}$) under native and supercharging conditions. The average (z_{avg}) and most abundant charge states for $Ubq_{1\text{-}11}$ in native conditions and highest observed and most abundant charge states in supercharging conditions are shown in Table A1. For native $Ubq_{1\text{-}11}$ considered here, z_{avg} is found to scale as $(\text{mass})^{0.55 \pm 0.01}$, in good agreement with previously reported values (0.54-0.57)[21,23,33,78,162-164] and slightly above that predicted for perfectly spherical, uniformly dense proteins based on the CRM (0.5) (Figure 6a). The highest observed charge states for the supercharged $Ubq_{1\text{-}11}$ scale according to a $(z–1)\times\ln(z–1)$ relationship (Figure 6b), and clearly do not follow a simple linear scaling law (Figure 6c). This scaling law ($\text{mass} \propto (z–1)\times\ln(z–1)$) was derived analytically (see Appendix A) by treating the protein as a line segment with uniformly spaced point charges and assuming that the difference in the apparent gas-phase basicity[175] between the z_{max} and $z_{max}+1$ charge states is independent of protein size and is equal to the gas-phase basicity of water. This is supported by experimental gas-phase basicity measurements of supercharged Ubq_1 and Ubq_3, which are found to be 695.4 and 636.8 kJ/mol, respectively (Table A3). These results indicate that $Ubq_{1\text{-}11}$ ionized under native-like conditions have charge states consistent with the CRM for folded structures, and that supercharged $Ubq_{1\text{-}11}$ adopt quasi-linear conformations during the electrospray process, consistent with the CEM and previous studies of Ubq_1.[165] Charge states for native-like or supercharged ions of all other proteins studied (myoglobin, carbonic anhydrase, alcohol dehydrogenase monomer, LF_N, and PA_{63}) agree well with these

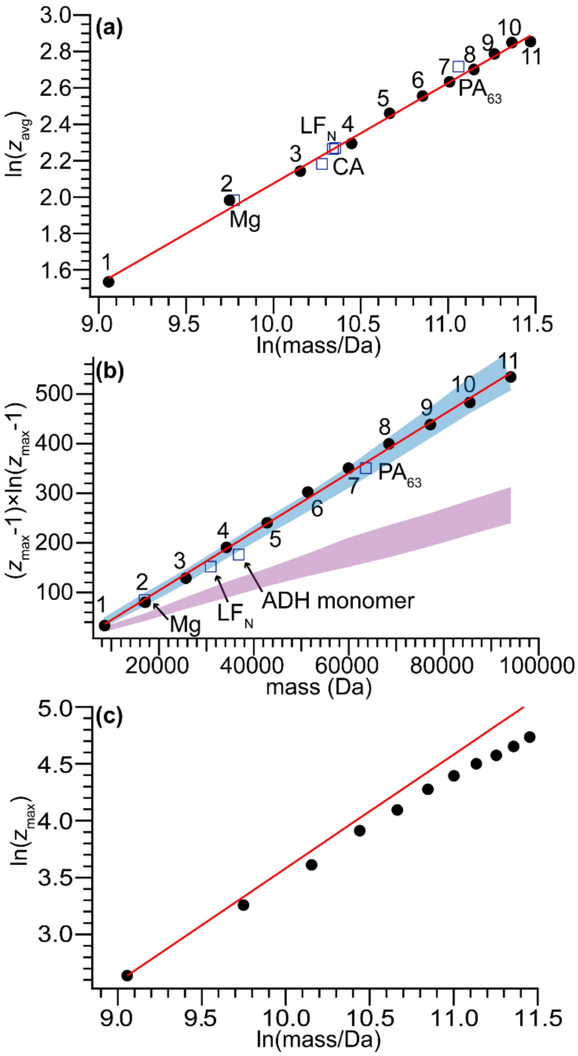

Figure 6. (a) Plot of ln(z_{avg}) vs. ln(mass) for native Ubq$_{1-11}$ with linear trend line. **(b)** Plot of analytically-derived scaling relation for highest observed charge states of supercharged Ubq$_{1-11}$ vs. mass, with linear trend line. The blue band is a range of calculated charge states for straight-chain Ubq$_{1-11}$ using either gas-phase basicity (upper limit) or proton affinity (lower limit). The purple band is the same range for α-helical Ubq$_{1-11}$. **(c)** Plot of ln(z_{max}) vs. ln(mass) for supercharged Ubq$_{1-11}$ with trend line showing hypothetical linear scaling that deviates significantly from observed data.

scaling laws despite their different amino acid compositions (Table A2), suggesting that amino acid composition is not the most important factor in the observed charge states for these ions.

Mass-dependent scaling of collisional cross sections. IM-MS data were acquired for Ubq$_{1-11}$ under native, denatured, and supercharging conditions. For native Ubq$_{1-11}$, the CCS of the most abundant charge state scales as (mass)$^{0.62 \pm 0.01}$ and that for the immediately lower charge state scales as (mass)$^{0.63 \pm 0.01}$, in good agreement with the expected two-thirds power scaling for folded, globular structures (Figure 7a). IM-MS data for myoglobin (17 kDa), LF$_N$ (31 kDa), carbonic anhydrase (29 kDa), and PA$_{63}$ (63 kDa) in native conditions follow a similar trend, with CCS values close to Ubq$_{1-11}$ of similar mass. By contrast, for supercharged Ubq$_{1-11}$, the mass scaling powers for the CCSs of the highest and most abundant charge states are 0.98 ± 0.01 and 1.02 ± 0.02, respectively (Figure 7c). Data for myoglobin, LF$_N$, alcohol dehydrogenase, and PA$_{63}$ follow the same trend, with CCS values close to those of Ubq$_{1-11}$ of similar mass. Thus CCS scales linearly with mass for these supercharged, highly-unfolded protein ions independent of the identity of the protein. For denatured Ubq$_{1-11}$ ions, the CCS also scales linearly with mass (Figure 7b), with an experimental scaling power of 1.01 ± 0.01. Supercharging of these proteins creates ions with densities similar to those formed by nanoESI of solution-denatured proteins. The linear scaling of CCS with mass for both types of ions indicates that they have quasi-one-dimensional structures.

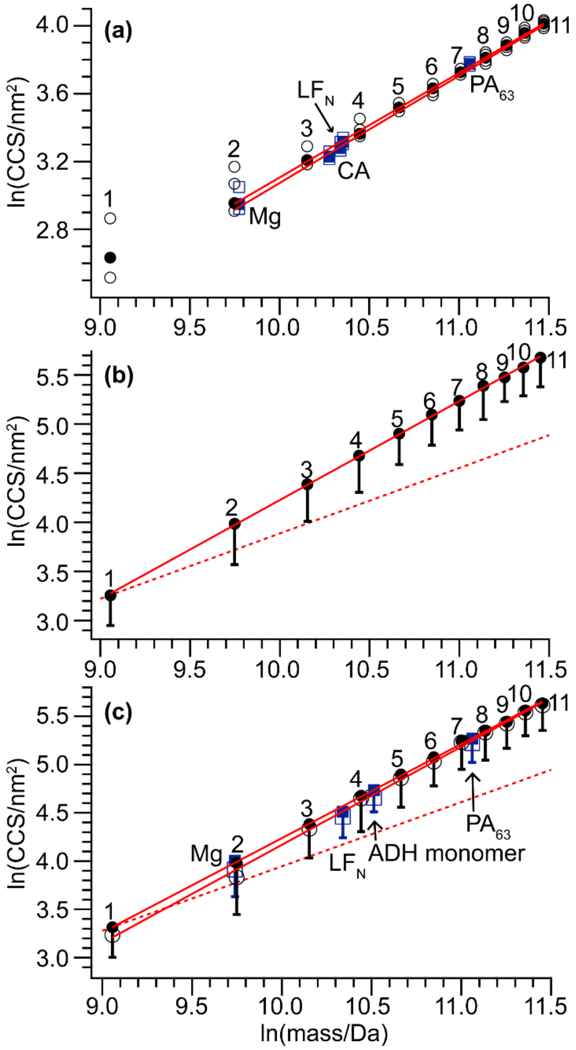

Figure 7. Plots of ln(CCS) vs. ln(mass) for **(a)** native, **(b)** denatured, and **(c)** supercharged Ubq$_{1-11}$ and other proteins (see text) with linear trend lines (solid). In **(a)** the most abundant charge state of Ubq$_{1-11}$ (resp., other proteins) is plotted as filled circles (resp., squares) and other charge states as open circles (resp., squares). Note that Ubq$_1$ falls below the size range used for IM calibration and thus was omitted from the fit. In **(b)** and **(c)** the highest observed charge state for Ubq$_{1-11}$ (resp., other proteins) is plotted as filled circles (resp., squares), the most abundant charge state as open circles (resp., squares), and the other charge states are represented by lines spanning the highest and lowest charge states. Hypothetical 2/3 scaling power trend lines are shown as dashed lines.

“Quasi-linear” structures. CCSs were computed for straight chain and α-helical Ubq$_{1-3}$ (Figure A1). Both structures exhibit linear

CCS scaling, but CCS increases much more quickly with mass for straight chain $\mathrm{Ubq}_{1\text{-}3}$ (i.e. the slope of CCS vs. mass is greater) (Figure A1). Experimental CCSs for $\mathrm{Ubq}_{1\text{-}3}$ are significantly greater than those calculated for α-helical structures and close to the straight chain values. This agrees with prior investigations of the structures of high charge states of ubiquitin and α-synuclein, which found that these ions are in highly unfolded conformations but are not completely linear chains – their CCS values approach but do not reach those calculated for a theoretical linear chain conformation.[35,88,165] Charge site calculations for $\mathrm{Ubq}_{1\text{-}11}$ demonstrate that the experimentally-observed charge states fall much closer to those calculated for the straight-chain structures than for the α-helical structures (Figure 6b). These data support experimental structures that are significantly more unfolded than α-helical structures but are not completely straight chains. Interestingly, Ubq_{11} modeled as a straight chain (respectively, α-helix) is predicted to have a length of 300 nm (resp., 126 nm), based on simple model structures using constant dihedral angles. These values are considerably larger than the initial diameter of ESI droplets in our experiments, which I estimate to be at most 100 nm, based on the inner diameter of the ESI emitters used. Although the actual structures adopted in these experiments are not perfectly straight, even significantly more folded/compact structures than these should have diameters close to or larger than the initial ESI droplet, consistent with very dramatic unfolding of the initial folded structures during the supercharging ESI process.

Effects of internal disulfide bonds. To elucidate when unfolding occurs during supercharging, i.e., “early” via a CEM-like mechanism[44,55-57] or “late” via a CRM-like mechanism,[54] a comparison of the extent of supercharging was performed for native and reduced BSA, β-lactoglobulin, and lysozyme, which contain 17, 2, and 4 disulfide bonds in their native forms. If protein unfolding occurs in the gas phase after charging by the CRM-like mechanism described by Konermann,[54] then the presence of internal disulfide bonds, which do not significantly affect folding in solution (see below), should have little effect on the observed charge states. However, if unfolding occurs in the droplet prior to or simultaneously with charging, as in the CEM, internal disulfides would be expected to decrease the amount of charging because they limit how extended the structure of the protein can become.

Reduced BSA, β-lactoglobulin, and lysozyme were buffer exchanged into ammonium acetate and the reduced and un-reduced proteins were compared. CD spectroscopy of BSA and β-lactoglobulin shows that minor changes in secondary structure content occur following reduction. Un-reduced BSA exhibits two peaks, one at 222 nm and another at 210 nm, characteristic of a structure rich in α-helical content and consistent with its crystal structure (Figure A2d). A similar CD spectrum is observed for reduced BSA, albeit with a decrease in signal, indicating a small decrease in the amount of α-helix present and an increase in the amount of conformational flexibility, as expected for a compact structure with reduced disulfide bonds. The CD spectrum of un-reduced β-lactoglobulin has a prominent peak at 218 nm and a shoulder at 208 nm, corresponding to a primarily β-sheet structure with a small amount of α-helical content (Figure A3d). The CD spectrum of reduced β-lactoglobulin exhibits a 3% decrease in signal at 218 nm and a 9% increase at 208 nm, indicative of an increase in α-helical content and a slight shift towards a more disordered state, consistent with a largely folded protein with broken disulfide bonds.[176] However, the small magnitude of the changes indicates that reduced β-lactoglobulin remains in a similar conformation to the un-reduced form.

For all three proteins, comparison of IM-MS data for the reduced and un-reduced protein shows that following exchange into native ESI buffer the reduced protein retains a compact conformation, as evidenced by the low and narrow charge state distributions. For BSA and lysozyme the charge state distributions are virtually identical for the reduced and unreduced forms (Figure A2, A4), while for β-lactoglobulin a smaller population of dimers and a small amount of higher charge states are observed in the mass spectrum of the reduced protein (Figure A3). Comparison of arrival time distributions shows that the un-reduced and reduced proteins have similar CCSs, with a 0-2% increase in drift time for the reduced species (Table A4), within the ~3% uncertainty of the measurement.[77] This slight expansion is attributed to increased conformational flexibility upon reduction of the disulfide bonds. The CD and IM-MS results indicate that reduced BSA, β-lactoglobulin, and lysozyme can still adopt a compact, native-like conformations, albeit with minor changes in secondary structure. Additionally, CD of BSA in supercharging conditions shows that the un-reduced and reduced samples have similar secondary structure content (Figure 8). However, compared to the CD spectra in native conditions, the peak at 210 nm is much more prominent. This is likely due to a conformational transition to the F state of BSA, in which domain II converts to a molten-globule state and the overall structure remains compact.[177-179]

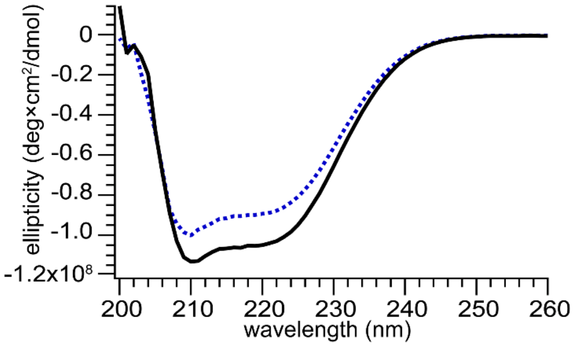

Figure 8. Circular dichroism spectra of un-reduced (solid black line) and reduced (dashed blue line) BSA in supercharging solution.

Supercharging of reduced BSA, β-lactoglobulin, and lysozyme resulted in a marked increase in observed charge state as compared to the un-reduced proteins. For BSA the highest observed charge state increased from 78+ to 87+ and the most abundant charge state increased from 60+ to 70+ (Figure 9). For β-lactoglobulin the highest observed charge state increased from 21+ to 23+, and the most abundant charge state of the reduced protein is 19+, while for the un-reduced sample the charge state distribution is bimodal with local maxima at 15+ and 11+ (Figure A5). For lysozyme the highest observed charge state increased from 17+ to 19+ and the most abundant charge state increased from 11+ to 14+ (Figure A5). Reduction of the internal disulfides thus leads to an increase in the charge state when supercharging, while both reduced and un-reduced samples exhibit native-like, compact structures of very similar size when electrosprayed from buffered aqueous solution. Additionally, all of the reduced proteins access more unfolded conformations with larger CCS than the un-reduced proteins across a range of

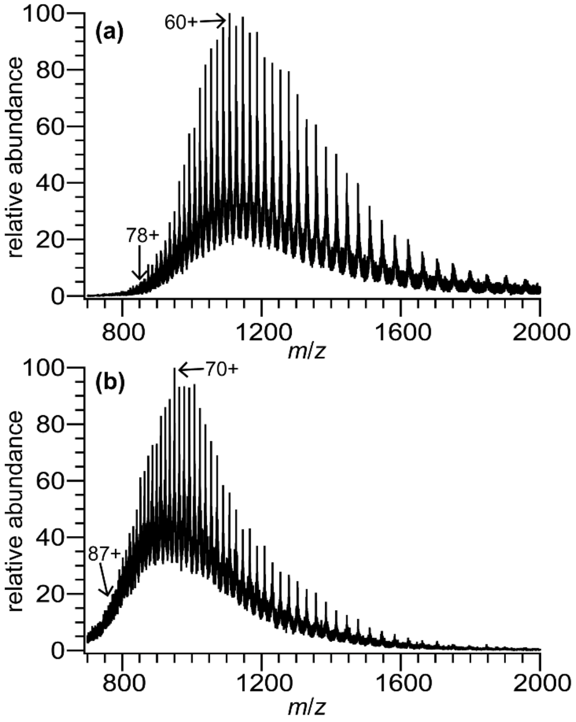

Figure 9. (a) Mass spectrum of supercharged, un-reduced BSA. **(b)** Mass spectrum of supercharged, reduced BSA.

charge states (Figure A6). These data suggest that the ion charge states observed upon supercharging depend on the flexibility of the protein chain in solution and number of intact disulfide linkages, and not simply on the initial folded structure in solution. This strongly supports a supercharging mechanism for these ions whereby unfolding and ejection of these protein chains occurs during the electrospray process and before all solvent and supercharging reagent have evaporated, i.e. a CEM-like model.

Conclusions

IM-MS was used to systematically investigate the charge and CCS scaling behavior of supercharged proteins across a wide range of sizes and to investigate the mechanism of chemical supercharging in ESI. CD spectroscopy results confirm that Ubq_1 and Ubq_4 in supercharging solution have secondary structure content very similar to that of natively folded proteins and dissimilar to that of denatured Ubq_1 and Ubq_4. In contrast, IM-MS data for solution-denatured and supercharged proteins show that both charge state and CCS scale in a manner consistent with quasi-one-dimensional gas phase structures. I derive an analytical model that accurately predicts the experimental charge state behavior, and GB^{app} results verify the assumptions in the model. GB^{app} measurements also indicate that supercharged Ubq_1 and Ubq_3 are approximately as basic as water, so there is likely a quasi-equilibrium with water vapor that controls the extent of charging for highly-unfolded protein ions. However, the GB^{app} of native-like Ubq_1 and Ubq_3 ions were found to be approximately the same as pyridine. These results agree with a recent report by Susa et. al.[180] and suggest that charging of proteins via the CRM is limited by droplet size near the end of the evaporation process, whereas supercharging of proteins via the CEM occurs in the water-rich atmosphere of the electrospray plume and/or evaporating droplet at an earlier stage of evaporation. Reduction experiments show that the proteins with reduced disulfide bonds have structures similar to those with native disulfide bonds as demonstrated by native IM-MS and CD. However, the extent of charging increases for the reduced proteins in supercharging conditions, demonstrating that the amount of charging depends on the presence of internal disulfide bonds and not only on the overall folded structure. Those results are consistent with supercharging causing unfolding prior to evaporation of all solvent and suggests that supercharging proceeds by a CEM-like ionization mechanism rather than a CRM-like mechanism. I expect that systematic, simultaneous investigation of expected charge states and CCSs for model structures, such as that described here, can lead to more accurate structure assignment with IM-MS and refinement of computational methods used to probe ionization dynamics.

In this chapter I studied the ESI process and some of the ways in which the final gas-phase structures of proteins can be manipulated during ESI. However, as shown here, supercharging ESI tends to produce highly unfolded protein ions. It can also be advantageous to exert finer control over the degree of unfolding, which can be accomplished by performing the structural perturbation in the gas phase. In Chapter III I turn my focus to gas-phase structural changes of proteins and the methods used to produce them, and I begin to develop a quantitative understanding of collisional and surface activation of protein ions.

CHAPTER III

EXPERIMENTAL AND THEORETICAL INVESTIGATION OF OVERALL ENERGY DEPOSITION IN SURFACE-INDUCED UNFOLDING OF PROTEIN IONS

Reprinted with permission from Donor, M. T.; Mroz, A. M.; Prell, J. S. Experimental and Theoretical Investigation of Overall Energy Deposition in Surface-Induced Unfolding of Protein Ions. *Chem. Sci.* **2019**, *10*, 4097-4106 – Published by The Royal Society of Chemistry.

Introduction

The ability of electrospray ionization (ESI) to preserve native-like non-covalent interactions into the gas phase has led to the study of a range of important biological systems using native mass spectrometry. Native ion mobility-mass spectrometry (IM-MS), which can be used to characterize the overall shape and size of an ion by determining its collisional cross section (CCS) in a buffer gas, is a powerful tool for the investigation of high-order structure.[181] Various gas-phase dissociation methods can be used to disrupt covalent and/or non-covalent interactions in order to probe structural characteristics such as sequence,[182-184] location of ligand binding or post-translational modifications,[100,183,184] connectivity of subunits in a complex,[109-111] and differences in stability between closely-related structures.[85,86] These dissociation methods vary as to how the ion is activated, i.e., *via* charge transfer/recombination,[92,93,185,186] collisions with neutral species,[91] or absorption of photons.[94,95,187]

Collision induced dissociation (CID), in which ions are slowly heated by many low energy collisions with a neutral gas (e.g. Ar), is the most commonly-used method for interrogating protein complex composition using mass spectrometry. The products of CID for a non-covalently bound assembly such as a protein oligomer with n subunits are typically an ejected monomer and remaining (n-1)-mer.[86,188] For protein assembly ions, the charge of the complex is typically partitioned asymmetrically between the products – the monomer is often unfolded and carries a share of the charge that is larger than its share of the mass of the complex.[86,102,189] This provides useful information about the identity of the subunits in a complex but imparts only limited information about the quaternary structure of the complex.

By contrast, surface induced dissociation (SID) is an alternative dissociation method that can yield more information about the high-order structure of protein complexes than is typically obtained in CID.[40,190] In SID, dissociation is caused by a single high-energy collision event with a rigid surface, usually a gold electrode coated with a self-assembled monolayer of perfluorinated alkanethiol (FSAM). Unlike CID, SID often fragments native-like protein complexes such that the products remain compact on the millisecond timescale of the experiment and the charge is partitioned symmetrically.[42,105,190] Seminal results from the Wysocki group for a variety of protein homo- and heterooligomers indicate that the SID products in many cases reflect the quaternary structure of the complex observed in condensed-phase data (e.g. a hexamer with an x-ray crystal structure indicative of a dimer of trimers will dissociate into two trimers upon SID), and thus that SID can probe the high-order structure of protein complexes.[106,108-111] For protein complexes correlation between the surface area of the interfaces broken and the SID collision energy required to break them has been reported,[106] but the challenge of translating the nominal laboratory frame energies to internal energies has limited quantitative determination of protein-protein interfacial areas directly from SID data. SID has been implemented on a number of different mass spectrometry platforms, including FT-ICR[191,192] and Q-TOF[193] instruments. In partnership with Waters Corp., the Wysocki group has developed a kit that enables routine application of SID on Waters Synapt Q-IM-TOF instruments, making this platform a testbed for SID of native protein complexes.

The energetics of SID have been previously characterized, both experimentally[130,194,195] and computationally,[196,197] for small monomeric molecules and peptides. In general, the kinetics of product formation from these precursor ions after relatively low-energy surface collision can be well-described using unimolecular RRKM theory, indicating that the dissociation process occurs away from the surface following picosecond-timescale[196,198] thermalization of the energy deposited by the collision. Multiple studies have shown that approximately 20% of the ion's laboratory frame kinetic energy is converted to internal energy of the ion for collisions with the typical FSAM surfaces.[194-197] This fraction varies little with the angle of incidence, which instead modulates the proportion of the laboratory frame kinetic energy transferred out of the ion's translational modes or into the surface, with shallower angles decreasing transfer into the surface and increasing the amount of translational energy remaining after surface collision.[194] For some peptide ions, fragments that appear at very short reaction times suggest that "shattering" is an alternate dissociation pathway at high incident kinetic energies (such that greater than 10 eV is transferred to internal modes),[130,199] a result supported by simulations of glycine[200] and octaglycine[201] SID showing that specific collision orientations lead to shattering. Shattering, in which fragmentation is nearly instantaneous following surface impact (ps timescale), is also commonly observed for small molecules and large non-covalent clusters of atoms and small molecules (e.g. Ar, ammonium) colliding with the surface at high (transonic) velocities.[202-205]

Due to the vast number of degrees of freedom present in proteins and protein complexes, energy deposition and dissociation in SID can be much more difficult to study quantitatively using the same methods employed for peptides. Proteins and protein complexes also differ from peptides in that the observed fragments result from the disruption of many non-covalent interactions that can be distributed across a large surface area, rather than a single covalent bond. This raises the possibility that, when a small portion of a large species traveling at high velocity collides with the surface, shear forces and other mechanical effects may play a large role, leading to dissociation of some of these non-covalent interactions before thermalization is complete. Multiple collisions of the ion with the surface may also occur, further complicating the study of SID dynamics both computationally and experimentally.[197]

A first step towards understanding SID of protein complexes more quantitatively is to understand how surface collisions deposit energy into proteins more generally. Here, unfolding of protein monomers, as measured by ion mobility after surface collision, is used to investigate energy deposition upon surface collision. I demonstrate that proteins subjected to collision- and surface-induced unfolding (CIU and SIU, respectively) undergo the same unfolding transitions and quantify the relationship between their nominal laboratory-frame energy scales. Monte Carlo simulations and theoretical modeling of CIU enable calibration of the internal energy deposited for CIU, which in turn is used to calibrate overall energy deposition in SIU. I show that the efficiency of SIU, defined as the proportion of laboratory-frame kinetic energy converted to internal energy of the ion, can be nearly three times the efficiency of CIU for large monomeric proteins. Finally, SIU is shown to depend strongly on the structure of the precursor ion, with more unfolded ions having a smaller effective protein-surface CCS and lower energy transfer efficiency.

Methods

Sample preparation. Myoglobin, β-lactoglobulin, concanavalin A, carbonic anhydrase, alcohol dehydrogenase, albumin, bovine serum albumin, and transferrin were acquired from Sigma-Aldrich. Two protein components of anthrax lethal toxin, protective antigen, PA_{63}, and the N-terminal domain of lethal factor, LF_N, were graciously provided by Dr. Bryan Krantz at the University of Maryland. Lyophilized proteins were reconstituted in ultrapure (18 MΩ) water. Protein samples were exchanged into either 200 mM ammonium acetate 10 mM ammonium bicarbonate pH 8 (PA_{63}) or 200 mM ammonium acetate pH 7 (all other proteins) using Micro Bio-Spin 6 desalting columns (BioRad).

Ion mobility-mass spectrometry. All ion mobility-mass spectra were collected using a Synapt G2-S*i* ion mobility-mass spectrometer (Waters Corp.) equipped with a nanoelectrospray (nanoESI) source. NanoESI emitters with a tip ID of approximately 1 µm were pulled from borosilicate capillaries with an ID of 0.78 mm using a Flaming-Brown P-97 micropipette puller (Sutter Instruments). For mass spectrometry analysis, 3-5 µL of sample was loaded into an emitter, and electrospray was initiated by applying a potential (relative to instrument ground) of +0.7-1.1 kV to a platinum wire in electrical contact with the solution. All experiments were conducted in “Sensitivity” mode with the source equilibrated to ambient temperature and a backing pressure of 3.7 mbar. Traveling wave velocities of 400-550 m/s and wave heights of 18-25 V were used in all experiments. Nitrogen was used as the buffer gas in ion mobility experiments, and the helium cell and nitrogen gas flows were set to 100 mL/min and 50 mL/min, respectively. Measured arrival time distributions were converted to collisional cross sections using an established literature procedure.[77,161] Cytochrome C, β-lactoglobulin, avidin, bovine serum albumin, and concanavalin A were used as ion mobility calibrants.

Collision-induced unfolding. Collisional activation in the Waters Synapt G2-S*i* occurs in the “Trap” region of the instrument, located between the quadrupole and the ion mobility cell. A single charge state was isolated using the quadrupole with the LM Resolution set to 4.0 and the HM Resolution to 15. Collision-induced unfolding was performed by increasing the acceleration voltage (Trap CE) in 5 V increments, starting at 5 V and ending when significant fragmentation of the precursor ion was observed. The Trap gas flow was set to 5 mL/min for all collision-induced unfolding experiments. Arrival time distributions for each acceleration voltage were extracted using MassLynx 4.1 (Waters) and “fingerprint” images were generated using Igor Pro (WaveMetrics). For each acceleration voltage, the Multi Peak Fitting package in Igor Pro was used to fit the arrival time distribution with a number of Gaussian functions corresponding to the number of conformer families present. The area of each peak was computed to determine the relative abundance of each conformer family. For transitions resulting in at least 50% conversion to the more unfolded conformer family in both SIU and CIU, appearance energies were determined by summing the relative abundances of each conformer family with a larger CCS than that of the initial family for the transition (i.e. for the transition out of conformer family 1, sum the abundances of families 2, 3, and 4), and fitting that data with a sigmoidal function using Igor Pro – the appearance energy is the energy value at the intersection between the line tangent to the midpoint of the sigmoid and the x-axis.

Surface-induced unfolding. In the Synapt G2-S*i*, the SID device is located between the Trap and the ion mobility cell.[42] Single charge state precursors were isolated in the manner described in the preceding section. Surface-induced unfolding was performed by increasing the SID acceleration potential in 5 V increments, starting at 20 V (the lowest SID voltage accessible) and continuing until fragmentation was observed. SID on this platform is accomplished by holding the surface at a fixed potential and then raising the potentials of all the instrument optics up to and including the exit electrode of the Trap by changing the "Trap DC Bias" value. Tuning of the entrance optics in the SID device is required to maintain ion transmission while causing the ions to hit the surface. The SID acceleration potential is calculated as the difference between the exit electrode of the Trap and the surface electrode. Minimally-activating conditions in the Trap were used: 5 V potential and 5 mL/min gas flow. Surface-induced unfolding data were analyzed using the procedure described for the collision-induced unfolding data.

Combined unfolding: source + CIU or source + SIU. On the Synapt G2-S*i* platform, activation prior to the quadrupole is readily accomplished by increasing the Sampling Cone voltage near the ion source. This value was set to either 130 V or 175 V for the experiments with BSA to produce mildly or moderately activated precursors, respectively, that were subsequently subjected to either collision- or surface-induced unfolding following the procedures outline above. For the experiments combining in-source activation with SIU, the gas flow in the Trap was reduced to 1 mL/min to minimize any ion heating or cooling in that region.

Monte Carlo and theoretical modeling of CIU. For each protein and charge state studied experimentally, the CIU process was simulated at acceleration voltages from 10-200 V in 5 V increments using argon as the collision gas and two models of the activation process, one with a cooling mechanism and one without. A value of 0.9 was used for the per-collision efficiency of converting center-of-mass frame kinetic to internal energy, based on results for nonapeptides.[206] Gas velocities were sampled from a Boltzmann distribution at a temperature of 298 K, and collision geometries were sampled from an isotropic distribution. The collision probability at each time step was sampled from an exponential distribution consistent with the mean free path of the ion as derived from its CCS and the gas pressure in the Trap. The model for the on-axis electrical potential due to the traveling wave was adapted from Mortensen et al.[207] To avoid undercounting collisions, the simulation time step was set to 1/20th of the mean time between field free collisions at the highest initial kinetic energy for each protein simulated. Additionally, an analytic expression for the total internal energy deposited was derived in the limit of a large number of collisions and averaging over all possible collision geometries and gas velocities:

$$\langle \Delta U^{tot} \rangle = \frac{xNm_i}{m_i+m_g}\langle KE_g^{lab}\rangle + \frac{x(m_i+m_g)\langle KE_{i,0}^{lab}\rangle}{2m_i(1+\sqrt{1-x})+m_g x} \qquad (2)$$

where x is the fraction of available center-of-mass energy converted to internal energy, N is the total number of collisions, m_i and m_g are the mass of the ion and gas, respectively, $\langle KE_g^{lab}\rangle$ is the average kinetic energy of the gas, and $\langle KE_{i,0}^{lab}\rangle$ is the initial kinetic energy of the ion. Further details of the Monte Carlo simulations and derivation of Equation 2 can be found in Appendix B.

Results and Discussion

A major challenge in using SID (and CID) to determine quantitative energetic information is relating the nominal, laboratory-frame kinetic energy to the internal energy deposited into the ion. Because all of these experiments were performed on a Synapt G2-S*i* platform, the "laboratory-frame kinetic energy" (KE^{lab}) is defined here as an ion's charge state multiplied by the voltage difference between either the FSAM-gold surface electrode and the exit electrode of the Trap in SID, or the entrance electrode of the Trap and exit electrode of the quadrupole in CID. The overall SIU or CIU efficiency is defined as the ratio of the initial KE^{lab} and the final internal energy following the collision(s) or interaction with the surface. The relationship between initial KE^{lab} and final internal energy may depend on factors such as the identity of the collision partner and number of collisions, and the mass, size, and shape of the ion.

CIU and SIU access the same unfolding transitions. Using the same instrumentation as for CID of protein complexes, accelerating a native-like protein monomer ion through a buffer gas often causes the ion to unfold and adopt one or more extended conformations at collision energies below those required for fragmentation.[85] The size and shape of these conformations can be assessed by ion mobility spectrometry prior to mass analysis. This technique, termed collision-induced unfolding (CIU), has been demonstrated to yield useful information about a variety of protein structural characteristics.[37,85,97] Analogous protein unfolding using surface activation (surface-induced unfolding, SIU) has not yet been extensively studied. Comparing CIU and SIU for the same protein monomer ions is one approach to better understand the energy deposition and activation process in SIU. Because CID typically partitions charge asymmetrically while SID partitions charge symmetrically, they often yield different products even for protein dimers.[105,190] Since protein ions in CIU and SIU experiments do not significantly change mass or charge, their unfolding products and energies can be more directly compared than dissociation products of protein oligomer ions.

As the first step in calibrating the internal energy deposited by SIU, 10 native-like protein ions, ranging in size from 17-80 kDa, were unfolded using CIU and SIU. Results for three of these, bovine serum albumin (BSA^{15+}, 66 kDa), the N-terminal domain of anthrax lethal factor (LF_N^{10+}, 31 kDa), and transferrin (TF^{18+}, 80 kDa) are illustrated in Figure 10 as examples. For BSA^{15+}, three structural transitions are observed in the CIU "fingerprint" between a native-like and three successively more unfolded conformer families as the nominal KE^{lab} is increased from 300 to 2,775 eV (Figure 10a). In the SIU "fingerprint" one native-like and three unfolded conformer families are observed with the same CCSs as in the CIU experiment, suggesting that the same unfolding transitions to the same unfolded states are taking place in both CIU and SIU of BSA (Figure 10b). Similarly, LF_N^{10+} exhibits unfolding transitions from a native-like to three successively more unfolded conformer families in both CIU and SIU, with virtually identical CCSs in both data sets (Figure 10c,d). In the case of TF, CIU causes a complete transition to the conformer family at approximately 58 nm^2, and only minimal conversion to the conformer family at approximately 62 nm^2 (Figure 10e). However, SIU results in complete transitions to both unfolded conformer families (Figure 10f), consistent with results from the Wysocki group showing that SID/SIU are able to effect greater activation on the timescale of the experiment than CID/CIU at the same $\mathrm{KE}^{\mathrm{lab}}$.[110] Similar CIU and SIU analysis of the remainder of the protein monomers investigated shows that CIU and SIU produce unfolded states with the same CCSs for a variety of proteins and charge states (Figure B1).

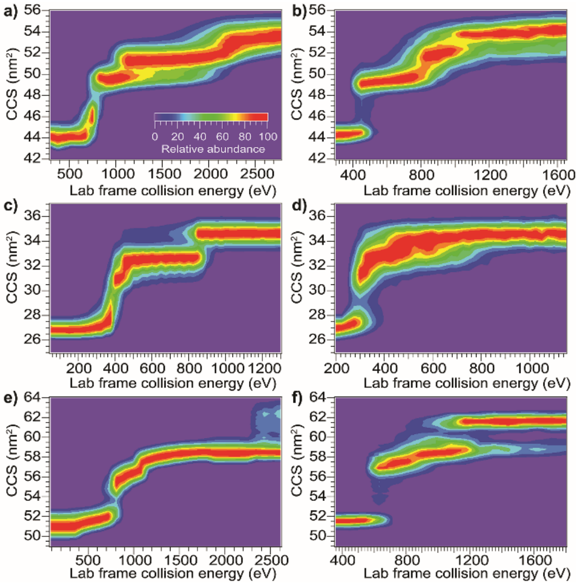

Figure 10. Comparison of CIU and SIU for BSA^{15+}, $\mathrm{LF_N}^{10+}$, and TF^{18+}. **(a)** CIU of BSA^{15+} exhibiting three transitions to unfolded conformer families **(b)** SIU of BSA^{15+} with conformer families at the same CCSs as in CIU **(c)** CIU of $\mathrm{LF_N}^{10+}$ exhibiting three transitions to unfolded conformer families **(d)** SIU of $\mathrm{LF_N}^{10+}$ with conformer families at the same CCSs as in CIU **(e)** CIU of TF^{18+} exhibiting one full transition and the beginning of a second to unfolded conformer families **(f)** SIU of TF^{18+} exhibiting two transitions to unfolded conformer families.

Although CIU and SIU access the same conformer families, they do not produce identical unfolding “fingerprints” as a function of $\mathrm{KE}^{\mathrm{lab}}$. For each of the proteins studied, the CIU and SIU transitions occur at different acceleration voltages and thus different nominal laboratory frame kinetic energies. Additionally, the differences between the lab-frame appearance energies for successive structural transitions are not the same in CIU and SIU. However, defining the transition “appearance energy” as the energy at which the more unfolded conformer is detected (determined as described in the Methods section), extracting appearance energies for each transition, and plotting the nominal SIU energies against the nominal CIU energies reveals a correlation between SIU and CIU appearance energies (Figure 11). The trend is clearly non-linear and can be empirically fit to a power law relationship with an exponent of 0.61 ± 0.05 (energy uncertainties are propagated from the uncertainty in the fit). Some of the scatter in the data set arises from uncertainty in the measurement of SIU or CIU energies (approximately 5%, arising primarily from voltage fluctuations and uncertainty in the sigmoidal fits), but protein-specific factors, such as structure, almost certainly cause deviations from the fitted curve. However, neither the amount of α-helical or β-sheet structure, the number of salt bridges, nor the ratios of CCS to mass, charge to mass, and charge to CCS correlated with deviations from the fitted curve (Figure B6). The implication of the exponent being less than 1 is that SIU is relatively more efficient at causing unfolding than is CIU at higher KE^{lab} values under these instrumental conditions, due to an increase in SIU efficiency, a decrease in CIU efficiency, or some combination of both. Kinetic shifts may be present in both CIU and SIU on this instrument, however, the time for unfolding after activation is likely shorter in SIU because the SID device is located closer to the detector than is the Trap, where CIU occurs. This difference alone should result in a smaller kinetic shift for SIU compared to CIU. Furthermore, if kinetic shift alone were responsible for the non-linear trend observed in Figure 11, the curvature of the trend should be in the opposite direction from what is observed. Thus, other factors beyond kinetic shift dominate the observed trend. The fit also intersects the origin, which implies that any other activation

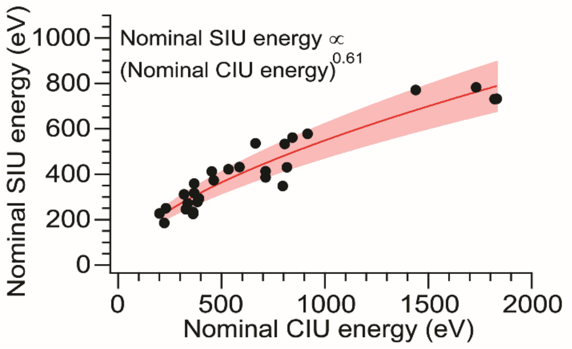

Figure 11. Plot of SIU appearance energy vs. CIU appearance energy for a set of 10 protein monomers. The non-linear trend is fit to a power law relationship with an exponent of 0.61 ± 0.05. The shaded region represents ± one standard deviation of the relative difference from the fit.

taking place that is not a function of the CIU or SIU potential is approximately the same for both processes under the conditions used here.

Calibrating SIU energy deposition by modeling CIU energy deposition. To relate the nominal SIU and CIU energies to the overall internal energy deposited into the ion by each process, the CIU process was modeled and used to calibrate the internal energy scale of the SIU data. The physics of the individual collisions involved in the CID/CIU process have been investigated previously, and a number of theoretical models describing the rate of ion heating and dissociation in multiple-collision CID have been introduced.[208-211] In the Synapt G2-S*i*, in addition to the acceleration potential that injects ions into the collision cell there is a time-dependent electric field (traveling wave potential) that helps elute the ions out of the Trap. In order to model trajectories and energetics for protein ions undergoing CIU it is necessary to add this component to models describing the ion-gas collisions in a field-free environment, e.g., Douglas' model.[209] At the pressures used for CID/CIU in this instrument (approximately 2.6×10^{-2} mbar), these protein ions experience from several hundred to several thousand collisions as they traverse the collision cell. Implementing a Monte Carlo simulation of the collision geometry and distance between collisions (a similar approach to that of Nesatyy and Laskin)[208] enables consideration of both internal energy gain and kinetic energy loss due to energetic collisions.

For all proteins and charge states studied experimentally, the change in internal energy in both the presence and absence of cooling mechanisms is modeled for each 5 V increment of the acceleration potential from 10-200 V. The internal energy change increases linearly with KE^{lab}, and the slope of the trend line gives the overall CIU efficiency (Figure 12). The overall CIU efficiency, defined as the maximum fraction of KE^{lab} converted to internal energy, was found to be approximately 34% and decrease slightly with ion mass in the absence of a cooling mechanism, compared to 25% with a slight increase with ion mass with a cooling mechanism (Figure B2). These values provide upper and lower bounds to the energy deposition, since in our simulations collisional cooling occurs at the maximum possible rate. I expect that the actual amount of energy deposited is close to that computed in the simulations with cooling. When the collisions are highly inelastic (as in these experiments), the traveling wave has a small effect (<2%) on the overall CIU efficiency (Figure B3d), but does contribute to the non-zero intercepts of the plots in Figure 12. Values of the total internal energy change and overall efficiency computed using Equation 2 are in excellent agreement with the results from Monte Carlo simulations without a cooling mechanism (Figure B3a-c).

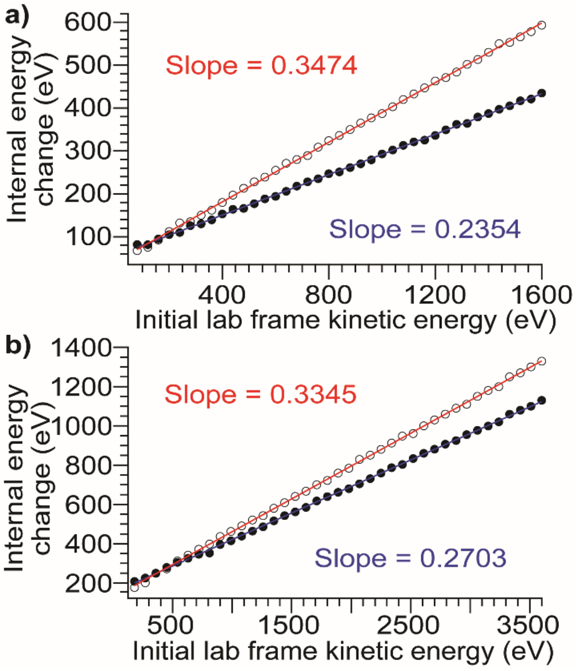

Figure 12. Plots of internal energy change vs. initial laboratory-frame kinetic energy computed from Monte Carlo simulations using models with heating only (open circles, red line) and heating and cooling (filled circles, blue line) for **(a)** β-lactoglobulin^{8+} (**b**) TF^{18+}. These plots are representative and in all cases there is a linear relationship. The slope of the trend line gives the overall CIU efficiency.

Using the computed values for internal energy deposited during CIU (from the simulations with cooling), the energy axis for the data shown in Figure 11 was calibrated (Figure 13), with energy uncertainties in Figure 13 propagated from the uncertainty in the fit. After this re-calibration, it is clear that energy deposition at higher-laboratory frame collision energies is typically more efficient for SIU than for CIU, and SIU is more efficient for high-mass protein ions than for those with lower masses, reaching a maximum of ~68% conversion to internal energy for the highest-energy transitions. (Using the CIU calibration with no cooling mechanism yields a value of ~85%, which I interpret as an extreme upper bound for energy deposition in SIU.) Computational results for collisions of dialanine with an F-SAM surface suggest that a maximum of 16% of initial KE^{lab} remains in translational modes after surface collision,[197] leaving 84% or more of the energy to be partitioned between ion internal modes and the surface; an even lower fraction of the energy remains in translational modes for nanoscale polystyrene latex spheres after surface collision.[212] Our maximum value falls within this upper bound, and suggests that energy transfer to internal modes dominates over energy transfer to the surface under these conditions. The nominal SIU energy vs. calibrated CIU energy trend can be fit to a power law relationship, with an exponent of 0.57 ± 0.04. The fact that the energy scale in SIU can be well-described by relation to CIU data implies that SIU, like CIU, can be understood as a primarily thermal process, in which the observed extent of unfolding in SIU is determined in large part by the amount of energy deposited into and equilibrated among the ion’s internal modes. This result is in

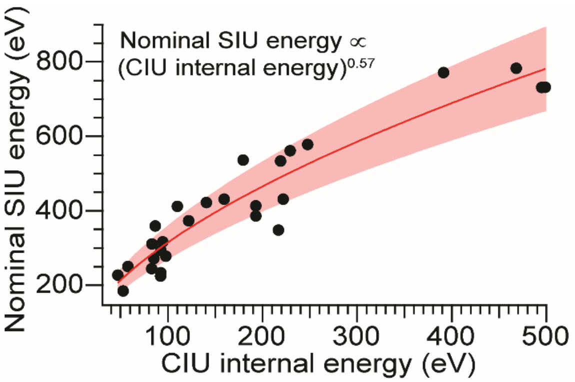

Figure 13. SIU appearance energy vs. rescaled CIU internal energy. The non-linear trend is fit to a power law relationship with an exponent of 0.57 ± 0.04. The shaded region represents ± one standard deviation of the relative difference from the fit.

agreement with the majority of previous experimental and theoretical work on SID of small molecules, peptides, and proteins.[126,127,129,193,194]

Laskin and Futrell showed that in SID of peptides the efficiency of conversion to ion internal energy was approximately 20% and largely invariant to acceleration voltage.[130,195] Thus, increased mass is likely to be primarily responsible for the observed increase in efficiency in our experiments. Previously published results for small molecules and peptides up to 1 kDa have shown that energy deposition efficiency varies little in this size range.[195] The observed increase in overall SIU efficiency with mass in these experiments suggests that proteins of the size studied here fall into a different regime. Note that the SIU energy calibration presented here probes the overall deposition of energy into the ion and not dynamical details of how SIU energy deposition occurs, such as whether the ion interacts one or multiple times with the surface.

In-source activation effects on SIU behavior. Besides mass and initial kinetic energy, other factors that can in principle affect energy deposition in SID are the initial internal energy and structure of the protein ion. In-source ion activation followed by SIU was used to probe the influence of these factors. Applying a cone voltage of 130 V at a backing pressure of 3.7 mbar activates BSA^{15+} as much as possible without causing observable unfolding on the timescale of these experiments (see Figure B8 for full in-source CIU fingerprint). Subjecting this activated precursor to SIU produces a remarkably similar unfolding “fingerprint” to that obtained without in-source activation (Figure 14), and causes a 0.5% to 3.5% change in the unfolding transition appearance energies. Thus, for a precursor with a given CCS, SIU under these conditions does not depend strongly on the degree of activation prior to the surface collision. This is in contrast to CIU, in which ions pre-activated in the source region require less energy to unfold in the Trap (Figure 15), with each transition shifted lower in energy. Interestingly, the size of the shift is the same for the first two unfolding transitions and half as large for the third unfolding transition (Table 1). These data indicate that in CIU ions retain a high internal temperature or already have many of their native non-covalent interactions disrupted as they enter the Trap. Decreased adduction following in-source activation may also contribute to the observed destabilization, as adducts have been shown to have a slight stabilizing effect in CIU,[213-216] and in-source activation in these experiments dissociates approximately 225 Da of adducts. However, for SIU, in-source activation has no significant effect on unfolding appearance energies, suggesting that these ions cool prior to SIU. Minimal cooling is observed for CIU with the same instrumental conditions between the source and the Trap, and SIU following pre-activation in the Trap produces the same result as in-source pre-activation (Figure B9). Thus, cooling of the ions between the source and collision surface in SIU is likely due to collisions with helium or nitrogen leaking from the ion mobility cell.

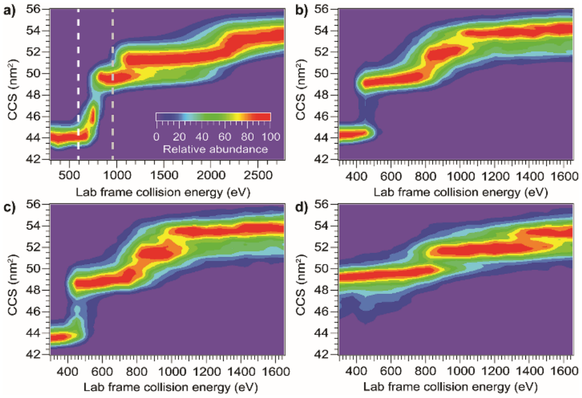

Figure 14. Effect of in-source pre-activation on SIU of BSA^{15+}. **(a)** CIU showing two different levels of in-source activation **(b)** SIU with no source activation **(c)** SIU following in-source activation to the white line in **(a)** does not differ from SIU with no source activation **(d)** SIU following in-source unfolding up to the gray line in **(a)** requires significantly higher energies to cause further unfolding transitions.

Markedly different behavior is observed when the protein monomers studied here were measurably unfolded in the source region prior to SIU. For example, applying a cone voltage of 175 V with a backing pressure of 3.7 mbar causes BSA^{15+} to undergo an unfolding transition to the first unfolded conformer family (Figure 14). The SIU fingerprint of this species is dramatically different from that generated without source unfolding (Figure 14): the KE^{lab} value required to precipitate the second unfolding transition increases by 70 eV, and the third unfolding transition is shifted higher in energy by 170 eV (Table 1). Considering that the ions enter the Trap region partially unfolded, it is remarkable that more energy is required to precipitate the second and third unfolding transitions than without in-source activation, and cooling in the Trap cannot explain these differences. Thus, conversion of kinetic energy of the surface collision to internal energy of the protein must be much less efficient for these initially unfolded, relatively low-charge structures. The differences between the first and second and between the second and third transition appearance energies have increased by approximately 50%, demonstrating that SIU is highly sensitive to the structure of the precursor ion; a 12% increase in CCS leads to this dramatic reduction in the energy deposition efficiency. In simulations of triglycine SID, folded and extended structures differed little in energy deposition efficiency,[196] again indicating that proteins of the size studied here fall into a different regime than peptides.

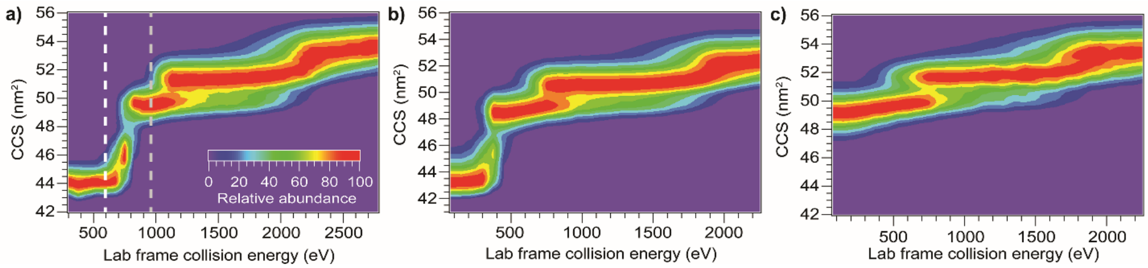

Figure 15. Effect of pre-activation on CIU of BSA^{15+}. **(a)** CIU showing two different levels of in-source activation **(b)** Unfolding transitions in CIU following in-source activation up to the white line in **(a)** are shifted to lower energies **(c)** Unfolding transitions in CIU following in-source unfolding up to the gray line in **(a)** are shifted to lower energies.

Contrasting behavior is observed in CIU, where in-source unfolding followed by CIU causes the second and third unfolding transition appearance energies to decrease by 628 and 490 eV, respectively (Table 1). These results agree with those for in-source activation without unfolding followed by CIU, and demonstrate that overall internal energy deposition efficiency for these ions in CIU depends on ion CCS to a much lesser extent than in SIU. This conclusion is supported by calculations of the overall CIU efficiency with cooling included, which show that although overall CIU efficiency depends non-linearly on CCS and has its maximum at the experimental CCS value of the native-like conformation (Figure B4), changing the CCS of BSA^{15+} by the amounts observed experimentally changes the overall CIU efficiency by only 1-5% (Figure B5). Simulations of collisional activation of peptides do show a small decrease in energy transfer for extended structures, a finding consistent with our results.[217] SIU of pre-activated TF^{18+} provides a corroborating result, with in-source unfolding causing the appearance energy of the next transition to increase significantly (Figure B10).

Table 1. Appearance energies for CIU and SIU with in-source activation

Activation method	Sampling cone voltage	Appearance energies (eV) 1	2	3
CIU	25 V	713	916	1731
	130 V	296	514	1518
	175 V		288	1241
SIU	25 V	386	578	783
	130 V	377	598	779
	175 V		649	953

These results suggest at least two mechanisms that contribute to the reduction in energy deposition efficiency for unfolded proteins in SIU (Figure 16). First, the effective protein-surface CCS can be smaller for unfolded proteins than for folded proteins, even though the protein-gas CCS is larger. That is, in many cases, an ion that is more elongated will on average interact with a smaller area of the surface than an ion with the same mass that is compact (Figure 16). This reduces the effective center-of-mass frame kinetic energy of the collision and thus decreases the amount of energy transferred to internal modes. The increased flexibility of the unfolded protein ions in these experiments relative to the compact, native-like conformers likely also contributes to the lower energy conversion efficiency, because energy can be more efficiently transferred into rotational motion for more elongated structures.[217] As rotation is less efficient than vibrational energy at causing further unfolding,[218] this will increase the amount of KE^{lab} required to cause further unfolding. Multiple interactions of the ion with the surface may further complicate energy deposition.

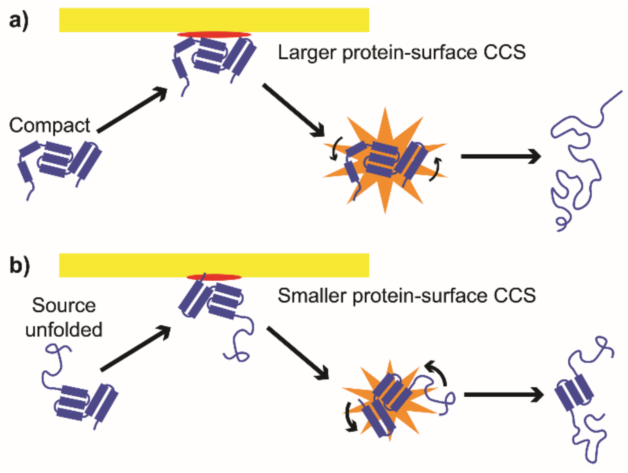

Figure 16. Effective protein-surface CCS is larger and transfer to rotational modes less efficient for **(a)** compact structures than for **(b)** unfolded structures, causing energy deposition efficiency to be higher for compact structures.

Conclusions

The energy deposition process in SID of proteins was studied by comparing unfolding of protein monomers by collisional and surface activation and by investigating the effect of in-source pre-activation on CIU and SIU. CIU and SIU cause similar unfolding transitions and the conformer families observed have the same CCS. The nominal energy scales of CIU and SIU are correlated and follow a power law relationship, with SIU being more efficient than CIU at higher KE^{lab} values and for larger ions, but significant scatter from this trend indicates other protein-specific factors also play a significant role, although no correlations in deviations from the trend was found with respect to secondary structure content, number of salt bridges, or the ratios of charge to mass, charge to CCS, or CCS to mass. These factors may be structural or may be related to the mechanical protein-surface interaction. The average overall efficiency for conversion of initial KE^{lab} to internal energy for CIU determined by Monte Carlo simulation including both ion heating and cooling is approximately 25%, increasing slightly with ion mass. These calculated data are used to calibrate the SIU energy scale, leading to computed efficiency values for SIU of up to 68% for the largest ions studied (80 kDa). Alternatively, this is equivalent to the effective mass of the surface during the collision, defined as the mass of the effective two-body collision partner required to impart a center-of-mass frame energy equal to the calibrated CIU internal energy,[127] increasing with protein size. Previous determinations of the effective mass of the surface in peptide SID experiments were a few tens of Da,[126,127] a result corroborated by atomistic simulations of peptide SID showing that the peptide interacts with a single $-CF_3$ group (mass of 69 Da).[197] My data suggest that the effective mass of the surface grows with the mass of the protein (Figure B11).

When in-source pre-activation is followed by CIU, for both degrees of in-source activation (unfolded and not unfolded), subsequent unfolding transitions are shifted to lower energies by an amount commensurate with the amount of in-source activation. This indicates that effects of activation, i.e. an elevated internal temperature or disruption of non-covalent interactions, can be preserved as the protein ions travel from the source region to the entrance of the Trap. In contrast, pre-activation without unfolding has little effect on SIU, indicating that protein ions are cooled between the end of the Trap and the SID device. Protein ions unfolded in the source require significantly more energy to further unfold in SIU than their compact counterparts, showing that energy deposition in SID is sensitive to ion CCS, with reduced conversion efficiency for more unfolded ions due to a smaller effective protein-surface CCS and increased transfer to rotational modes. The Wysocki group has combined in-source activation with SID of protein tetramers and demonstrated that when partially-unfolded complexes are subjected to SID they produce fragments akin to those produced by CID.[219] The results obtained here parallel those and provide quantitative insights into the effect of structure on the SID energy deposition process. Future experiments probing the energy required to dissociate pre-activated protein complexes could elucidate how the effects demonstrated here change with varying complex size and number of subunits. I anticipate that calibration of energy deposition in SID using a strategy similar to that reported here may enable more quantitative calibration of SID appearance energies with respect to the disrupted protein-protein interfacial areas, facilitating rapid characterization of protein-protein interactions in previously unexamined complexes, including membrane protein complexes. Future investigation of the role of protein structure as well as mechanical effects of the surface collision, including those revealed by sophisticated chemical dynamics simulations,[220] are expected to shed light on protein-specific deviations from the SIU-CIU calibration curve described here.

Beyond determining the efficiencies of kinetic to internal energy conversion in CIU and SIU, it is of interest to determine thermodynamic parameters for gas-phase protein unfolding. In order to do so it is necessary to know the internal temperature of the ion and the reaction time. The model for collisional activation introduced in this chapter allows both to be determined. Therefore, it can enable quantitative studies using CIU/CID. In Chapter IV I describe and validate a quantitative method for determining activation energies for protein unfolding and dissociation and discuss intriguing common features of gas-phase protein unfolding.

CHAPTER IV

RAPID DETERMINATION OF ACTIVATION ENERGIES FOR GAS-PHASE PROTEIN UNFOLDING AND DISSOCIATION IN A Q-IM-TOF MASS SPECTROMETER

Reprinted with permission from Donor, M. T.; Shepherd, S. A.; Prell, J. S. Rapid Determination of Activation Energies for Gas-Phase Protein Unfolding and Dissociation in a Q-IM-ToF Mass Spectrometer. *J. Am. Soc. Mass Spectrom.* **2020**, *31*, 602-610.
Copyright 2020 American Chemical Society.

Introduction

The ability of electrospray ionization (ESI) to gently transfer folded proteins to the gas phase and preserve native-like structure and non-covalent interactions, in conjunction with global size measurement using ion mobility (IM), has led to the emergence of native ion mobility-mass spectrometry (IM-MS) as an important structural biology tool.[144] Particularly, perturbation of protein or complex structure *via* gas-phase activation followed by IM-MS analysis has led to valuable insights in an ever-growing number of cases,[99,109,221-223] such as recent experiments using IM-MS to identify specific membrane protein-lipid interactions.[224]

One of the most common methods for interrogating protein structure in the gas phase is collision-induced dissociation/collision-induced unfolding (CID/CIU). While CID can be performed on many types of mass spectrometers, CIU is typically undertaken in an ion mobility-time-of-flight mass spectrometer. In both CID and CIU, protein ions accelerated to a high initial kinetic energy experience many (hundreds to thousands for proteins) collisions with neutral gas atoms or molecules that slowly heat the ions, leading to dissociation (CID) or unfolding (CIU) of a portion of the protein or assembly. CID of protein complexes can provide information about the identity of subunits and overall complex stoichiometry.[86] Pioneering work by the Ruotolo group has shown that CIU can reveal details of protein structure,[85] including the number of domains,[37] disulfide binding patterns,[97] and location and cooperativity of ligand binding sites.[100] However, the relationship between the initial kinetic energy and quantitative parameters such as the activation energy of dissociation/unfolding has not yet been established. This has limited comparisons between both gas-phase energies for different species and gas- and solution-phase energetics. Also unknown at this stage are the exact unfolded structures, any common features of unfolded structures arising from different compact structures, and the pathway(s) by which they are reached.

Activation energies for the dissociation of many peptide and small protein ions can be accurately and precisely determined in the gas phase using blackbody infrared radiative dissociation (BIRD).[115,118,119] In BIRD, implemented in an FT-ICR, ions in an ultrahigh vacuum environment are heated by absorption of blackbody photons emitted from the walls of the ICR cell, which is equilibrated to a specific temperature. The abundance of fragment ions can be measured at a set of reaction times to determine the rate constant at a given temperature. Repeating at multiple temperatures allows the activation energy to be determined using the Arrhenius equation. However, measuring ion unfolding energetics with BIRD is extremely challenging, because it is difficult to measure the ion shape and size distribution after activation in an FT-ICR cell.

Additionally, the amount of time required to equilibrate the temperature of the FT-ICR cell between measurements can be many minutes, and, depending on the size of the molecule in question, master-equation modeling may be needed to extract accurate and precise thermodynamic information.[116]

Various other methods have been used to determine quantitative gas-phase energetic information, including single-collision threshold CID,[131,133] calibration using a range of "thermometer" ions such as metal carbonyls,[225] hydrated metal ions,[226,227] aromatic species,[228-230] and small peptides,[117,231] multiple-collision CID,[125,127,128] and surface-induced dissociation (SID).[127,129,130] Many of these methods, particularly the latter two, require quantum mechanical computation of accurate vibrational levels, which are used in microcanonical Rice-Ramsperger-Kassel-Marcus (RRKM) modeling to determine absolute dissociation energies from experimental data.[125,127,128] Energetic information obtained using the methods described above has provided fundamental insights into ionization,[228,229,232] activation,[125,226,227] and dissociation properties,[117,130,199] as well as structural information.[118,233,234] Although these approaches have proven fruitful for the study of small peptides, they have not yet been applied to proteins due to the difficulty of the computations involved. Development of a rapid method that allows determination of absolute energies for protein unfolding and dissociation without requiring an FT-ICR or quantum mechanical calculations would open a critical class of biomolecules to more fundamental study.

Here, I present a method for determining activation energies for protein unfolding and complex dissociation from CIU and CID experiments performed on a Waters Synapt G2-S*i* Q-IM-ToF mass spectrometer. Using a previously-developed model for energy deposition in collisional activation[235] to calibrate the internal temperature enables the activation energy to be determined using either the Arrhenius or Eyring equation and pseudo-first-order reaction kinetics. Activation energies determined for heme loss from myoglobin and subunit dissociation from streptavidin and Shiga toxin 1 are in good agreement with values from BIRD experiments, validating our model. Also reported is the first gas-phase determination of unfolding activation energies for several monomeric proteins. Average $\Delta G^{\ddagger}$ values fall within a narrow range for a variety of proteins and charge states, depend more strongly on charge density than on protein identity, and are consistent with energies computed for proton transfer in small peptides from basic residues to the amide backbone. These factors combine to suggest that the rate-limiting step in gas-phase protein unfolding is proton transfer to an exposed region. This procedure provides a facile, rapid method to measure activation energies for gas-phase protein unfolding and dissociation and yields insight into the mechanism of CIU.

Methods

Sample preparation. Myoglobin, streptavidin, Shiga toxin 1 B subunit, β-lactoglobulin, concanavalin A, carbonic anhydrase II, alcohol dehydrogenase, bovine serum albumin, and transferrin were purchased from Sigma Aldrich. Lyophilized proteins were reconstituted in ultrapure (18 MΩ) water before buffer-exchange into 200 mM ammonium acetate, pH 7-7.5 (native-like, positive and negative polarity); 180 mM ammonium acetate 20 mM triethylammonium acetate (TEAA), pH 7 (charge-reduced, positive polarity); or 160 mM ammonium acetate 40 mM TEAA, pH 7 (charge-reduced, positive polarity). Myoglobin was prepared in an 80/20 water/methanol solution to match the conditions used in literature BIRD experiments.[120]

Native IM-MS and CID/CIU. Ion mobility-mass spectra were acquired using a Synapt G2-S*i* ion mobility-mass spectrometer (Waters Corp.) equipped with a nanoelectrospray source. A Flaming-Brown P-97 micropipette puller (Sutter Instruments) was used to pull nanoelectrospray emitters from borosilicate capillaries with an i.d. of 0.78 mm to a final i.d. of approximately 1 μm. Samples were electrosprayed by applying a potential of ±0.7-1.1 kV to a platinum wire in electrical contact with 3-5 μL of solution in the emitter. "Sensitivity" mode and traveling wave velocities of 450-550 m/s and heights of 20-25 V were used for all experiments. The source block was equilibrated to ambient temperature, nitrogen was used as the mobility gas at a flow rate of 50 mL/min, and helium and argon (in the "Trap" collision cell) flow rates were 100 mL/min and 5 mL/min, respectively. Measured arrival time distributions were converted to collisional cross sections following an established literature procedure,[77,161] using cytochrome C, β-lactoglobulin, avidin, bovine serum albumin, concanavalin A, and alcohol dehydrogenase as calibrants. Negative ions were assigned a collisional cross section (CCS) value equal to that of the positive ion of the same protein with the same number of charges – e.g. BSA^{14-} and BSA^{14+} are assumed to have the same CCS. A comparison of CCS values in positive and negative polarity showed that CCS differences between the two polarities are negligible for native-like ions.[236]

For collision-induced unfolding (CIU) experiments, a single charge state was isolated using the quadrupole and the ion unfolded by modulating the acceleration voltage into the Trap (Trap CE), beginning below the threshold for unfolding and increasing in 1 V increments until the most compact conformer family disappeared or a quasi-equilibrium was reached. Collision-induced dissociation (CID) experiments were performed similarly, with the criteria for the upper and lower bounds of Trap CE being the appearance of measurable product monomer(s) and disappearance of measurable precursor, respectively.

Theory. In order to determine quantitative activation energies from dissociation or unfolding kinetics data, the rate constant and effective temperature must be known. I previously published a model for collisional activation in a Synapt G2-Si that can be used to determine the effective temperature for a protein ion at a given collision energy.[235]

$$T = T_0 + \frac{x \cdot z \cdot e \cdot V}{3 \cdot N_{at} \cdot k_B} \tag{3}$$

where T_0 = 298 K is the initial ion temperature, x is the overall fraction of initial kinetic energy converted to internal energy (computed using our Monte Carlo simulation approach), z is the number of charges, e is the fundamental charge, V is the collision voltage, N_{at} is the number of atoms in the protein, and k_B is the Boltzmann constant. Assuming pseudo-first-order kinetics for these unimolecular reactions, the rate law will be given by

$$[R]_t = [R]_0 e^{-kt} = [R+P]e^{-kt} \tag{4}$$

where $[R]$ is the abundance of the precursor ion, $[R+P]$ is the total abundance of precursor and product ions, k is the rate constant, and t is the reaction time. Rewriting this expression in terms of the rate constant gives

$$k = -\frac{1}{t} \cdot \ln \frac{[R]_t}{[R]_0} = -\frac{1}{t} \cdot \ln \frac{[R]_t}{[R+P]} \tag{5}$$

The reaction time cannot be directly measured in a Synapt G2-Si, unlike in an FT-ICR, but it can be estimated from our simulations of collisional activation. The ions enter the Trap collision cell with high velocity, but quickly slow down as most of the kinetic to internal energy conversion occurs in the early portion of the Trap. I take the ion’s final velocity exiting the Trap (typically 200-250 m/s, slightly below the 300 m/s traveling wave velocity in the simulations) as representative of the velocity of the ions after energy deposition, which primarily occurs in the first third of the Trap, and estimate that the ions traverse a distance of 20 cm ± 5 cm (the majority of the length of the Trap, plus the SID device and the distance between the SID device and the helium cell, where unfolding/dissociation is effectively quenched) following activation. From those values, an estimated reaction time can be determined, values for which are typically ~800 microseconds. Although the uncertainty associated with this time is large (~25%), it has only a small impact on the calculated activation entropy, contributing an uncertainty of 0.5-2% to the final value. With the effective temperature and rate constant determined, activation energies can be computed.

The Arrhenius equation, used in a number of BIRD studies,[115,118,119] provides an empirical relationship between the rate constant, k, and the temperature, T

$$k = Ae^{-E_a/k_B T} \tag{6}$$

where A is the pre-exponential factor, and E_a is the activation energy. This can be rearranged to

$$\ln k = \ln A - \frac{E_a}{k_B T} \tag{7}$$

Substituting the expression for the rate constant, Equation 5, into Equation 7, gives the following expression

$$\ln\left(-\frac{1}{t} \cdot \ln \frac{[R]}{[R+P]}\right) = \ln A - \frac{E_a}{k_B T} \tag{8}$$

which simplifies to

$$\ln\left(-\ln \frac{[R]}{[R+P]}\right) = \ln A + \ln t - \frac{E_a}{k_B T} \tag{9}$$

The activation energy is then the slope of a linear fit of Equation 9.

The Eyring equation, which has a firmer theoretical justification than the Arrhenius equation,[237] also relates the rate constant and the temperature

$$k = \frac{k_B T}{h} e^{-\Delta G^{\ddagger}/k_B T} \tag{10}$$

where h is Planck's constant and $\Delta G^{\ddagger}$ is the Gibbs free energy of activation. It can be re-written as

$$k = \frac{k_B T}{h} e^{\Delta S^{\ddagger}/k_B} \cdot e^{-\Delta H^{\ddagger}/k_B T} \tag{11}$$

where $\Delta S^{\ddagger}$ is the activation entropy and $\Delta H^{\ddagger}$ is the activation enthalpy. This can be rearranged to

$$\ln \frac{k}{T} = -\frac{\Delta H^{\ddagger}}{k_B T} + \ln \frac{k_B}{h} + \frac{\Delta S^{\ddagger}}{k_B} \tag{12}$$

Substituting Equation 3 for the rate constant into Equation 10 gives

$$\ln\left(\frac{-\ln\frac{[R]}{[R+P]}}{t \cdot T}\right) = -\frac{\Delta H^{\ddagger}}{k_B T} + \ln \frac{k_B}{h} + \frac{\Delta S^{\ddagger}}{k_B} \tag{13}$$

which can be rearranged to give

$$\ln\left(\frac{-\ln\frac{[R]}{[R+P]}}{T}\right) = -\frac{\Delta H^{\ddagger}}{k_B T} + \ln \frac{k_B}{h} + \ln t + \frac{\Delta S^{\ddagger}}{k_B} \tag{14}$$

The activation enthalpy is then obtained from the slope of a linear fit to Equation 14, and the activation entropy from the intercept.

CID data analysis. Relative abundances of the product monomer(s) and precursor were computed by integrating the respective peaks in MassLynx 4.1 (Waters Corp.). At each Trap CE the natural logarithm of the negative of the natural logarithm of the precursor relative abundance was taken to yield the y-axis data for Arrhenius analysis. The effective temperature, computed using Equation 3, was multiplied by the Boltzmann constant and the reciprocal of the result taken to yield the x-axis data. The two data sets were plotted against one another and a linear least-squares fit performed. The slope of the linear fit was used to determine the activation energy, according to Equation 9.

CIU data analysis. Arrival time distributions for each CIU experiment were extracted using TwimExtract,[238] and further data analysis performed in Igor Pro (WaveMetrics). Briefly, at each Trap CE the relative abundances of each conformer family were determined by fitting the arrival time distribution with one Gaussian function for each observed local maximum and computing the relative abundances from the area under each Gaussian. At each Trap CE the negative of the natural logarithm of the relative abundance of the most compact conformer family was divided by the effective temperature determined using Equation 3 and the natural logarithm of the result taken to yield the y-axis data for Eyring analysis (see below for an example of this procedure). The x-axis data was obtained by taking the reciprocal of the effective temperature multiplied by the Boltzmann constant. The two data sets were plotted against one another and a linear least-squares fit performed. Data points corresponding to relative abundances below 1% for either the compact or unfolded conformer families were excluded from the analysis. Equation 14 was used to determine $\Delta H^{\ddagger}$ from the slope of the linear fit, and $\Delta S^{\ddagger}$ from the intercept. $\Delta G^{\ddagger}$ was determined from $\Delta H^{\ddagger}$, $\Delta S^{\ddagger}$, and the average effective temperature over the range of data included in the fit.

Results and Discussion

Comparison of our results with BIRD data. Although BIRD has frequently been used to study peptide fragmentation, only a handful of small protein systems have been investigated, most prominently the three referenced here: loss of heme from myoglobin,[120] and dissociation of a monomer from streptavidin tetramers and Shiga toxin 1 B pentamers, respectively.[121] Representative mass spectra for each protein can be found in the Supporting Information (Figures C1, C2, and C3). For all species studied, the primary dissociation pathway is the same as that reported in the literature, and no secondary dissociation is observed at the collision voltages used in these experiments. For each protein and charge state, plots of $\ln(k)$ vs. $\frac{1}{k_BT}$ were generated following the procedure described above. Data for one charge state of each protein is shown in Figure 17, and the rest are collected in Figure C4.

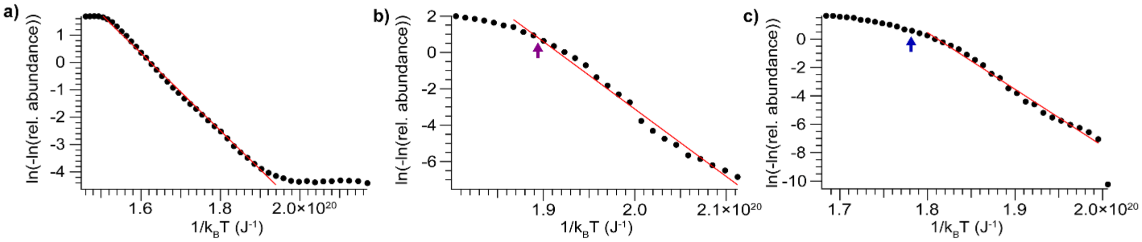

Figure 17. Plots of the double natural logarithm of precursor relative abundance versus inverse vibrational temperature for **(a)** myoglobin, 10+ **(b)** Shiga toxin 1, 12+ **(c)** streptavidin, 14+. The purple arrow in **(b)** indicates the end of the data set reported by Sinelnikov et al.,[121] while the blue arrow in c) indicates the approximate location of the inflection point observed by Sinelnikov et al.[121]

For myoglobin, 10+, a small amount of the apo form is present even at very low collisional activation. For this ion, there is a small amount of activation due to the isolation in the quadrupole (Figure C5), and a small population (< 1% abundance) that dissociates readily with minimal activation. This leads to the flat region of the graph in Figure 17a, prior to the remaining population reaching the threshold for dissociation, after which point the plot exhibits a linear relationship, allowing Arrhenius parameters to be determined. For both streptavidin, 14+ and Shiga toxin 1, 12+, the relationship between $\ln(k)$ and $\frac{1}{k_BT}$ is linear at lower levels of collisional activation (i.e. higher $\frac{1}{k_BT}$) and exhibits some curvature at higher levels of activation. This curvature is likely caused by multiple non-interconverting populations with different reactivities, and/or rearrangement to a more stable conformer family upon activation. Sinelnikov et al., using an FT-ICR, also observe some degree of curvature in Arrhenius plots for streptavidin when little of the precursor remains, which they attribute to the presence of multiple, differently-reactive populations.[121] For streptavidin, 14+, scrutiny of their data reveals that the transition point occurs at approximately the same ratio of precursor to products as in this study.[121] For Shiga toxin 1, 12+, within the range of precursor abundances studied by Sinelnikov et al. our data are linear. Thus, fitting the initial linear portion of our data provides a reliable basis for a comparison between the energies determined here and those acquired using BIRD; this comparison is presented in Table 2.

Table 2. Comparison of activation energies obtained using our method and BIRD.

Protein	Charge	E_a (kJ/mol)	BIRD E_a (kJ/mol)
Myoglobin	9+	92±7	87±10[a]
Myoglobin	10+	85±7	87±10[a]
Shiga toxin 1	11+	263±21	264±9[b]
Shiga toxin 1	12+	223±14	217±5[b]
Shiga toxin 1	13+	208±18	193±5[b]
Streptavidin	14+	240±15	262±9[b]
Streptavidin	15+	224±14	230±10[b]

[a]Gross et al.[120] [b]Sinelnikov et al.[121]

For four of the seven species studied, the two values of activation energy are in excellent agreement and are within 3% of each other, while in the remaining cases the discrepancy is less than 10%. In all cases the activation energy determined by our method and by BIRD are within uncertainty of each other, validating our combined experimental and computational approach. These results also demonstrate that, for proteins, quantitative energetic information can be obtained without the need for explicitly computing vibrational modes of the system or microcanonical RRKM rate constants. The long-term reproducibility of this method was assessed and found to be good, with experiments conducted across several months producing relative standard deviations in E_a below 5% (Table C1). It is important to note that obtaining stable, gentle electrospray with minimum non-specific adduction is key to producing reliable data for this method. Another potential source of error is *m*/*z*-, charge-, and CCS-dependent transmission efficiencies. Abundance of protein monomers in the *m*/*z* and voltage ranges examined here typically varies by ±10% (Figure C6). In the CID experiments, the sum of the abundances of the precursor and product monomers is nearly constant, whereas the sum of the precursor and product (n-1)-mers abundances decreases with increasing collision voltage (i.e. the (n-1)-mer is suppressed). Thus, the monomer is treated as representative of the true abundance of the products; any discrepancies introduced by this approach are likely small (see Table C2). This approach may break down in cases where the precursor and products are more discrepant in *m*/*z*, owing to greater differences in transmission efficiency, and it is important to evaluate the effect of transmission efficiency for each new ion of interest.

The timescale of this method (a set of experiments can be performed in minutes) and its relatively low computational demands provide key advantages relative to other, more rigorous, approaches. Importantly, it is also applicable to the study of a broad range of species, including very large protein complexes and protein unfolding. Other biological macromolecules such as oligonucleotides could also be probed given suitable characterization of the collision physics. Our method rests on several assumptions, including that the protein ions studied have an effective heat capacity that scales linearly with mass, that the ions reach an elevated effective internal temperature following activation, and that they remain at or near that elevated effective temperature until rapid cooling in the helium cell. Considering those assumptions in order, the proteins studied here are large enough that the density of states is much closer to a continuum than for small analytes such as peptide ions, and thus their heat capacity will depend primarily on the number of vibrational modes, which is roughly proportional to mass. The Williams group, among others, has shown that activation *via* multiple collisions can produce ions with an effective temperature comparable to that produced in BIRD experiments.[124] Our simulations indicate that, when collisional cooling is included in the model, ion internal energy remains roughly constant (within a few percent) following an initial, sharp increase (i.e. collisional cooling and heating nearly balance under the conditions considered).[235] Factoring in the good agreement between BIRD and our method suggests that our method, while not as precise as BIRD, can provide relatively accurate, quantitative thermodynamic information.

Thermodynamics of gas-phase protein unfolding. The validated method was then used to investigate the energetics of gas-phase protein unfolding for a broad variety of protein ions. A set of monomeric proteins ranging in size from 18-80 kDa were subjected to CIU using both positive and negative polarities. For each protein, multiple charge states were unfolded, including both native-like and charge-reduced species in positive polarity. (Charge states in negative polarity are generally lower than in positive polarity, e.g. for transferrin the highest charge states are 16− and 19+ in negative and positive polarity, respectively.) Overall, ions with an equal number of charges unfold similarly in positive and negative polarity, but not identically, in agreement with a recent report.[239] Data for the unfolding of the most compact conformer family were analyzed according to the method described above, and shown in Figure 18.

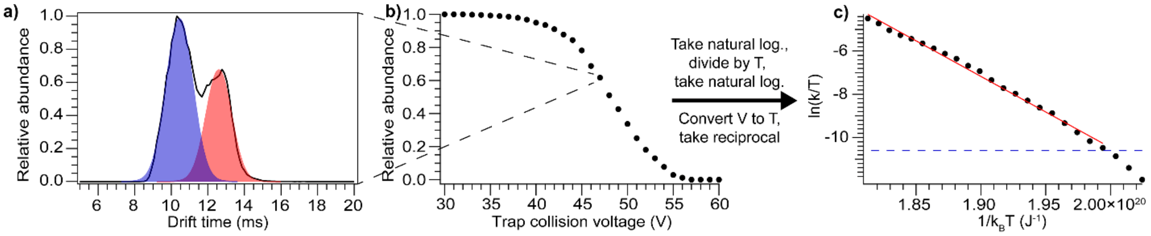

Figure 18. Data analysis scheme, using bovine serum albumin, 16+ as an example. **(a)** Drift time distribution at selected Trap collision voltage (47 V) showing two coexisting conformer families. **(b)** Relative abundance of most compact conformer family for the set of Trap collision voltages, which is transformed to **c)** Plot of natural logarithm of effective rate constant divided by temperature versus inverse energy. The linear fit gives the activation enthalpy and entropy, and the dashed blue line shows the threshold for quantitation (>1% unfolded conformer family).

Eyring plots (the natural logarithm of the effective rate constant divided by the temperature, plotted versus inverse vibrational temperature) for two representative species, alcohol dehydrogenase (ADH), 12+, and concanavalin A (Con A), 8+, are shown in Figure 19. ADH, 12+ unfolds such that the most compact conformer family is completely depleted (Figure 19a), while Con A, 8+ reaches a quasi-equilibrium between the most compact and unfolded conformer families, giving rise to the plateau observed in the Eyring plot (Figure 19b). Eyring plots for the remaining species are collected in the SI (Figure C7 and Figure C8). In some cases, the data exhibit curvature at lower abundances (typically <10%) of the most compact conformer family. In these cases, I fit the initial linear portion of the data. As discussed above, this curvature may arise from multiple non-interconverting populations with different reactivities, and/or rearrangement to a more stable conformer family upon activation. In these CIU experiments, any such rearrangement necessarily must not produce a measurable ΔCCS (i.e. < 3%). Given that the decrease in reactivity tends to manifest when little of the most compact conformer family remains, I expect that it is due to structural rearrangement to a more stable species with similar CCS. Therefore, fitting the initial linear portion of the curves will provide information about the kinetics of the initial compact conformer family, prior to rearrangement.

Activation enthalpies and entropies extracted from the linear fits are plotted against each other in Figure 20 (activation parameters can be found in Tables C3 and C4). Remarkably, for both polarities there is a strong linear correlation between ΔH‡ and TΔS‡, one that falls on a line of nearly constant ΔG‡. Higher ΔH‡ values for these data are (in general) associated with relatively lower charge states. Interestingly, a correlation between ΔH‡ and ΔS‡ was also noted by Sinelnikov et al. in their BIRD studies of protein complex dissociation.[121] A possible cause of this correlation is that a structure with a more tightly-bound proton may have a lower ground-state entropy and thus a larger change in entropy upon conversion to the transition state for the unfolding/dissociation process. In Figure 20a, four data points lie significantly above the remaining data and do not fit the linear trend. These data arise from the lowest charge-state cations for which measurable unfolding is observed in our instrument for four

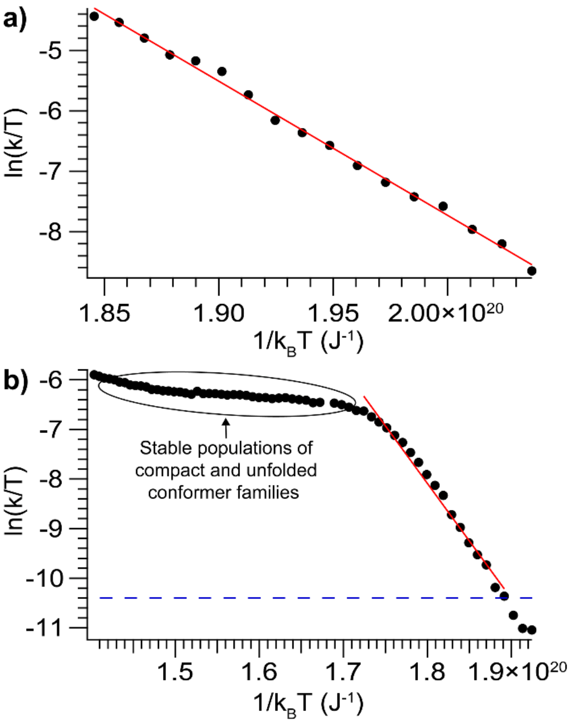

Figure 19. Plots of the natural logarithm of the effective rate constant divided by temperature versus inverse vibrational temperature for **(a)** alcohol dehydrogenase, 12+ **(b)** concanavalin A, 8+, which does not unfold fully, leading to the plateau apparent in the plot. The blue dashed line shows the threshold for quantitation (>1% unfolded conformer family).

proteins (concanavalin A, carbonic anhydrase, alcohol dehydrogenase, and bovine serum albumin). Furthermore, all of these are species that do not fully convert from the most compact conformer family to a more unfolded one, but instead reach a quasi-equilibrium with two coexisting populations.

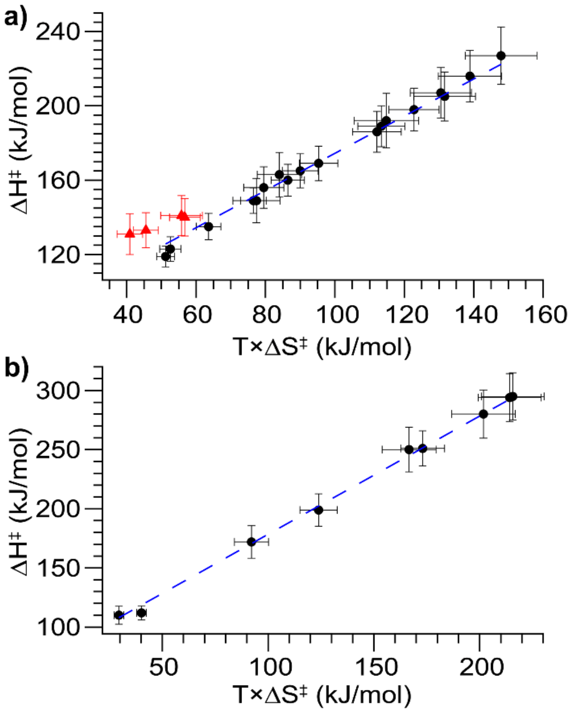

Figure 20. Plots of $\Delta H^{\ddagger}$ versus $T\Delta S^{\ddagger}$ for **(a)** positive and **(b)** negative ions. The black circles are species that fully unfold, the blue dashed lines are lines of constant $\Delta G^{\ddagger}$ (i.e. a slope of 1, best fit lines have slopes of 1.07±0.02 in **(a)** and 1.02±0.02 in **(b)**), and the red triangles are species that reach a quasi-equilibrium between the compact and unfolded states (only observed for positive ions). Notably, these species also have markedly larger $\Delta G^{\ddagger}$ than the rest of the species studied.

These species all have markedly higher $\Delta G^{\ddagger}$ values than the rest of the positive ions studied and are the only ones with $\Delta G^{\ddagger}$ above 80 kJ/mol (Figure 21). They also have lower $\Delta H^{\ddagger}$ values than do the same proteins with one more proton, which may indicate a different unfolding mechanism at work for these species. Interestingly, this behavior is not observed for negative ions with the same absolute charge as the outlier species. Instead, all the negatively-charged species investigated fall along the linear trend of $\Delta H^{\ddagger}$ vs. $T\Delta S^{\ddagger}$. The rest of the positively-charged ions measured have $\Delta G^{\ddagger}$ between 70 and 80 kJ/mol, except for Con A^{10+} at 68 kJ/mol (Figure 21). The negatively-charged ions are more unfolded at a given collision voltage in the majority of cases (Fig. C10) and have $\Delta G^{\ddagger}$ values slightly below or approximately equal to the equivalent positively-charged ions, with the single exception of BSA^{14-}

/BSA^{14+} (Figure 21). These results are intriguing in light of a recent study that found negatively-charged complexes to be more resistant to CID.[239] For all proteins studied and both polarities, the lowest charge state has the largest ΔG‡, and ΔG‡ decreases monotonically with increasing charge state.

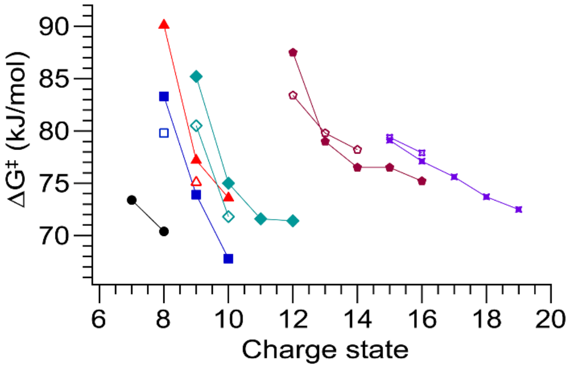

Figure 21. Plot of ΔG‡ versus charge state for positive (filled symbols) and negative (open symbols) ions of β-lactoglobulin (black circles), concanavalin A (blue squares), carbonic anhydrase II (red triangles), alcohol dehydrogenase (teal diamonds), bovine serum albumin (maroon pentagons), and transferrin (purple stars). For a given protein, ΔG‡ decreases nearly monotonically with increasing charge state.

Implications for unfolding mechanism. Since the measured ΔG‡ values for a diverse variety of structurally unrelated proteins fall within a narrow range of energies, and ΔG‡ varies more with charge state for a single protein than across proteins, protein and sequence identity are unlikely to be the main determining factors in the unfolding energy. Nor is the size of the unfolding portion of the protein (for which ΔCCS is a proxy) likely to be a major factor, as ΔG‡ varies less across these proteins than does ΔCCS. Instead, the data suggest that charge state plays a vital role. This is borne out by a plot of ΔG‡ against charge density (here, number of charges divided by CCS), which demonstrates a clear negative correlation between ΔG‡ and charge density for positively-charged ions ($R^2 = 0.77$, excluding the four outlier data points. $R^2 = 0.54$ if they are included) (Figure 22a). Further, quantum mechanical calculations of proton transfer in small, basic residue-containing peptides with well-solvated protons (the case for the proteins studied here, which have more basic sites than charges in every instance) yield ΔG‡ values consistent with ours (~70 kJ/mol for proton transfer to an amide oxygen).[240]

This suggests the intriguing possibility that our experiments measure the energy of proton transfer from a basic side chain to the peptide backbone, which is likely to be the rate-limiting step in gas-phase protein unfolding for many native-like protein ions. Moreover, the lower charge states tend to be associated with higher $\Delta H^\ddagger$ values, consistent with those relatively fewer protons being more tightly bound. Many previous reports have established and commented on the link between charge state and CIU/CID,[37,38,41,241] and this result provides quantitative support for the connection between the Mobile Proton model and CIU.

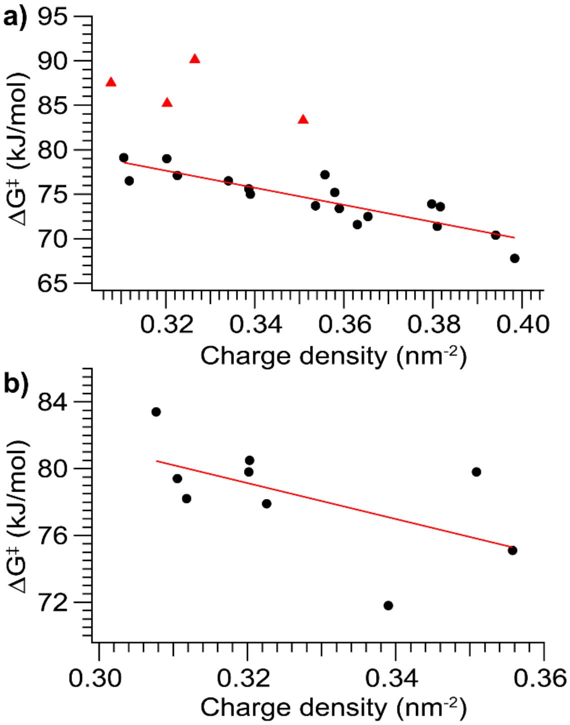

Figure 22. Plots of $\Delta G^\ddagger$ versus charge density (number of charges divided by CCS) for **(a)** positive and **(b)** negative ions. For positive ions the four species with anomalously high $\Delta G^\ddagger$ are also outliers here. There is a strong correlation ($R^2 = 0.77$) between $\Delta G^\ddagger$ and charge density for the species that fully unfold. For negative ions there is a weaker correlation between $\Delta G^\ddagger$ and charge density ($R^2 = 0.33$).

A weaker correlation between $\Delta G^\ddagger$ and charge density is observed for negatively-charged ions ($R^2 = 0.33$) (Figure 22b), for which fewer native charge states were produced by electrospray. The weaker correlation as compared to positively-charged protein ions may also arise due to differences in the number and identity of protonation/deprotonation sites between positive and negative polarities. Since the $\Delta G^\ddagger$ values for negative polarity cluster in the same region as those for positive polarity, the simple explanation is that similar mechanisms are operative in both polarities (i.e. proton transfer is the rate-limiting step). However, while in positive polarity charges can move to many moderately basic sites (such as amide groups) along the peptide backbone, in negative polarity charge mobilization requires donation of a proton to the charged site, limiting the number of groups that can participate. A more direct charge transfer process may be involved in gas-phase unfolding in negative polarity, such as neutralization of salt-bridge interactions leading to increased charge repulsion and unfolding. This mechanism could also be operative in positive polarity, thus preserving the possibility of a unified explanation of gas-phase unfolding for both polarities.

I also considered the effect of instrumental characteristics on the set of transitions that are observable and quantifiable using our instrument (see Appendix C for details). For small to very large proteins, the lower bound of the range of accessible energies is approximately 60 kJ/mol, while the upper bound lies close to 200 kJ/mol for a small protein such as ubiquitin (8.5 kDa) and decreases to ~80 kJ/mol for a very large protein such as GroEL (800 kDa) (Fig. C11). Enhanced control over ion temperature (initial and final) and reaction time via instrument modifications could allow relevant transitions occurring at lower or higher energies to be investigated.

Conclusions

A novel, rapid method for quantitatively determining activation energies for gas-phase protein unfolding and dissociation was introduced. Combining a previously-developed model for energy deposition in collisional activation with unimolecular rate theory enabled measurement of dissociation and unfolding thermodynamics. Values derived using this method agree well with those determined using BIRD. Although our method is more dependent on the veracity of constructed models than is BIRD, I expect that in many cases it will provide results rapidly with reasonable accuracy. Another advantage of this method is that ion internal energies upon activation can be practically sampled more finely than in typical BIRD experiments due to facile adjustment of collision cell voltages. Studies of gas-phase protein unfolding reveal that $\Delta G^{\ddagger}$ values for a given protein decrease with increasing charge state, while those across proteins fall within a narrow range; there is more variation with charge state than with protein identity for the range of native-like and charge-reduced ions probed here. The above results lead us to infer that the CIU transitions observed in these experiments result from proton transfer from a basic site to the peptide backbone. This inference is supported by the concurrence of our experimental $\Delta G^{\ddagger}$ values and those computed for proton transfer in small model peptides.

This work only considered the lowest-energy gas-phase unfolding transition resolvable with a Synapt G2-S*i*, which is from a compact, native-like structure to another relatively-compact structure. However, subsequent unfolding transitions and MD modeling of changes in CCS may provide additional insight into high-order protein structure and are the subject of future investigations. Also, while charge density and $\Delta G^{\ddagger}$ are found to be correlated, exploring the origins of deviations from the trend may reveal interesting protein-specific impacts on unfolding activation energy. Although the relationship between $\Delta G^{\ddagger}$ values determined here and solution-phase unfolding behavior remains a question for future exploration, the amount of unfolding observed in these gas-phase experiments is typically smaller than that observable with many condensed-phase techniques and thus has the potential to provide more detailed unfolding data than conventional techniques. Further experiments measuring $\Delta G^{\ddagger}$ for ligand dissociation and subsequent comparison to solution-phase binding constants will aid in establishing that link and could yield insights into important biological interactions including enzyme-inhibitor and protein-lipid systems.

One important class of protein-ligand systems is membrane protein-lipid interactions. Because membrane proteins can be ionized within membrane mimetics and subsequently analyzed in the gas phase, mass spectrometry is a promising candidate for studying membrane proteins. However, a recent report from our group predicted that significant non-specific binding between lipids and proteins is likely to occur.[242] In Chapter V, I investigate experimentally non-specific binding between lipid head groups and soluble proteins, and use the method introduced in this chapter to study the $\Delta G^{\ddagger}$ of such interactions.

CHAPTER V

EXTENT AND ENERGETICS OF NON-SPECIFIC BINDING BETWEEN LIPID HEAD GROUPS AND SOLUBLE PROTEINS

While the material included here is primarily my own work, Samantha O. Shepherd assisted with data collection and analysis, and Jesse W. Wilson and James S. Prell contributed to experimental design and interpretation. This work will form a portion of a manuscript to be submitted in the future, with the above named as co-authors.

Introduction

As native mass spectrometry (MS) has increased in prevalence, a wider range of systems has come under investigation.[10,243] Of particular interest are membrane proteins and their interactions with lipids. Although membrane proteins comprise a significant fraction of the proteome, their propensity to aggregate and precipitate when removed from membrane environments makes them extremely difficult to characterize using many techniques.[244] However, membrane proteins can be solubilized through interaction with a local environment mimicking that of the lipid membrane, such as a detergent micelle[245,246] or lipid Nanodisc.[247-249] Native MS utilizes the ability of electrospray ionization (ESI) to transfer membrane proteins embedded within a membrane-like environment to the gas phase to probe the native-like structure, stoichiometry, and interactions of membrane proteins.[243,250] Several seminal papers from the Robinson group have demonstrated the power and potential of this approach.[251-253]

Phospholipids, which make up the majority of biological membranes, likely play roles beyond that of simply stabilizing membrane proteins. In many cases, lipid-protein interactions may affect membrane protein function.[254,255] Preferential binding to a particular lipid or lipids can affect such properties as localization and oligomerization.[256] Therefore, knowledge of these lipid-protein interactions is important for understanding membrane function and developing therapeutics targeting membrane proteins.[257] The Robinson and Laganowsky groups have led the way toward addressing these questions using native MS, publishing studies investigating structural stabilization due to lipid binding and reporting binding constants and allosteric effects.[224,258,259]

However, as for all native MS experiments, there may not be an exact correspondence between measured gas-phase results and solution-phase parameters.[260] Importantly in this case, there is the possibility of non-specific binding between lipids and proteins. Non-specific binding is an artifact of the ESI process, caused by two species present in the same droplet that associate as the solvent evaporates.[261,262] In many of the lipid binding experiments conducted to date this is possible, based on the concentrations of lipid and protein used. Depending on the strength of the interaction in the gas phase, such interactions may be transient or long-lasting, with ionic interactions typically proving robust. One common example of this is adduction of sodium ions, which is almost ubiquitously present in solution. Protein ions often suffer from excessive sodium adduction, leading to decreased peak resolution.[263] Polymers lacking strongly polar groups may be entirely charged via sodium adduction,[81] enabling analysis by MS.

The chemistry of lipid head groups defines their potential propensity to form non-specific bonds with proteins, as lipid tails have no ionizable groups. Head groups of many common lipids contain acidic groups (such as phosphate) and/or basic groups (such as amines) and can thus form shared-proton bonds with basic residues on the protein surface.[264] The strength of such interactions is dependent on the gas-phase basicity (GB) values of both participants in the bond, with closer GB values producing a stronger bond.[264] A recent report from my colleagues in the Prell group demonstrated that lipids with phosphoserine and phosphoethanolamine head groups had GBs very close to those of lysine, the second-most basic amino acid and a common location of charge for protein ions, suggesting that these lipids have the potential to form strong shared-proton bonds.[242] Phosphoglycerol lipids had GBs well below that of lysine, suggesting that they would form weaker bonds.[242] Phosphocholine lipids had GBs above that of arginine, the most basic amino acid, suggesting that they would also form weaker shared proton bonds and that they would tend to strip charge from protein ions.[242] To date, these predicted interactions have not been confirmed experimentally.

In Chapter IV I discussed a method I recently introduced to determine activation energies for collision-induced dissociation (CID) of non-covalent protein complexes, including protein-ligand complexes. This method enables the gas-phase energetics of non-specific binding to be probed. The degree to which binding strength reflects solution- or gas-phase characteristics is highly relevant to studying protein-lipid interactions with native MS. If gas-phase parameters dominate, then extra care will be necessary in both designing and interpreting the results of experiments. In addition, probing binding energetics of a suite of molecules to multiple proteins will serve to further characterize the performance of the method I introduced in Chapter IV.

In order to probe non-specific binding between lipids and proteins, I will use soluble proteins and lipid head groups, which are soluble in aqueous solution. This will enable facile characterization of binding without the need for detergent micelles or lipid Nanodiscs, and, as head groups will be responsible for the vast majority of non-specific interactions, will provide a reliable readout of the typical extent of non-specific adduction. In this chapter I report non-specific binding of several lipid head groups to multiple soluble proteins. The extent of binding follows the predicted trend, with serine- and ethanolamine-containing head groups binding extensively, while choline-containing head groups bind less readily and tend to strip charge from the protein. The energetics of binding also follow the predicted trend, with serine- and ethanolamine-containing head groups binding strongly, while choline-containing head groups bind weakly. These results demonstrate the importance of considering GB and non-specific binding and are a step towards a framework for interpreting membrane protein-lipid binding native MS experiments quantitatively.

Methods

Sample preparation. Glycerophosphorylcholine, phosphorylcholine, phosphorylethanolamine, glycerol 1-phosphate, phosphoserine, ubiquitin, and lysozyme were purchased from Sigma Aldrich. Lyophilized proteins were reconstituted in ultrapure 18 MΩ water and buffer-exchanged into 200 mM ammonium acetate pH 7-7.5. Lipid head groups were dissolved in 200 mM ammonium acetate pH 7-7.5. Protein and lipid head group solutions were combined such that the final concentrations of protein and head group were 10 μM and 100 μM, respectively.

Native IM-MS and CID. All mass spectra were acquired in "Sensitivity" mode using a Synapt G2-S*i* (Waters Corp.) with a nanoelectrospray source. Nanoelectrospray emitters were pulled from 0.78 mm i.d. borosilicate capillaries to a final i.d. of ~1 μM using a Flaming-Brown P-97 micropipette puller (Sutter Instruments). Emitters were loaded with 3-5 μL of sample and 0.7-1.1 kV applied to a platinum wire in electrical contact with the solution to initiate electrospray. The source was held at ambient temperature, and nitrogen, helium, and argon gas flow rates were 50, 100, and 5 mL/min, respectively. A traveling wave velocity of 500 m/s and height of 20 V were used for all experiments. For collision induced dissociation (CID) experiments, the singly-adducted state was isolated for a given charge state using the quadrupole with the LM resolution set to 12. Dissociation was performed by increasing the Trap CE in 1 V increments, beginning at the lower threshold for dissociation and continuing until the precursor was fully dissociated or significant covalent fragmentation was observed.

Data analysis. Data was analyzed in a similar manner to that described in Chapter IV. Briefly, arrival time distributions for precursor and product ions were extracted using TwimExtract[238] and integrated in Igor Pro (WaveMetrics). The relative abundance of precursor at each Trap CE was determined (for ions that exhibited dissociation due to the isolation, the precursor relative abundance was normalized to have a maximum value of 1), as was the effective temperature. These values were used to compute the left-hand side of Equation 14, which was plotted against the reciprocal of temperature multiplied by the Boltzmann constant. The slope and intercept were then used to determine $\Delta H^\ddagger$ and $\Delta S^\ddagger$, respectively, using Equation 14. $\Delta G^\ddagger$ was determined from $\Delta H^\ddagger$, $\Delta S^\ddagger$, and the average effective temperature over the range of data included in the fit.

Results and Discussion

Several lipid head groups representing the most common phospholipids were studied. Structure of phosphorylethanolamine (PE), glycerol 1-phosphate (PG), phosphoserine (PS), phosphorylcholine (PC), and glycerophosphorylcholine (GPC) are shown in Figure D1. GPC was studied in addition to PC since PC comes as a calcium salt; calcium adduction decreases spectral quality and complicates analysis. Ubiquitin (Ubq, 8.5 kDa) and lysozyme (LZ, 14 kDa) were used as model soluble proteins. Native mass spectra of each protein with no head group present were acquired and are shown in Figure D2. The most abundant charge state was chosen for subsequent CID experiments; 5+ for Ubq and 7+ for LZ. Each lipid head group was added to both proteins in a 10:1 molar ratio, the singly-adducted state isolated, and gradually dissociated using CID.

Mass spectra of lipid head group binding. For Ubq, spectra for GPC and PS binding are shown in Figure 23, and those for PC, PE, and PG binding are collected in Appendix D (Figure D3). All the head groups bind to Ubq. GPC and PC display the lowest extent of binding, with up to two bound to Ubq^{5+} (Figure 23a and D3a, respectively), while PS binds the most extensively, up to five on Ubq^{5+} (Figure 23d), and PE and PG fall between the two extremes, with up four bound to Ubq^{5+} (Figure D3d,g). Interestingly, GPC shifts the charge state distribution slightly to lower values, increasing the relative abundance of Ubq^{4+}.

For LZ, spectra for all head groups are shown in Figure D4. Overall, the data follow a similar trend to that for Ubq. Similarly, all head groups bind to LZ. In this case, PC binds least readily, with up to three bound to LZ^{7+} (Figure D4d), GPC, PE, and PE all bind to a similar extent, with up to 4 bound to LZ^{7+} (Figure D4a,g,j), and PS binds most extensively, with up to 8 on LZ^{7+} (Figure D4m). Again, GPC has a slight charge-reducing effect, in this case increasing the relative abundance of LZ^{6+}. Taken together, the data suggest that PS binds most readily, and PC and GPC bind least readily. In order to determine the strength of the interactions, however, it is necessary to perform CID.

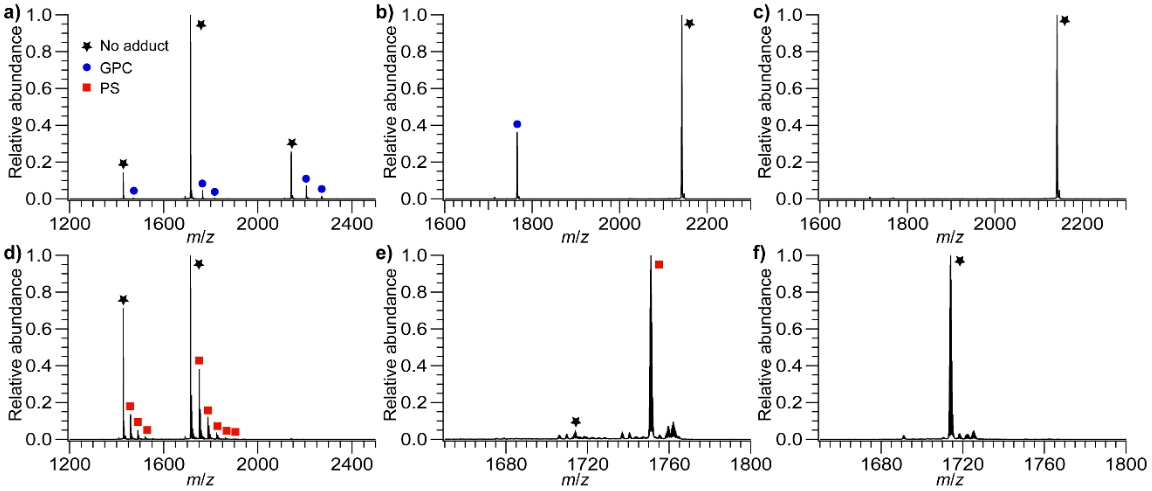

Figure 23. Mass spectra of GPC and PS bound to Ubq. **(a)** Ubq with GPC bound **(b)** isolated Ubq^{5+} with GPC bound at low activation **(c)** isolated Ubq^{5+} with GPC bound at high activation **(d)** Ubq with PS bound **(e)** isolated Ubq^{5+} with PS bound at low activation **(f)** isolated Ubq^{5+} with PS bound at high activation.

CID of lipid head groups. For each protein and head group combination, CID was performed by scanning the collision voltage in 1 V increments from a minimally-activating voltage to one sufficient to cause complete dissociation but not significant fragmentation. Isolated mass spectra of the singly-adducted state are shown in the middle column of Figures 23, D3, and D4. In the majority of cases the singly-adducted peak is not the only peak present in the isolated spectrum. The presence of protein with no head group adducts in these spectra is due to a combination of dissociation of the head group due to activation during the isolation and imperfect mass selection due to the intensity of the non-adducted and singly-adducted peaks. In appendix C (Figure C5) the isolation is shown to have a small heating effect for myoglobin (17 kDa) ions. Ubq and LZ may experience a somewhat greater degree of activation during the isolation, but it will likely still have only a small effect on the final energies determined. However, in order to account for the presence of protein with no adducts (which is also the product of CID), the relative abundances were normalized to the maximum of the singly-adducted state prior to further analysis. The right-hand column of Figures 23, D3, and D4 shows isolated mass spectra at high activation, indicating that there is a single CID product in all cases. While PE, PG, and PS all dissociate as neutral species, GPC and PC dissociate with a positive charge. Note that while some of the non-adducted protein of the same charge state is present due to imperfect isolation, it stays constant in abundance while the abundance of the non-adducted protein with one fewer charge increases over the course of the CID experiment. This result agrees with that predicted by comparison of GB values. PC (and GPC) have values above that of arginine and thus abstract the proton when dissociating, while the other head groups have GBs below that of arginine.

The relative abundance of the singly-adducted state at each collision voltage for each protein and head group combination are shown in Figure 24. For both Ubq and LZ, the same ordering is observed. GPC binds most weakly, followed closely by PC, then PE, followed closely by PG, and finally PS. The difference between GPC and PC is likely due to the additional free phosphate oxygen in PC compared to GPC (Figure D1), which could participate in a multidentate interaction and provide additional stabilization. As expected, PS binds most strongly, as its GB is very close to that of lysine and histidine, common protonation sites. PE which has a GB between those of arginine and lysine, forms a moderately strong interaction, also in agreement with the prediction. However, PG, which is significantly less basic than all common protonation sites and thus is not expected to form a strong interaction, actually forms a stronger interaction than PE. The PG spectra have more sodium adduction than the PE spectra, and increased salt adduction can lead to increases in measured CID energies. However, at most 50% of the singly-adducted population is sodiated in the low-activation isolated spectra, and this profile is largely constant throughout the experiment, indicating that any effect of increased sodium adduction is likely small. Since these interactions form in the latter stages of the ESI process and may be concurrent with charging, it is possible that the presence of a significant amount of PG causes alternative charge configurations to become favored. PG could form a relatively stable shared proton interaction with an amino acid residue such as proline or tryptophan during the charging process, and the resulting configuration could be more stable than one with protonation at only arginine and lysine residues. Other than PG, however, the interaction strengths agree with those predicted based on GBs.

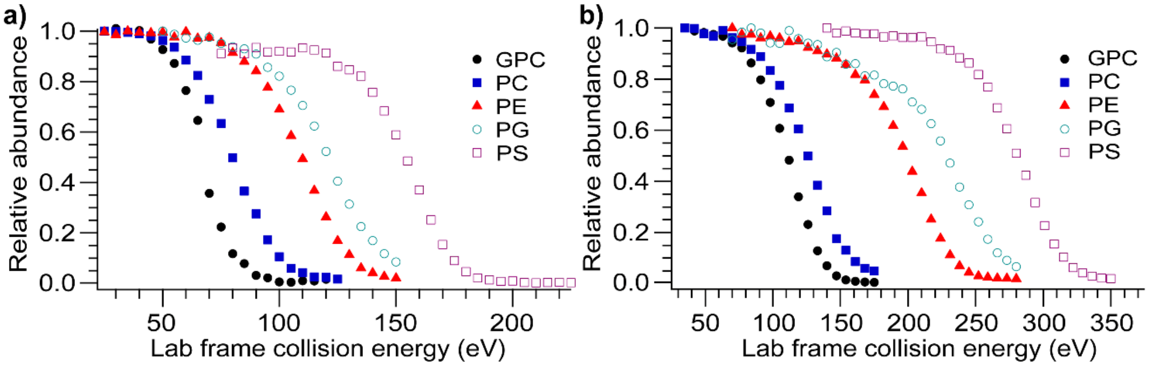

Figure 24. Breakdown curves for dissociation of lipid head groups from **(a)** ubiquitin, 5+ **(b)** lysozyme, 7+. For both proteins the same trend in binding strength is observed, namely PS > PG > PE > PC > GPC.

Activation energies for head group CID. Activation energies were determined using the method introduced in Chapter IV for each protein and head group combination. $\Delta G^{\ddagger}$ values are shown in Table 3, and $\Delta H^{\ddagger}$ and $\Delta S^{\ddagger}$ values are shown in Table D1. $\Delta G^{\ddagger}$

values fall between 65 and 81 kJ/mol and follow the same trend as the midpoints of the breakdown curves, i.e. PS > PG > PE > PC > GPC. Comparing $\Delta G^{\ddagger}$ values for the same head group but different proteins reveals a strong correlation. Observed discrepancies are below 7%, much less than the variation across head groups for a given protein, suggesting that the interaction between the head group and protein depends mainly on the local environment and that my method captures the particularities of the interaction. CID of GPC and PC produce $\Delta H^{\ddagger}$ values that are among the highest (Table D1), likely due to the presence of a Coulombic barrier. They also have the highest $\Delta S^{\ddagger}$ values, which may be indicative of rearrangement to an ensemble of charge configurations following abstraction of charge by GPC/PC. The activation energies measured here also lie close to those reported in Chapter IV for protein unfolding and in the literature for proton transfer between basic groups within peptides. As the lipid head groups studied here have similar GBs to those of several basic amino acid residues, the concordance between the measured values provides further confirmation that the barrier to proton transfer between groups approximately as basic as many amino acids is ~70 kJ/mol. The activation energies agree with the energy trend obtained from breakdown curve data and in addition uncover further, more subtle, details of the CID process.

Table 3. Activation free energies for lipid head group CID.

Head group	Ubiquitin, 5+ $\Delta G^{\ddagger}$ (kJ/mol)	Lysozyme, 7+ $\Delta G^{\ddagger}$ (kJ/mol)
GPC	65.8±14.6	67.2±4.6
PC	68.9±8.0	67.9±4.8
PE	71.9±8.1	73.7±4.6
PG	72.5±4.9	75.5±5.0
PS	75.7±8.5	80.9±9.5

Conclusions

The non-specific binding of several lipid head groups to soluble proteins was investigated with native MS and CID. Non-specific binding of all head groups to both proteins studied, Ubq and LZ, was observed. The strength of binding was probed using CID, revealing that PS binds most strongly, followed by PG, PE, PC, and GPC. This trend is can largely be explained by similarities in GB values between the head groups and amino acid residues likely to be protonated. For example, PS has a GB very close to that of lysine and thus will form a strong interaction, while PC and GPC have GBs above the most basic residue and thus form weaker interactions and dissociate with a positive charge, rather than as a neutral species. However, PG, which is not expected to form a strong interaction based on its relatively low GB, in fact forms the second strongest interaction. This may be due to formation of shared proton bonds within the shrinking ESI droplet, leading to a stronger interaction than would otherwise occur. $\Delta G^{\ddagger}$ values for a given head group are similar for Ubq and LZ, suggesting that the barrier for dissociation is largely intrinsic to the head group-protein interaction.

Since the chemistry of the lipid head group significantly affects non-specific binding behavior, results of membrane protein-lipid binding experiments should be interpreted with caution. In particular, PS lipids are likely to bind more strongly in the gas phase than expected based on solution-phase information, while PC lipids dissociate readily and may be stripped during ejection of a membrane protein from a detergent micelle. Future experiments characterizing the non-specific binding of lipid head groups to larger soluble proteins, including soluble forms of membrane proteins, will aid in characterizing the extent of non-specific adduction that can be expected for typical membrane proteins, which are larger than the proteins studied in this chapter. In addition, the energetics of binding between lipids and several model membrane proteins will be investigated, and by fully characterizing the non-specific adduction of lipids, the method introduced in Chapter IV and applied in this chapter could be used to probe the energetics of membrane protein-lipid binding to elucidate specific interactions.

OUTLOOK

This dissertation presents several novel insights and methods that expand the frontiers of native mass spectrometry by bringing quantitative analysis to systems previously studied qualitatively. Native mass spectrometry had emerged as a valuable tool for interrogating proteins and non-covalent complexes and proved useful in studying protein structure and covalent and non-covalent interactions. While the compact, folded structures of native-like protein ions had been extensively investigated, those of partially or fully unfolded protein ions had received less scrutiny. Furthermore, while numerous techniques to probe the energetics of small systems such as peptides had been developed, important processes such as gas-phase protein unfolding, as well as complex dissociation into structures reflecting the overall topology, had not yet been studied quantitatively. Although qualitative analysis can be very useful, it does not extract all possible information from the available data. Therefore, the moment appeared ripe for the development and application of more quantitative tools to gas-phase protein structure and structural transitions. The initial fruits of that effort are relayed in this dissertation.

The quantitative information described here was gleaned through a combination of experiments and simulations working in harmony along with global analysis of proteins across sizes. These approaches provided insight into mechanistic, energetic, and structural details of gas-phase protein behavior. In Chapter II, scaling behavior was used to study the highly unfolded structures of protein ions created by supercharging ESI. Mechanistic details of supercharging ESI were also uncovered, contributing to an ongoing discussion in the field. Beyond structures originating from ESI, the information contained within structures generated in the gas phase has long been of interest. Thus, attention was turned to gas-phase structural changes and several methods of producing them. In Chapter III, the energy deposition efficiencies of two such methods, CIU and SIU, were investigated. Modeling the activation process enabled absolute calibration of both energy scales. The dependence of energy deposition efficiency on structure was also probed. The model for collisional activation introduced in Chapter III led directly to the novel quantitative method developed in Chapter IV. This method is faster than other gas-phase quantitation approaches, and, crucially, can be applied to study protein unfolding. The method was validated and applied to investigate common features of gas-phase protein unfolding and reveal intriguing mechanistic insights. Protein-lipid interactions, which are often difficult to study, have been investigated using native MS. However, the potential for spurious non-specific interactions exists. Chapter V studied non-specific binding between lipid head groups and several soluble proteins and demonstrates the role of gas-phase basicity in binding strength, sounding a note of caution for native MS studies of lipid binding. Future directions include further application of the quantitative methods developed here to study lipid binding, as well as investigation of other important protein-protein and protein-ligand interactions such as enzyme-inhibitor complexes. In addition, it is likely that much of the structural information contained within CCS distributions remains unexploited. Our group and others developed approaches to begin extracting this information for structures generated during ESI. Extending these approaches to probe structures arising due to CIU or SID experiments and combining them with the quantitative tools introduced in this dissertation will further increase the usefulness of IM-MS for the study of proteins and complexes.

APPENDIX A

SUPPLEMENTAL INFORMATION FOR CHAPTER II: EXTENDED PROTEIN IONS ARE FORMED BY THE CHAIN EJECTION MODEL IN CHEMICAL SUPERCHARGING ELECTROSPRAY IONIZATION

Table A1. Experimentally-observed charge states of native and supercharged head-to-tail linked poly-ubiquitins (Ubq_{1-11}). z_{ma} is the most abundant charge state, z_{avg} is the average charge state, and z_{max} is the highest-observed charge state with a signal-to-noise of at least 2:1.

Protein	Native z_{ma}	Native z_{avg}	Supercharged z_{ma}	Supercharged z_{max}
Ubq_1	5+	4.64	12+	14+
Ubq_2	7+	7.26	19+	26+
Ubq_3	9+	8.52	32+	37+
Ubq_4	10+	9.92	44+	50+
Ubq_5	12+	11.71	51+	60+
Ubq_6	13+	12.87	63+	72+
Ubq_7	14+	13.92	74+	81+
Ubq_8	15+	14.90	84+	90+
Ubq_9	16+	16.24	90+	97+
Ubq_{10}	17+	17.28	95+	105+
Ubq_{11}	17+	17.36	108+	114+

Table A2. Amino acid composition of proteins studied. Letters in parentheses are one-letter abbreviations of amino acids.

Amino acid type	Ubq	Myoglobin	LF_N	PA_{63}	Carbonic anhydrase	ADH
Non-polar (AGILPV)	40.0%	43.8%	34.8%	35.7%	41.5%	49.9%
Aromatic (FWY)	4.0%	7.2%	8.2%	7.5%	9.2%	7.8%
Polar (NQCMST)	25.3%	14.4%	18.7%	29.8%	24.2%	19.9%
Acidic (DE)	16.0%	20.9%	18.0%	14.4%	14.2%	12.1%
Basic (RKH)	14.7%	13.7%	20.2%	12.7%	10.8%	10.4%

Derivation of analytical maximum charge state scaling law for highly-extended protein ions

I derive a simple analytical model for the scaling behavior of quasi-linear protein ions by treating them as line segments. For a set of *z* point charges in vacuum spaced uniformly along a line segment of length L, the apparent gas-phase basicity (resp., proton affinity), $\mathrm{GB}^{\mathrm{app}}$ (resp., $\mathrm{PA}^{\mathrm{app}}$) of the charge configuration, is equal to the sum of the intrinsic gas-phase basicities, $\mathrm{GB}^{\mathrm{int}}$, (resp., $\mathrm{PA}^{\mathrm{int}}$) of the charged sites minus

$$U_{tot} = \sum_{i<j}^{z} \frac{ke^2}{\varepsilon_r r_{ij}} = \sum_{i<j}^{z-1} \frac{ke^2}{\frac{(j-i)\varepsilon_r L}{z-1}} = \frac{ke^2(z-1)}{\varepsilon_r L} \sum_{i<j}^{z-1} \frac{1}{j-i} \tag{A1}$$

the total electrostatic self-energy of the charge configuration, where r_{ij} are the pair-wise distances between charges, *k* is Coulomb's constant, ε_r is the relative dielectric permittivity, and *e* is the fundamental charge. U_{tot} simplifies to

$$U_{tot} = \frac{ke^2(z-1)}{\varepsilon_r L} \sum_{(j-i)=a=1}^{z-1} \frac{z-a}{a} = \frac{ke^2(z-1)}{\varepsilon_r L} \left(\left(z \sum_{a=1}^{z-1} \frac{1}{a}\right) - (z-1) \right) \tag{A2}$$

which can be rewritten

$$U_{tot} = \frac{ke^2 z(z-1)}{\varepsilon_r L} \sum_{a=1}^{z-1} \frac{1}{a} - \frac{ke^2(z-1)^2}{\varepsilon_r L} \tag{A3}$$

For large *z*, this can be approximated

$$U_{tot} = \frac{ke^2 z(z-1)}{\varepsilon_r L} (\ln(z-1) + \gamma) - \frac{ke^2(z-1)^2}{\varepsilon_r L} \tag{A4}$$

where γ = 0.577 . . . is the Euler-Mascheroni constant. If a charge is removed and the remaining charges are allowed to spread out uniformly again, the resulting energy difference is

$$\begin{aligned} U_{tot}(z) - U_{tot}(z-1) = {} & \frac{ke^2 z(z-1)}{\varepsilon_r L} (\ln(z-1) + \gamma) - \frac{ke^2(z-1)^2}{\varepsilon_r L} \\ & - \frac{ke^2(z-1)(z-2)}{\varepsilon_r L} (\ln(z-2) + \gamma) + \frac{ke^2(z-2)^2}{\varepsilon_r L} \end{aligned} \tag{A5}$$

For large *z*, this tends toward

$$U_{tot}(z) - U_{tot}(z-1) = \frac{3ke^2(z-1)}{\varepsilon_r L}\ln(z-1) \tag{A6}$$

Assuming, for large *z*, that the total of the intrinsic gas basicities (resp., PA^{int}) of the protonated sites is $z \times GB_{avg}^{int}$ (resp., $z \times PA_{avg}^{int}$) and that the protein ion is in quasi-equilibrium with water vapor, one obtains

$$GB^{app}(z) - GB^{app}(z-1) = GB_{avg}^{int} - GB(H_2O) = U_{tot}(z) - U_{tot}(z-1) \tag{A7}$$

(resp., the analogous equation with GB's replaced by PA's).

Since GB_{avg}^{int} (resp., PA_{avg}^{int}) is independent of *z*, one finally obtains the approximation

$$\frac{3ke^2(z-1)\ln(z-1)}{\varepsilon_r L} \propto constant \tag{A8}$$

so that

$$3ke^2(z-1)\ln(z-1) \propto L \propto mass \tag{A9}$$

Table A3. Measured reaction rates and apparent gas-phase basicities (GB^{app}) for [Ubq$_1$, (z+1)H]$^{(z+1)+}$ and [Ubq$_3$, (z+1)H]$^{(z+1)+}$. Literature values for GB of reference bases are taken from Hunter and Lias.[265]

Base (GB, kJ/mol)	**Reaction rates (x10^{-11} cm^3 /mol•s)**			
Propane (607.5)			< 1.0	
Water (666.1)	< 1.0		4.8	
Methanol (724.5)	7.1			
Hexanone (811.3)				< 1.0
3-fluoropyridine (872.8)				3.5
Pyridine (902.5)		< 1.0		
Tri-n-propylamine (946.4)		7.8		
	Ubq$_1$	**Ubq$_1$**	**Ubq$_3$**	**Ubq$_3$**
Charge state (z)	13+	4+	36+	8+
GB^{app} (kJ/mol)	695.4	924.7	636.8	887.8

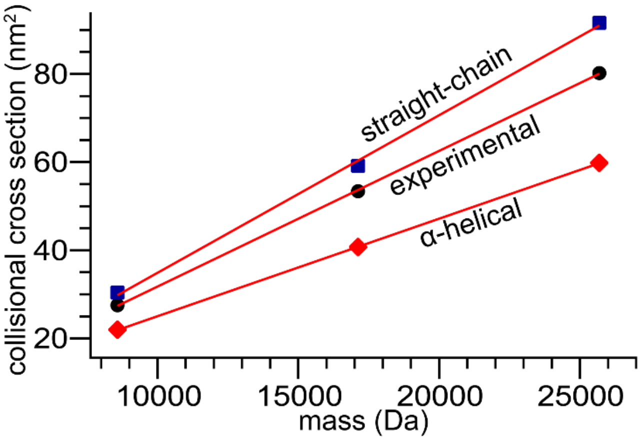

Figure A1. Collisional cross sections for Ubq$_{1\text{-}3}$ either measured using traveling-wave ion mobility (black circles) or calculated using Collidoscope for straight-chain (blue squares) or α-helical (red diamonds) structures. While all three sets of data follow linear trends, CCS increases more quickly with mass for the straight-chain structures as compared to the α-helical structures. The experimental CCSs are greater than those for the α-helical structures but lower than those for the straight-chain structures, indicating that the experimental structures are highly extended but not completely straight chains.

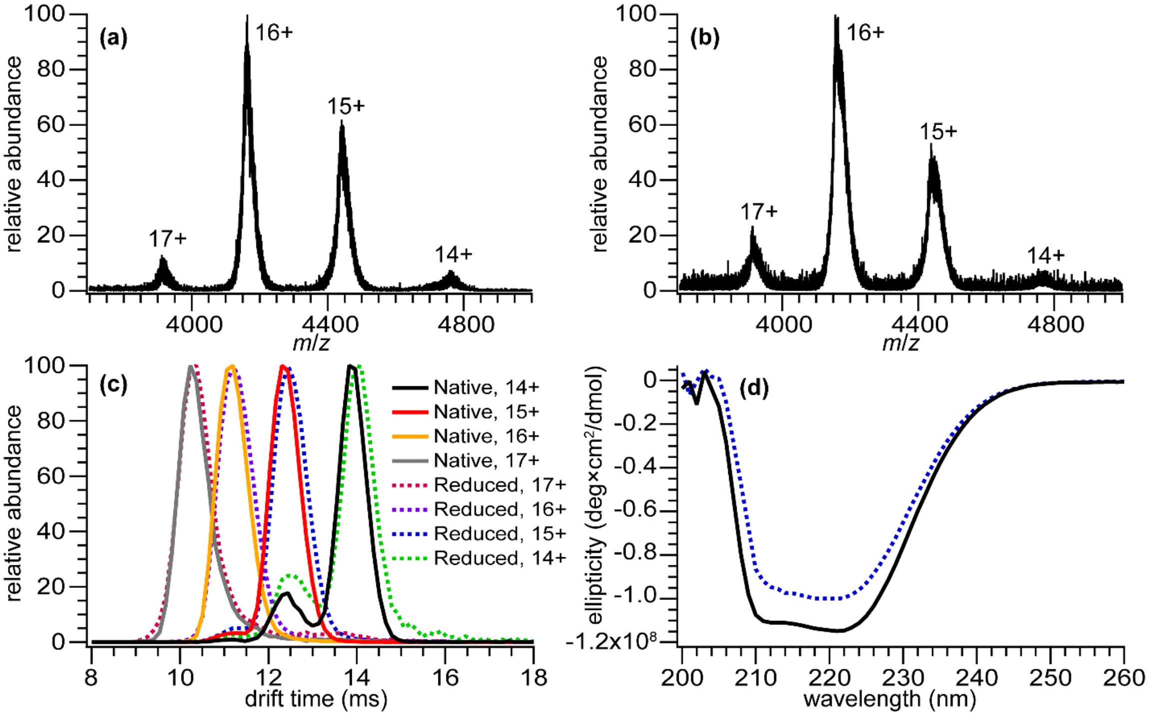

Figure A2. (a) Mass spectrum of natively folded BSA has a low and narrow charge state distribution. **(b)** Mass spectrum of refolded reduced BSA has a nearly identical charge state distribution. **(c)** Arrival time distributions of the 14+ to 17+ charge states of reduced and un-reduced BSA displaying a 1% increase in the peak location for the reduced protein, indicating nearly identical structures. **(d)** Circular dichroism spectra of un-reduced (solid black line) and reduced (dashed blue line) BSA in native ESI buffer. Similar peak shape indicates highly similar secondary structure content.

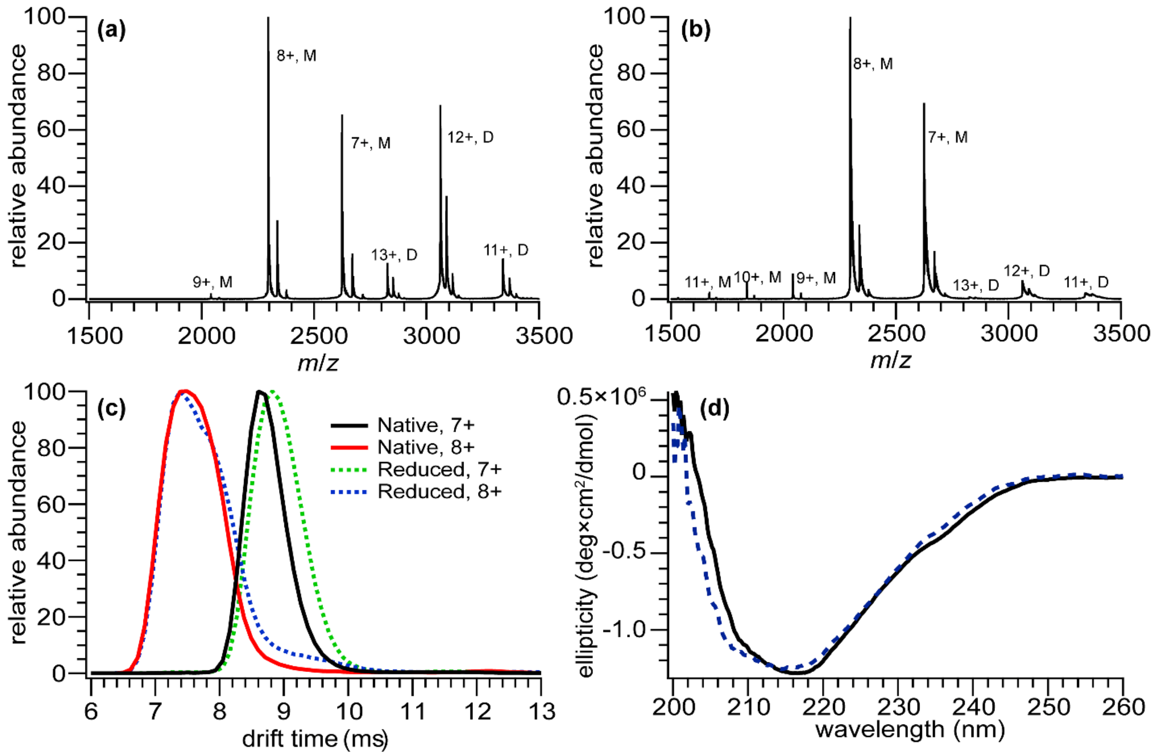

Figure A3. (a) Mass spectrum of natively folded β-lactoglobulin displaying populations of monomers (M) and dimers (D) with low and narrow charge state distributions. **(b)** Mass spectrum of refolded reduced β-lactoglobulin, with a smaller population of dimers (D) and an additional small amount of higher monomer (M) charge states. **(c)** Arrival time distributions of reduced 7+ (dashed green line) and 8+ (dashed blue line) and un-reduced 7+ (solid black line) and 8+ (solid red line) β-lactoglobulin monomers. There is virtually no change in the peak of the distribution for the 8+ charge state and reduction leads to a 2% increase in arrival time for the 7+ charge state. **(d)** CD spectra of reduced (- - -) and un-reduced (——) β-lactoglobulin.

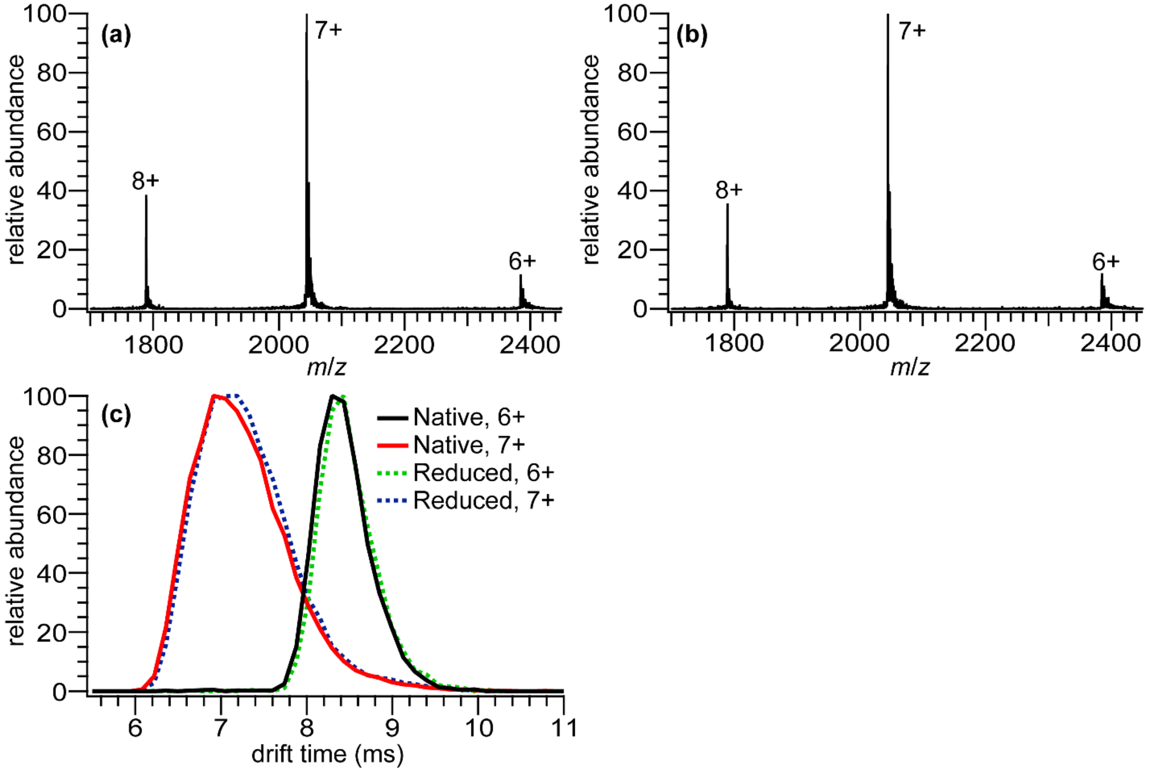

Figure A4. (a) Mass spectrum of natively folded lysozyme displaying low and narrow charge state distribution. **(b)** Mass spectrum of refolded reduced lysozyme with a virtually identical charge state distribution. **(c)** Arrival time distributions of 6+ and 7+ charge states of native and reduced lysozyme in native electrospray buffer showing a negligible, 1% increase in the peak position for the reduced protein as compared to the native protein.

Table A4. Experimental drift times for un-reduced and reduced BSA, β-lactoglobulin, and lysozyme in native conditions.

	BSA		
z	Un-reduced (ms)	Reduced (ms)	Difference (%)
14+	13.9	14.0	1
15+	12.4	12.5	1
16+	11.2	11.3	1
17+	10.3	10.3	1
	β-lactoglobulin		
7+	8.7	8.9	2
8+	7.6	7.6	1
	Lysozyme		
6+	8.4	8.4	1
7+	7.1	7.2	1

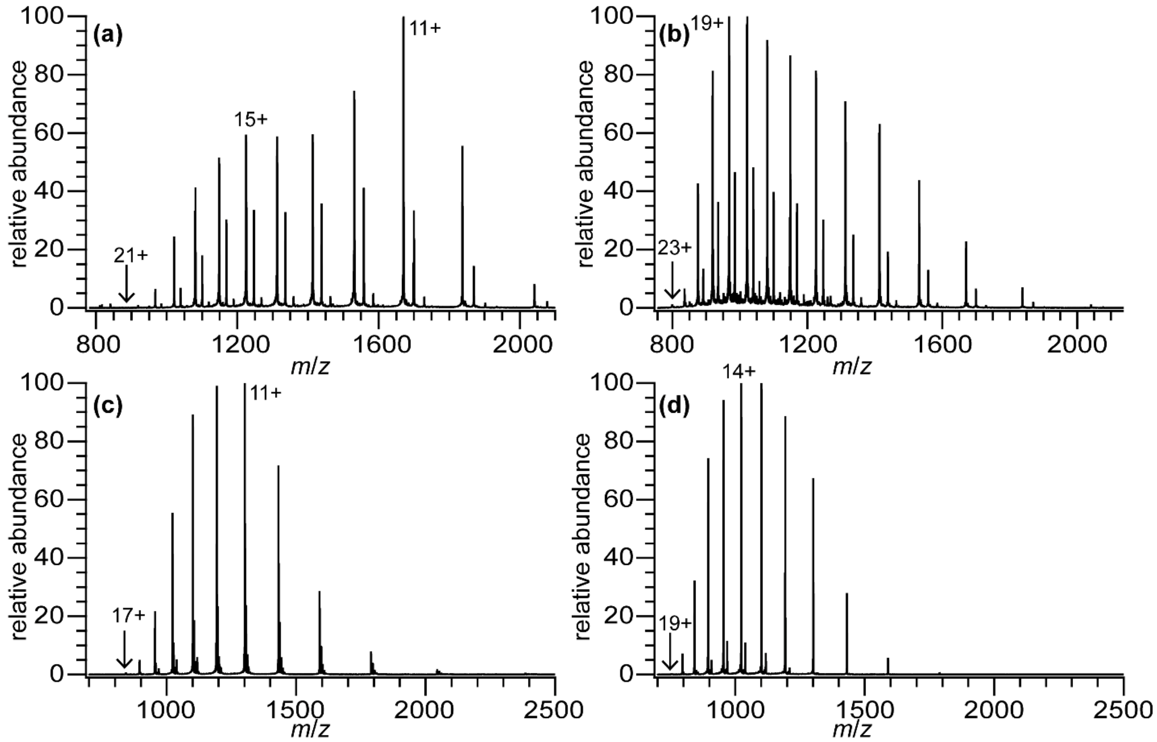

Figure A5. Mass spectra in supercharging conditions. **(a)** Un-reduced β-lactoglobulin has a bimodal distribution with most abundant charge states of 11+ and 15+ and a highest observed charge state of 21+. **(b)** Reduced β-lactoglobulin has a most abundant charge state of 19+ and a highest observed charge state of 23+. Note that the small peaks slightly higher in mass than the main charge state series in (a) and (b) are a second isoform of β-lactoglobulin. **(c)** Un-reduced lysozyme has a most abundant charge state of 11+ and a highest observed charge state of 17+. **(d)** Reduced lysozyme has a most abundant charge state of 14+ and a highest observed charge state of 19+.

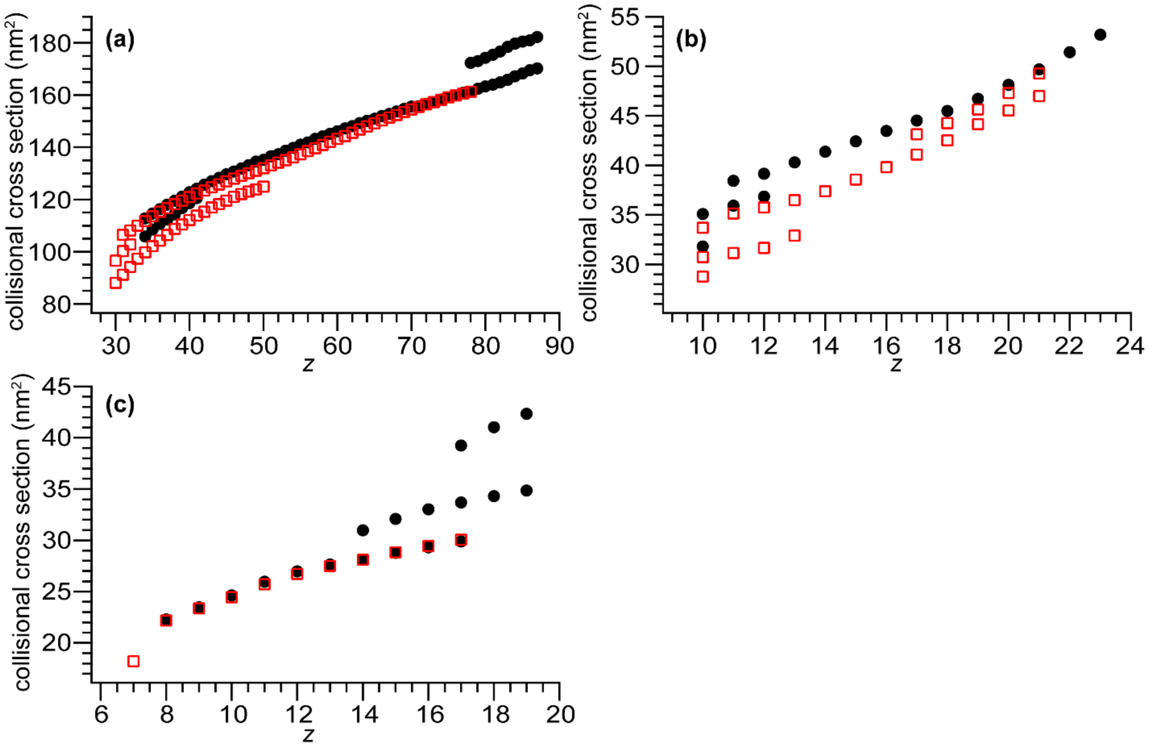

Figure A6. Plots of ion collisional cross section, measured in N_2 buffer gas, versus charge state for reduced (filled black circles) and un-reduced (open red squares) **(a)** BSA, **(b)** β-lactoglobulin, and **(c)** lysozyme.

APPENDIX B

SUPPLEMENTAL INFORMATION FOR CHAPTER III: EXPERIMENTAL AND THEORETICAL INVESTIGATION OF OVERALL ENERGY DEPOSITION IN SURFACE-INDUCED UNFOLDING OF PROTEIN IONS

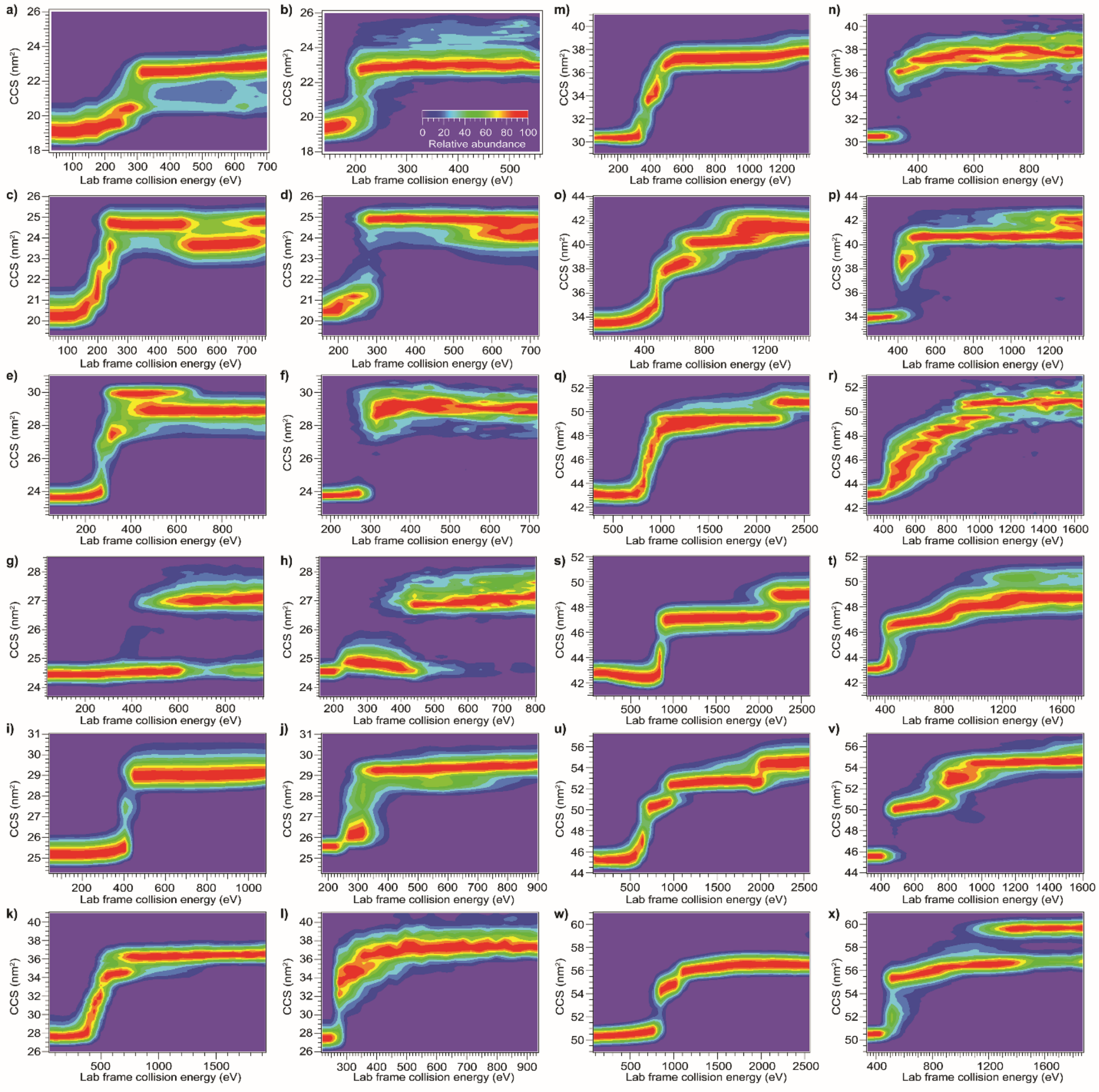

Figure B1. CIU and SIU plots, respectively, for **(a)** and **(b)** myoglobin, 7+ **(c)** and **(d)** β-lactoglobulin, 8+ **(e)** and **(f)** concanavalin A, 8+ **(g)** and **(h)** carbonic anhydrase 8+ **(i)** and **(j)** carbonic anhydrase 9+ **(k)** and **(l)** LF$_{\mathrm{N}}$, 11+ **(m)** and **(n)** alcohol dehydrogenase, 11+ **(o)** and **(p)** albumin, 12+ **(q)** and **(r)** PA$_{63}$, 15+ **(s)** and **(t)** bovine serum albumin, 14+ **(u)** and **(v)** bovine serum albumin, 16+ **(w)** and **(x)** transferrin, 17+.

Monte Carlo modeling of CIU in a Synapt G2-S*i*

The initial kinetic energy of the ion was calculated as $z \times V$, where z is the charge on the ion and V the "Trap Collision Energy", the voltage difference between the entrance electrode of the Trap and the exit electrode of the quadrupole. V was varied from 10 V to 200 V in steps of 5V for each protein. The traveling wave velocity in the simulations was 300 m/s, the wave height 2 V, and the wavelength 1.21 cm. The length of the collision cell in our modified instrument is 9 cm. The time step for each computation was

$$t_s = \frac{1}{20}\frac{mfp}{\sqrt{\frac{2 \times z \times 200}{m_i}}} \tag{B1}$$

or 1/20th of the mean time between collisions for the maximum initial kinetic energy, where *mfp* is the mean free path and m_i is the mass of the ion. While the distance traveled was less than the length of the collision cell, for each time step the total distance traveled was computed as the velocity of the ion multiplied by the time step and the distance in the forward direction computed as the velocity in the forward direction multiplied by the time step. To determine if a collision occurred during the time step, a Monte Carlo sampling procedure was used. A random number between 0 and 1 was chosen, if it was smaller than the collision probability, calculated as $1 - e^{-d_{ts}/mfp}$, where d_{ts} is the total distance traveled during that time step, then a collision occurred. If a collision occurred, the distance traveled before the collision was determined as

$$d_c = -mfp \ln\left(r\left(1 - e^{-\frac{d_{ts}}{mfp}}\right) + e^{\frac{-d_{ts}}{mfp}}\right) \tag{B2}$$

where r is the random number used to determine that a collision occurred. The forward distance before the collision was

$$d_{c,z} = d_c \frac{d_{ts,z}}{d_{ts}} \tag{B3}$$

To determine the geometry of the collision, the cosine of the polar angle (i.e. z-component of the unit velocity vector of the gas) was sampled from a uniform distribution from -1 to 1, the azimuthal angle was sampled from a uniform distribution from 0 to 2π, and the x- and y-components of the gas vector determined as $\cos(\Phi)\times\sin(\cos^{-1}(z))$ and $\sin(\Phi)\times\sin(\cos^{-1}(z))$, respectively. The gas velocity was sampled from a Maxwell-Boltzmann distribution

$$p(v) = \left(\frac{m_g}{2\pi k_b T}\right)^{\frac{3}{2}} 4\pi v^2 e^{-m_g v^2/2k_b T_g} \tag{B4}$$

where m_g is the mass of the gas (Argon), k_b is the Boltzmann constant, and T_g is the temperature of the gas (298 K). The change in velocity due to the traveling wave potential was determined by computing the potential difference over the course of the time

$$\Delta V_{TW} = \frac{wh}{2}\left(\sin\left(kd_f - \omega t_f\right) - \sin(kd_i - \omega t_i)\right) \tag{B5}$$

where wh is the wave height, k is the wavenumber, ω is the angular frequency, d_i and t_i are the initial z position of the ion and total time, and d_f and t_f are the final z position of the ion and total time. The change in velocity due to the traveling wave was computed as

$$v_{z,new} = \sqrt{\frac{2\left(\frac{1}{2}m_i v_z^2 + z\Delta V_{TW}\right)}{m_i}} \tag{B6}$$

where v_z is the z-component of the velocity vector of the ion, if the quantity inside the square root was positive, and as

$$v_{z,new} = -\sqrt{\frac{2\left|\frac{1}{2}m_i v_z^2 + z\Delta V_{TW}\right|}{m_i}} \tag{B7}$$

if it was negative. Using this updated velocity, the velocity of the ion after the collision was computed as

$$\boldsymbol{v}_{new} = \sqrt{1-x}\left(-\boldsymbol{v} + \frac{m_i\boldsymbol{v} + m_g\boldsymbol{g}}{m_i + m_g}\right) + \frac{m_i\boldsymbol{v} + m_g\boldsymbol{g}}{m_i + m_g} \tag{B8}$$

where x is the fraction of available kinetic energy converted to internal energy, $\boldsymbol{v}$ is the velocity vector of the ion, $\boldsymbol{g}$ is the velocity vector of the gas, m_i is the mass of the ion, and m_g is the mass of the gas. The change in internal energy due to the collision was computed as

$$\Delta U = \frac{x}{2}\mu(\boldsymbol{v}\cdot\boldsymbol{v} - 2\boldsymbol{v}\cdot\boldsymbol{g} + \boldsymbol{g}\cdot\boldsymbol{g}) \tag{B9}$$

where μ is the reduced mass, for the model with only a heating mechanism and no cooling mechanism, and as

$$\Delta U = \frac{x}{2}\mu(\boldsymbol{v}\cdot\boldsymbol{v} - 2\boldsymbol{v}\cdot\boldsymbol{g} + \boldsymbol{g}\cdot\boldsymbol{g}) - \frac{3}{n}U + \frac{1}{2}m_g\boldsymbol{v}_g^2 - \frac{3}{2}k_b T_g \tag{B10}$$

where U is the cumulative change in internal energy through the previous time step, for the model incorporating both heating and cooling mechanisms. After computing the change in internal energy the simulation advanced to the next time step.

If no collision occurred during a given time step, the change in velocity due to the traveling wave was determined as above and the simulation advanced to the next time step.

Derivation of analytic expression for energy deposition in CIU without cooling

I determined an analytical expression for an extreme upper bound of energy deposition in CIU (i.e., in the absence of any cooling mechanisms) that is based on the kinetic theory of gases using the collision cross section of the ion.

For an ion-gas collision, the available center-of-mass-frame kinetic energy is given by

$$KE_{avail}^{CM} = \frac{1}{2}\mu\boldsymbol{v}_{rel}^2 = \frac{1}{2}\mu\left(\boldsymbol{v}_i - \boldsymbol{v}_g\right)\cdot\left(\boldsymbol{v}_i - \boldsymbol{v}_g\right) \quad \text{(B11)}$$

where μ is the reduced mass and $\boldsymbol{v}_i$ and $\boldsymbol{v}_g$ are the laboratory-frame velocity vectors of the ion and gas, respectively. Averaging over all possible $\boldsymbol{v}_g$ gives

$$\langle KE_{avail}^{CM}\rangle = \frac{1}{2}\mu\langle\left(\boldsymbol{v}_i - \boldsymbol{v}_g\right)\cdot\left(\boldsymbol{v}_i - \boldsymbol{v}_g\right)\rangle \quad \text{(B12)}$$

which simplifies to

$$\langle KE_{avail}^{CM}\rangle = \frac{1}{2}\mu\left(\langle\boldsymbol{v}_i^2\rangle + \langle\boldsymbol{v}_g^2\rangle\right) \quad \text{(B13)}$$

or, in terms of kinetic energy

$$\langle KE_{avail}^{CM}\rangle = \frac{m_g\langle KE_i^{lab}\rangle}{m_i+m_g} + \frac{m_i\langle KE_g^{lab}\rangle}{m_i+m_g} \quad \text{(B14)}$$

where m_i and m_g are the mass of the ion and gas, respectively, and $\langle KE_i^{lab}\rangle$ and $\langle KE_g^{lab}\rangle$ are the kinetic energies of the ion and gas, respectively. Let x be the fraction of available center-of-mass-frame kinetic energy converted to internal energy of the ion. Then the change in internal energy for a collision is

$$\langle\Delta U\rangle = x\left(\frac{m_g\langle KE_i^{lab}\rangle}{m_i+m_g} + \frac{m_i\langle KE_g^{lab}\rangle}{m_i+m_g}\right) \quad \text{(B15)}$$

and the kinetic energy after the collision is

$$\langle KE_{post\ coll}^{CM}\rangle = (1-x)\langle KE_{avail}^{CM}\rangle \quad \text{(B16)}$$

Thus, the center-of-mass-frame velocities after the collision will be those prior to the collision reversed and scaled by $\sqrt{1-x}$. Converting back to the laboratory frame I have

$$\boldsymbol{v}_{i,post\ coll} = \sqrt{1-x}\left(-\boldsymbol{v}_i + \frac{m_g\boldsymbol{v}_i + m_i\boldsymbol{v}_g}{m_i+m_g}\right) + \frac{m_g\boldsymbol{v}_i + m_i\boldsymbol{v}_g}{m_i+m_g} \tag{B17}$$

which simplifies to

$$\boldsymbol{v}_i^{post\ coll} = \boldsymbol{v}_i\left(\frac{m_g - m_i\sqrt{1-x}}{m_i+m_g}\right) \tag{B18}$$

Let $a = \left(\frac{m_g - m_i\sqrt{1-x}}{m_i+m_g}\right)^2$, then the kinetic energy of the ion after *n*-1 collisions is

$$\langle KE_{i,n-1}^{lab}\rangle = \frac{1}{2}m_i\langle\boldsymbol{v}_{i,0}^2\rangle a^{n-1} = \langle KE_{i,0}^{lab}\rangle a^{n-1} \tag{B19}$$

and the internal energy after *n* collisions is

$$\langle\Delta U_n\rangle = x\left(\frac{m_g\langle KE_{i,n-1}^{lab}\rangle}{m_i+m_g} + \frac{m_i\langle KE_g^{lab}\rangle}{m_i+m_g}\right) \tag{B20}$$

Substituting the expression for the kinetic energy of the ion from Equation B18 gives

$$\langle\Delta U_n\rangle = x\left(\frac{m_g\langle KE_{i,0}^{lab}\rangle a^{n-1}}{m_i+m_g} + \frac{m_i\langle KE_g^{lab}\rangle}{m_i+m_g}\right) \tag{B21}$$

The total change in internal energy is given by summing the change in internal energy for each collision

$$\langle\Delta U_{tot}\rangle = \sum_{n=1}^{N}\langle\Delta U_n\rangle = \sum_{n=1}^{N} x\left(\frac{m_g\langle KE_{i,0}^{lab}\rangle a^{n-1}}{m_i+m_g} + \frac{m_i\langle KE_g^{lab}\rangle}{m_i+m_g}\right) \tag{B22}$$

where *N* is the number of collisions. Terms without *n* dependence can be moved outside the summation, yielding

$$\langle\Delta U_{tot}\rangle = \frac{Nm_i x\langle KE_g^{lab}\rangle}{m_i+m_g} + \frac{m_g x\langle KE_{i,0}^{lab}\rangle}{m_i+m_g}\sum_{n=1}^{N} a^{n-1} \tag{B23}$$

If *N* is large, then the total internal energy change can be expressed as

$$\langle \Delta U_{tot} \rangle = \frac{N m_i x \langle KE_g^{lab} \rangle}{m_i + m_g} + \frac{m_g x \langle KE_{i,0}^{lab} \rangle}{m_i + m_g} \frac{1}{1-a} \tag{B24}$$

Substituting the expression for *a* and simplifying yields the final result

$$\langle \Delta U_{tot} \rangle = \frac{N m_i x \langle KE_g^{lab} \rangle}{m_i + m_g} + \frac{x(m_i + m_g) \langle KE_{i,0}^{lab} \rangle}{2 m_i \left(1 + \sqrt{1-x}\right) + m_g x} \tag{B25}$$

Derivation of Model of Collisional Activation Capable of Both Heating and Cooling

The primary computational model for CIU described in the main text includes collisional heating as well as collision cooling of the ion due to interactions with the buffer gas. (Under the conditions used in these experiments, radiative cooling by emission of photons from the ions is much slower than collisional cooling.)

To derive a model that can both heat and cool the ions, I start with an protein ion with internal energy

$$U_{i,j-1} = \Delta U_{j-1} + nk_b T_{i,0} \tag{B26}$$

where $\Delta U_{j\text{-}1}$ is the cumulative change in internal energy at step j-1, n is the number of modes, k_b is the Boltzmann constant, and $T_{i,0}$ is the initial temperature of the ion. The ion has kinetic energy

$$KE_i^{lab} = \frac{1}{2} m_i \boldsymbol{v}_i^2 \tag{B27}$$

where m_i is the mass of the ion and $\boldsymbol{v}_i$ is the velocity of the ion. The gas has energy of

$$E_g = \frac{1}{2} m_g \boldsymbol{v}_g^2 \tag{B28}$$

where m_g is the mass of the gas and $\boldsymbol{v}_g$ is the velocity of the gas. The ion and gas form a collision complex with energy

$$E_{complex} = \Delta U_{j-1} + nk_b T_{i,0} + \frac{1}{2} m_g \boldsymbol{v}_g^2 + \frac{3}{2} k_b T_g + \frac{x}{2} \mu \left(\boldsymbol{v}_i - \boldsymbol{v}_g\right) \cdot \left(\boldsymbol{v}_i - \boldsymbol{v}_g\right) \tag{B29}$$

where x is the fraction of available center-of-mass frame kinetic energy converted to internal energy and μ is the reduced mass. Note that the "extra" $\frac{3}{2} k_b T_g$ of energy arises from bonding between the ion and gas. Assuming equipartition of energy, the total energy is distributed among n+3 modes, so the gas atom carries away $\frac{1}{2} \cdot \frac{3}{n+3}$ of the total energy as kinetic energy, and another $\frac{1}{2} \cdot \frac{3}{n+3}$ goes into breaking the bonds. Thus, the internal energy of the ion after the collision is

$$U_{i,j} = \frac{n}{n+3}\left(\Delta U_{j-1} + nk_b T_{i,0} + \frac{1}{2} m_g \boldsymbol{v}_g^2 + \frac{3}{2} k_b T_g + \frac{x}{2} \mu\left(\boldsymbol{v}_i - \boldsymbol{v}_g\right) \cdot \left(\boldsymbol{v}_i - \boldsymbol{v}_g\right)\right) \qquad \text{(B30)}$$

so the change in internal energy is

$$\Delta\Delta U_i = \frac{n}{n+3}\left(\Delta U_{j-1} + nk_b T_{i,0} + \frac{1}{2} m_g \boldsymbol{v}_g^2 + \frac{3}{2} k_b T_g + \frac{x}{2} \mu\left(\boldsymbol{v}_i - \boldsymbol{v}_g\right) \cdot \left(\boldsymbol{v}_i - \boldsymbol{v}_g\right)\right) - \Delta U_{j-1} - nk_b T_{i,0} = \frac{1}{n+3}\left(\frac{1}{2} n m_g \boldsymbol{v}_g^2 + \frac{3}{2} nk_b T_g + \frac{x}{2} n\mu\left(\boldsymbol{v}_i - \boldsymbol{v}_g\right) \cdot \left(\boldsymbol{v}_i - \boldsymbol{v}_g\right) - 3\Delta U_{j-1} - 3nk_b T_{i,0}\right) \qquad \text{(B31)}$$

Assuming that the ion is initially thermalized to the temperature of the gas, i.e. $T_{i,0} = T_g$, this reduces to

$$\Delta\Delta U_i = \frac{1}{n+3}\left(\frac{1}{2} n m_g \boldsymbol{v}_g^2 - \frac{3}{2} nk_b T_g + \frac{x}{2} n\mu\left(\boldsymbol{v}_i - \boldsymbol{v}_g\right) \cdot \left(\boldsymbol{v}_i - \boldsymbol{v}_g\right) - 3\Delta U_{j-1}\right) \qquad \text{(B32)}$$

Since n is large, I have

$$\Delta\Delta U_i \approx -\frac{3}{n}\left(\Delta U_{j-1}\right) + \frac{1}{2} m_g \boldsymbol{v}_g^2 - \frac{3}{2} k_b T_g + \frac{x}{2} \mu\left(\boldsymbol{v}_i - \boldsymbol{v}_g\right) \cdot \left(\boldsymbol{v}_i - \boldsymbol{v}_g\right) \qquad \text{(B33)}$$

and the cumulative change in internal energy at step j is

$$\Delta U_j = \Delta U_{j-1} - \frac{3}{n}\left(\Delta U_{j-1}\right) + \frac{1}{2} m_g \boldsymbol{v}_g^2 - \frac{3}{2} k_b T_g + \frac{x}{2} \mu\left(\boldsymbol{v}_i - \boldsymbol{v}_g\right) \cdot \left(\boldsymbol{v}_i - \boldsymbol{v}_g\right) \qquad \text{(B34)}$$

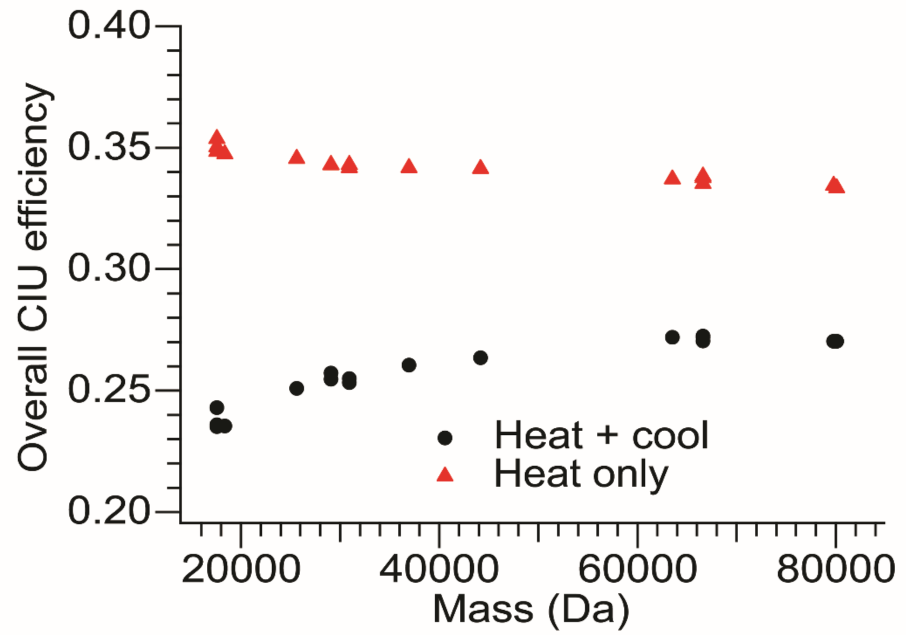

Figure B2. Computed overall CIU efficiency versus mass for each protein and charge state studied for models with heating only (red triangles) and heating and cooling (black circles). The addition of a cooling mechanism decreases the overall CIU efficiency by 20-30%. For the model with heating only the overall CIU efficiency decreases slightly with increasing mass, while for the model with heating and cooling there is a slight increase with mass, consistent with the prediction of longer cooling lifetimes for larger ions.

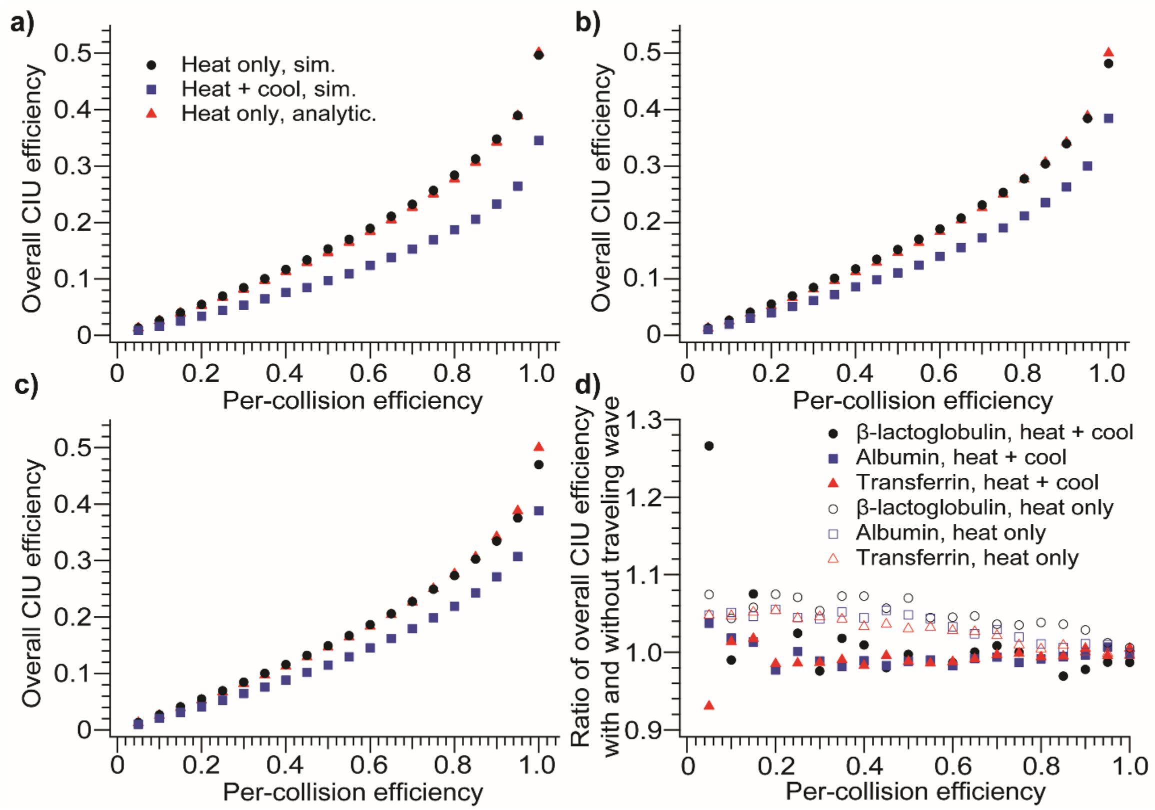

Figure B3. Comparison of overall CIU efficiencies determined from Monte Carlo simulations with (blue squares) and without (black circles) a cooling mechanism and those computed analytically (red triangles) at per-collision efficiency values ranging from 0.05 to 1 for **(a)** β-lactoglobulin, 8+ **(b)** albumin, 12+ **(c)** transferrin, 18+. For all three proteins the values computed analytically and those derived from Monte Carlo simulations without cooling are nearly identical, and the addition of a cooling mechanism decreases the overall CIU efficiency. **(d)** Effect of the traveling wave potential on the overall CIU efficiency. The ratio of the overall CIU efficiency with and without the traveling wave potential included is plotted against the per-collision efficiency. For the heating only model, the traveling wave increases the overall CIU efficiency by 5-8% at small to intermediate values of the per-collision efficiency, and has little effect at large values of the per-collision efficiency (I use a value of 0.9 to calibrate CIU data). For the model with heating and cooling, apart from very small (non-physical) values of the per-collision efficiency, the traveling wave has a negligible effect on the overall CIU efficiency.

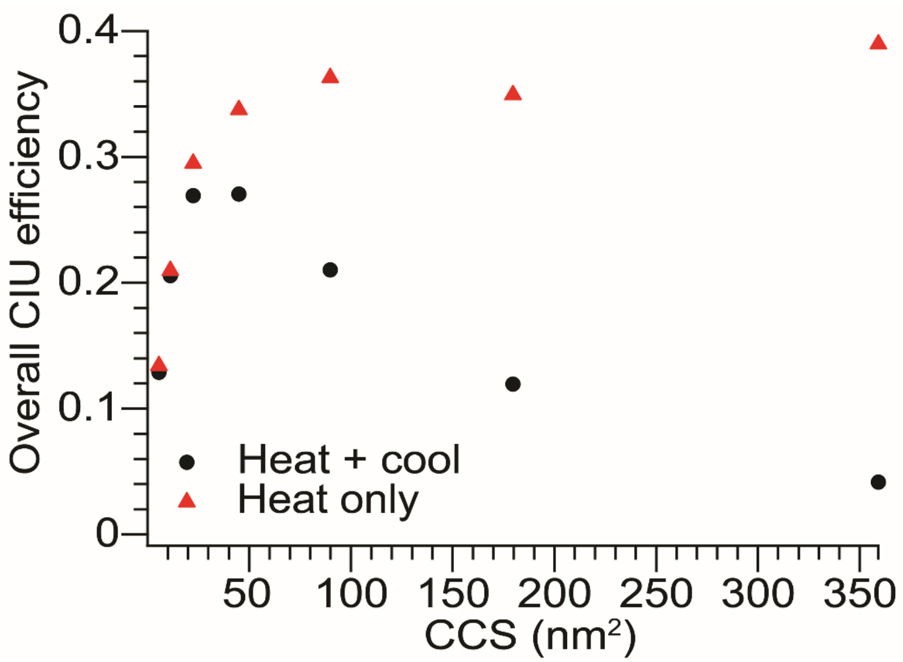

Figure B4. Computed overall CIU efficiency (ΔU/zV) for BSA^{15+} for a wide range of CCS values using a heating only model (red triangles) and one with heating and cooling mechanisms (black circles). For the heating only model there is a rapid increase in the overall CIU efficiency followed by a plateau. As the number of collisions increases, each collision transfers a smaller amount of energy to internal modes, leading to the observed behavior. For the model with both heating and cooling, there is a similarly rapid increase for small CCS values, but the overall CIU efficiency peaks near the experimental CCS value and decreases at much larger CCS values due to increased cooling from the greater number of collisions.

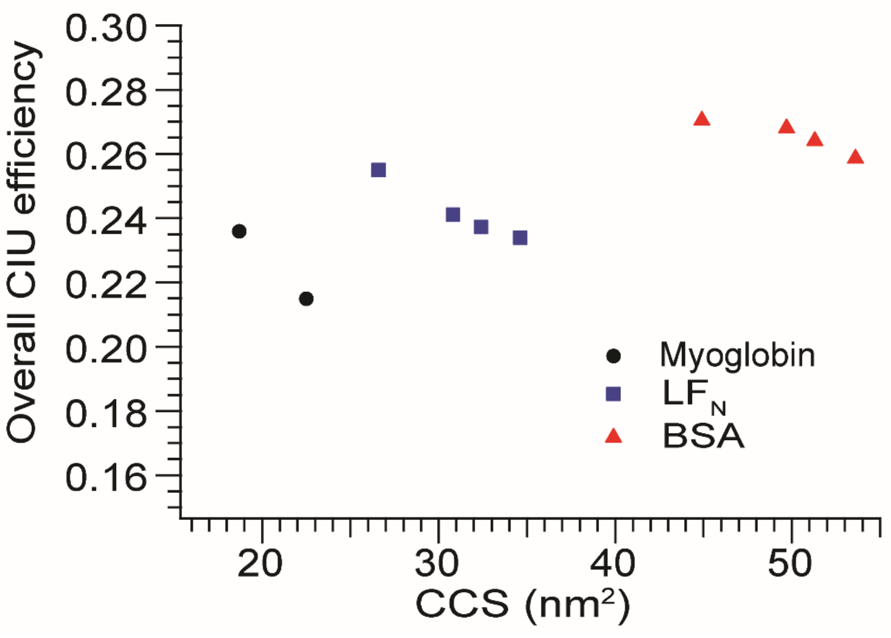

Figure B5. Computed overall CIU efficiency (ΔU/zV) for myoglobin^{7+}, LFN^{10+}, and BSA^{15+} for CCS values corresponding to experimentally determined conformer families. Increased CCS increases the number of collisions, slowing the ions down and simultaneously increasing the cooling rate. This leads to only a modest decrease in the overall CIU efficiency over the range of CCS investigated for each ion.

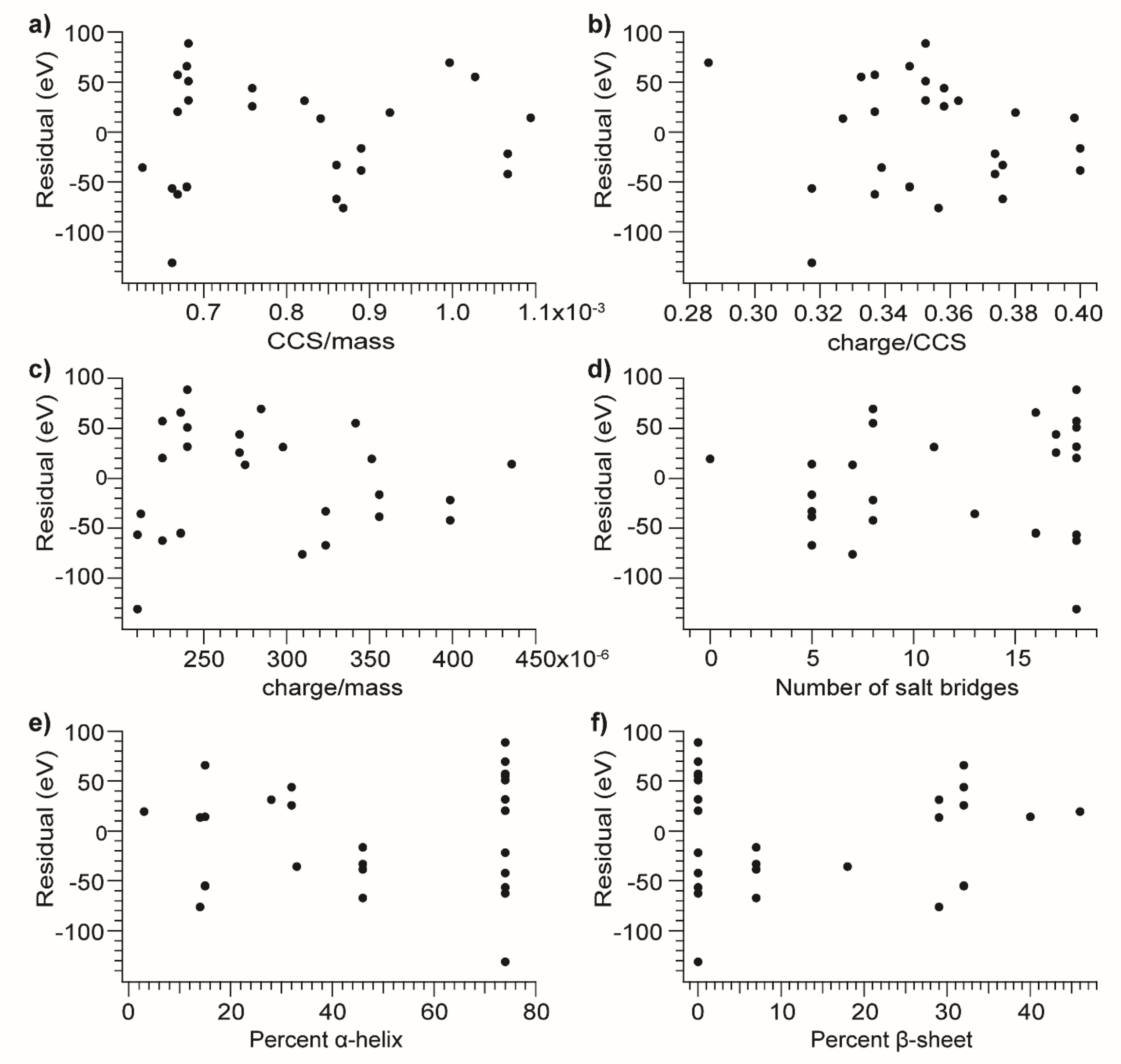

Figure B6. Plots showing relationship between residuals from power-law fit in Figure 11 and **(a)** CCS divided by mass **(b)** charge divided by CCS **(c)** charge divided by mass **(d)** number of salt bridges **(e)** amount of α-helical structure **(f)** amount of β-sheet structure. In all six cases there is no correlation.

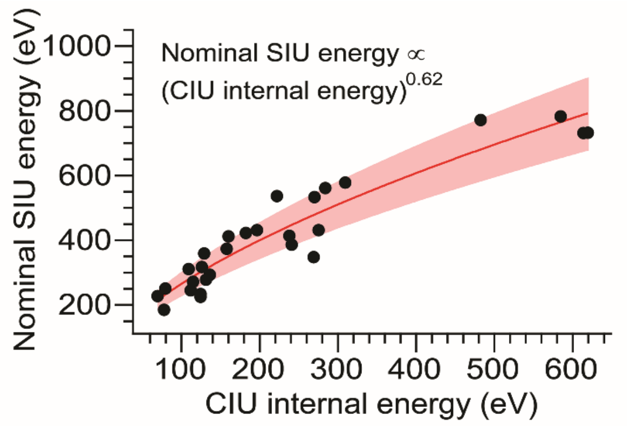

Figure B7. SIU appearance energy vs. rescaled CIU internal energy, computed using the heating only model. The non-linear trend is fit to a power law relationship with an exponent of 0.62 ± 0.05. The shaded region represents ± one standard deviation of the relative difference from the fit.

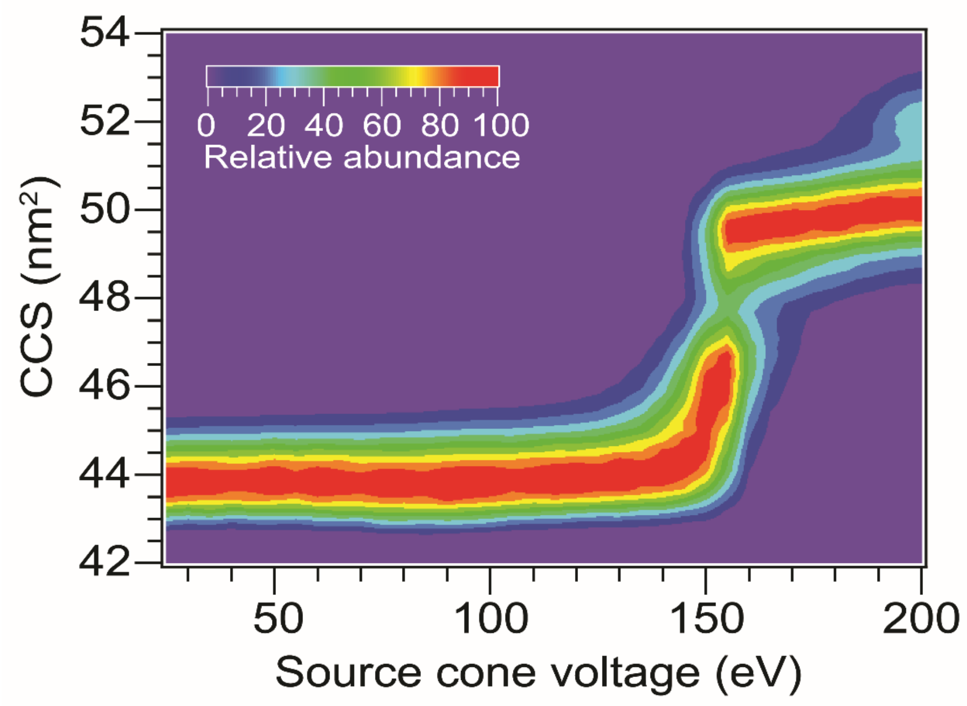

Figure B8. In-source unfolding of BSA^{15+} at a backing pressure of 3.7 mbar. The unfolding transitions observed are the same as those produced by CIU in the Trap. However, the ions are activated less efficiently in the source region, requiring higher voltages to precipitate unfolding and leading to incomplete unfolding at the voltages accessible.

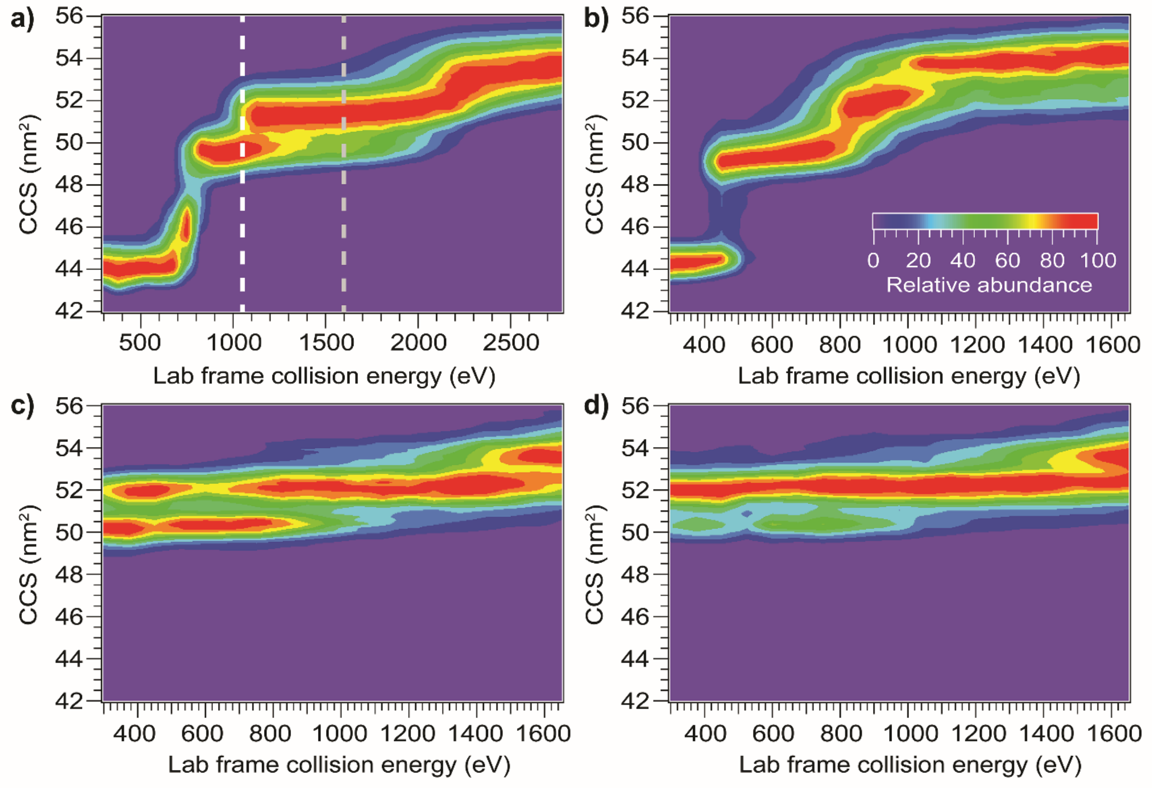

Figure B9. Effect of Trap pre-activation on SIU of BSA^{15+}. **(a)** CIU with dotted lines showing two different levels of Trap activation **(b)** SIU with no Trap activation **(c)** SIU following Trap activation to the white line in **(a)** requires significantly higher energies to cause further unfolding transitions **(d)** SIU following Trap activation up to the gray line in **(a)** also requires significantly higher energies to cause further unfolding transitions.

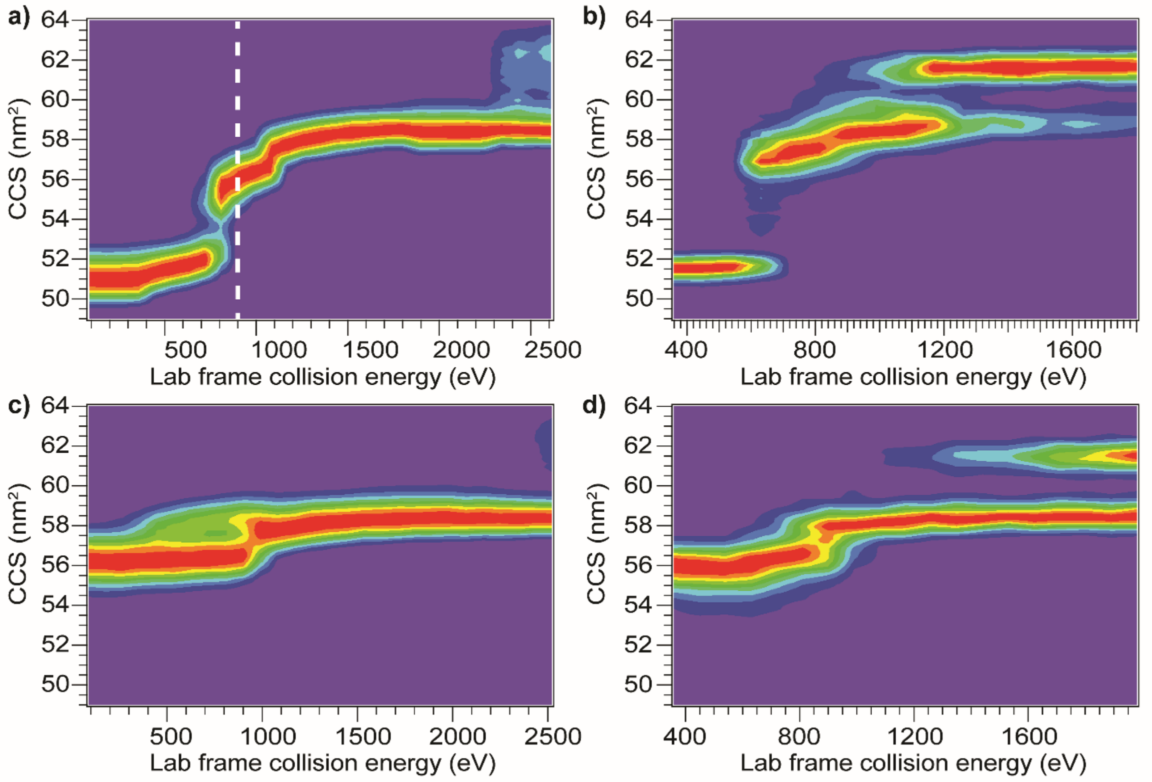

Figure B10. Effect of in-source pre-activation on CIU and SIU of TF^{18+}. **(a)** CIU with no in-source activation and dotted line showing level of pre-activation in **(c)** and **(d)**. **(b)** SIU with no in-source activation. **(c)** CIU following in-source activation up to the dotted line in **(a)** exhibits a small shift to lower energy for the discontinuity at 1200 eV in **(a)** to 1000 eV in this experiment. **(d)** SIU following in-source activation up to the dotted line in **(a)** requires more energy to cause further unfolding.

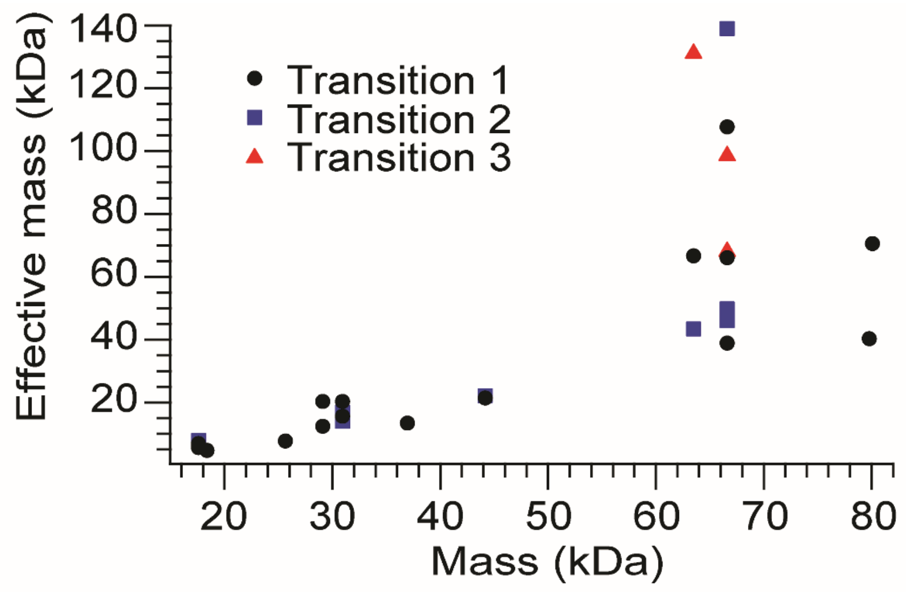

Figure B11. Effective mass of surface (see main text for definition) versus ion mass. For the first unfolding transition, the effective mass of the surface grows roughly linearly with ion mass. However, the effective mass of the surface can be much higher for the second and particularly the third unfolding transition. These transitions occur at higher energies and suggest that the ion-surface interaction depends on the kinetic energy of the ion.

APPENDIX C

SUPPLEMENTAL INFORMATION FOR CHAPTER IV: RAPID DETERMINATION OF ACTIVATION ENERGIES FOR GAS-PHASE PROTEIN UNFOLDING AND DISSOCIATION IN A Q-IM-TOF MASS SPECTROMETER

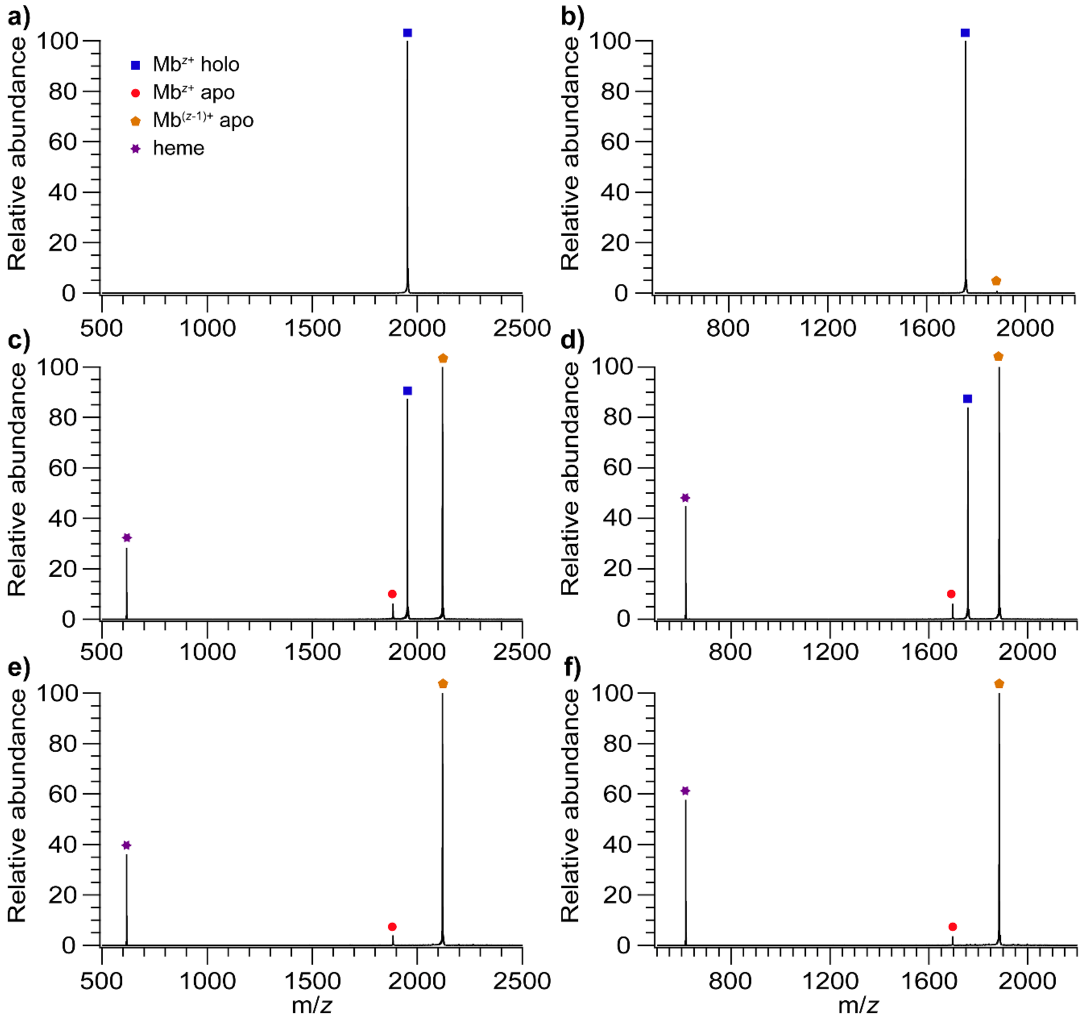

Figure C1. Mass spectra for myoglobin, 9+, at **(a)** 10 V Trap CE **(c)** 45 V Trap CE **(e)** 60 V Trap CE, and for myoglobin, 10+, at **(b)** 10 V Trap CE **(d)** 40 V Trap CE **(f)** 55 V Trap CE. The primary dissociation pathway is through loss of charged heme. However, a small amount of reduced iron is present, leading to loss of neutral heme and the small apo-myoglobin peak with the same charge as the precursor, identified by the red circles.

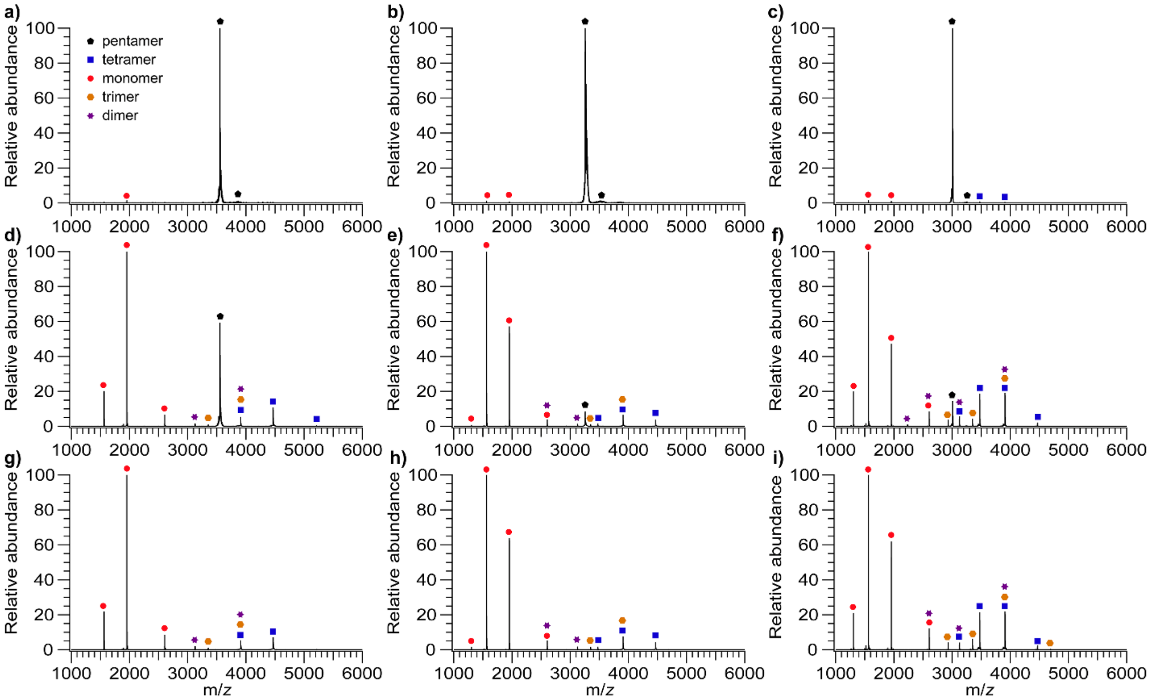

Figure C2. Mass spectra for Shiga toxin 1 B, 11+, at **(a)** 30 V Trap CE **(d)** 40 V Trap CE **(g)** 55 V Trap CE, for Shiga toxin 1 B, 12+, at **(b)** 20 V Trap CE **(e)** 35 V Trap CE **(h)** 50 V Trap CE, and for Shiga toxin 1 B, 13+, at **(c)** 20 V Trap CE **(f)** 30 V Trap CE **(i)** 40 V Trap CE. The predominant dissociation products in each case are monomer and the complementary tetramer. A small amount of dimer and complementary trimer are also observed. No evidence of secondary dissociation is observed, as all product species increase, then plateau, and none decrease in relative abundance at the collision energies studied.

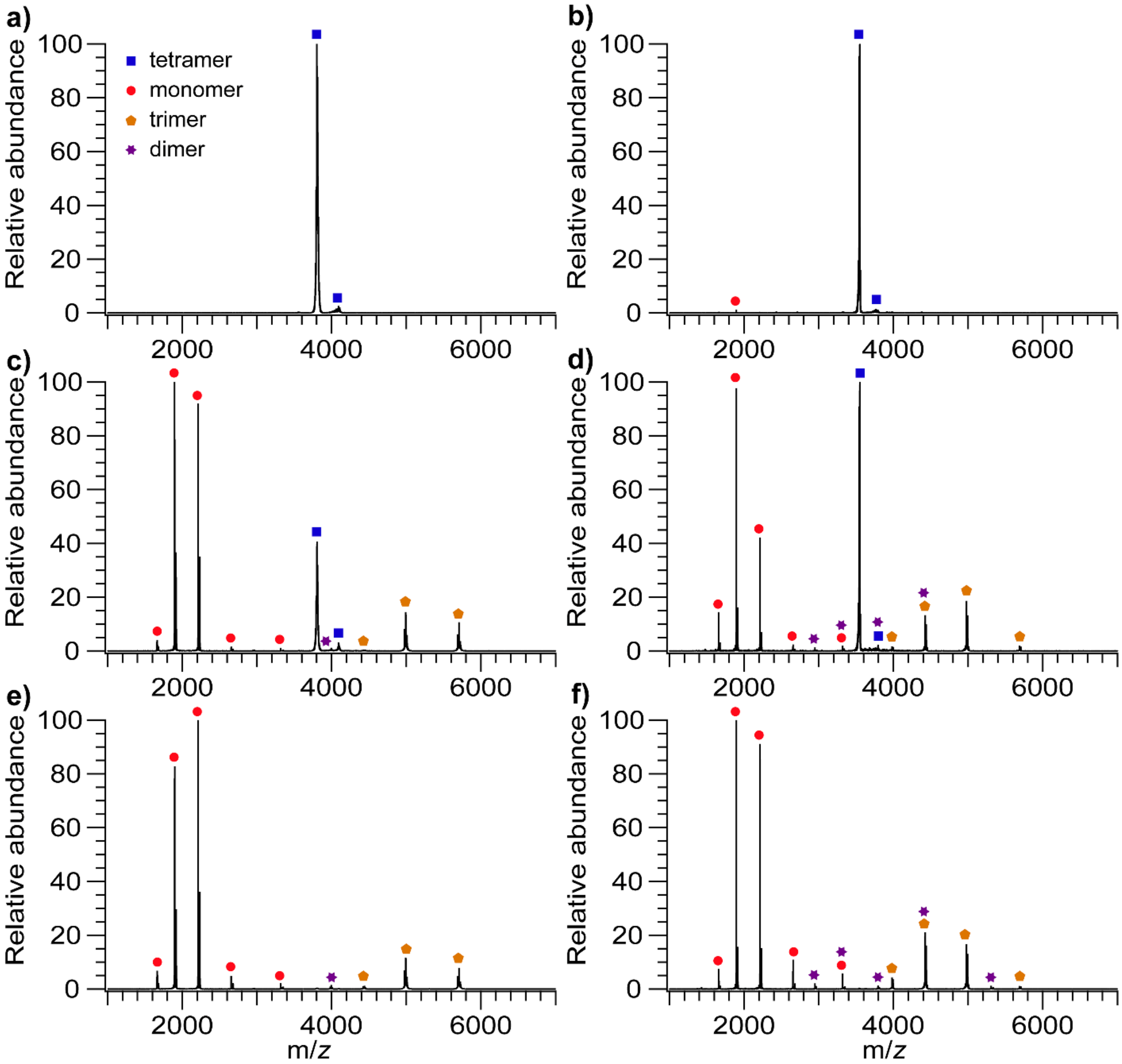

Figure C3. Mass spectra for streptavidin, 14+, at **(a)** 30 V Trap CE **(c)** 50 V Trap CE **(e)** 65 V Trap CE **(b)** 25 V Trap CE **(d)** 40 V Trap CE **(f)** 60 V Trap CE. The predominant dissociation products in both cases are monomer and the complementary trimer. A very small amount of dimer (< 1%) is also observed. No evidence of secondary dissociation is observed, as all product species increase, then plateau, and none decrease in relative abundance at the collision energies studied.

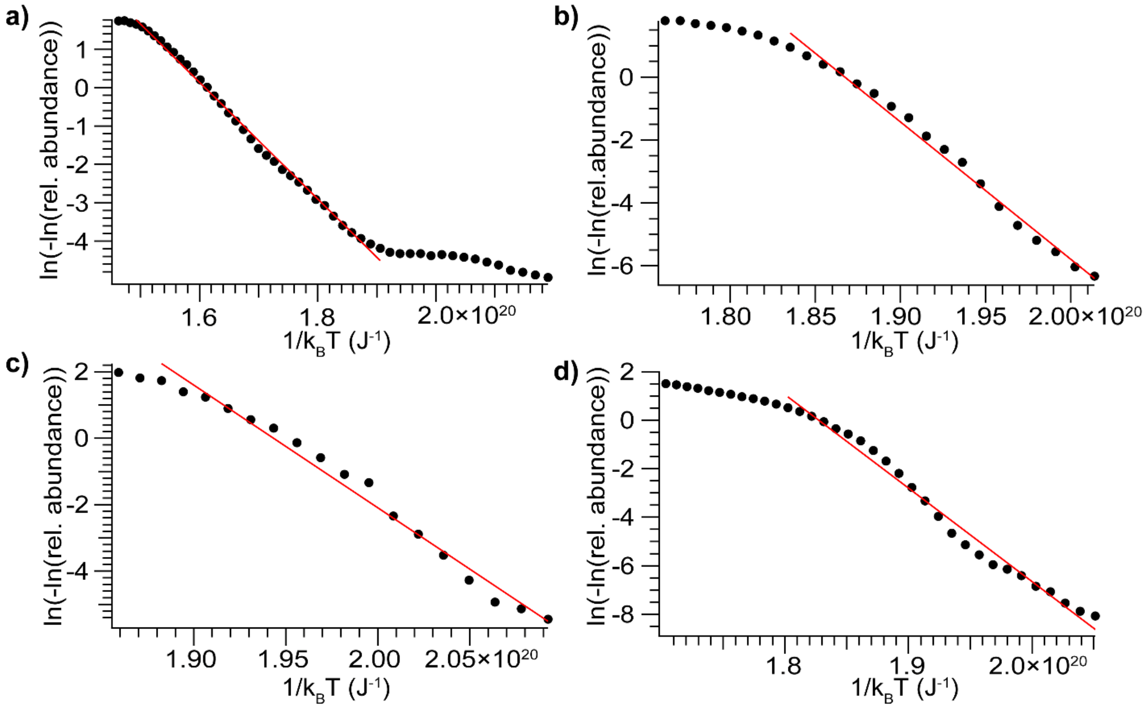

Figure C4. Plots of the double natural logarithm of precursor relative abundance versus inverse vibrational temperature for **(a)** myoglobin, 9+ **(b)** Shiga toxin 1 B, 11+ **(c)** Shiga toxin 1 B, 13+ and **(d)** streptavidin, 15+. In **(a)** a small amount of interfering dissociation due to activation during the isolation in the quadrupole is observed and is responsible for the plateau at low value of the laboratory-frame energy.

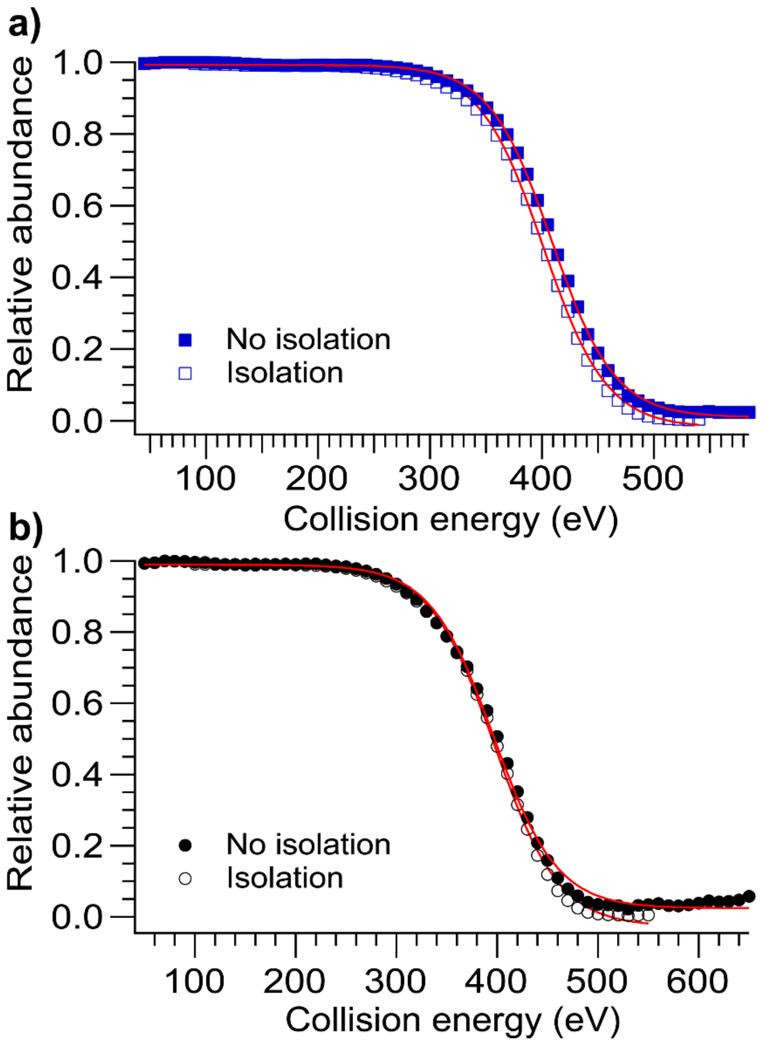

Figure C5. Plots of relative abundance versus laboratory-frame collision energy for **(a)** myoglobin, 9+ with and without isolation and **(b)** myoglobin, 10+ with and without isolation. The breakdown curves have been fit with sigmoidal functions to assess heating in the quadrupole, which would cause a shift in the curves toward lower energies upon isolation. For myoglobin, 9+ a small shift in the midpoint of the sigmoid of approximately 7 eV is observed – this corresponds to an effect of less than 2%. For myoglobin, 10+, despite an apparent small shift in the position of the curves, no difference in the midpoint of the sigmoids is found. The shift for the 10+ charge state is noticeably lower than for the 9+ charge state, so any effect that exists is significantly smaller than 2%. In both cases the isolation does not significantly affect the results.

Table C1. Results of reproducibility experiments.

Protein	**Charge**	**Trial**	**E_a (kJ/mol)**
Shiga toxin 1 B	13+	1	222
		2	207
		3	202
		4	201
		Average	**208±10**
Streptavidin	15+	1	232
		2	223
		3	217
		4	222
		Average	**224±6**

Table C2. Effect of differential transmission on measured E_a values.

			E_a (kJ/mol)			Percent difference	
Protein	Charge	Trial	Monomer	Average	(n-1)-mer	Average	(n-1)-mer
Shiga toxin 1 B	13+	1	207	210	213	1.5%	3.0%
		2	202	206	209	1.7%	3.4%
		3	201	204	206	1.4%	2.8%
Streptavidin	15+	1	223	229	236	2.3%	5.6%
		2	217	223	231	2.6%	6.2%
		3	222	228	236	2.5%	5.9%

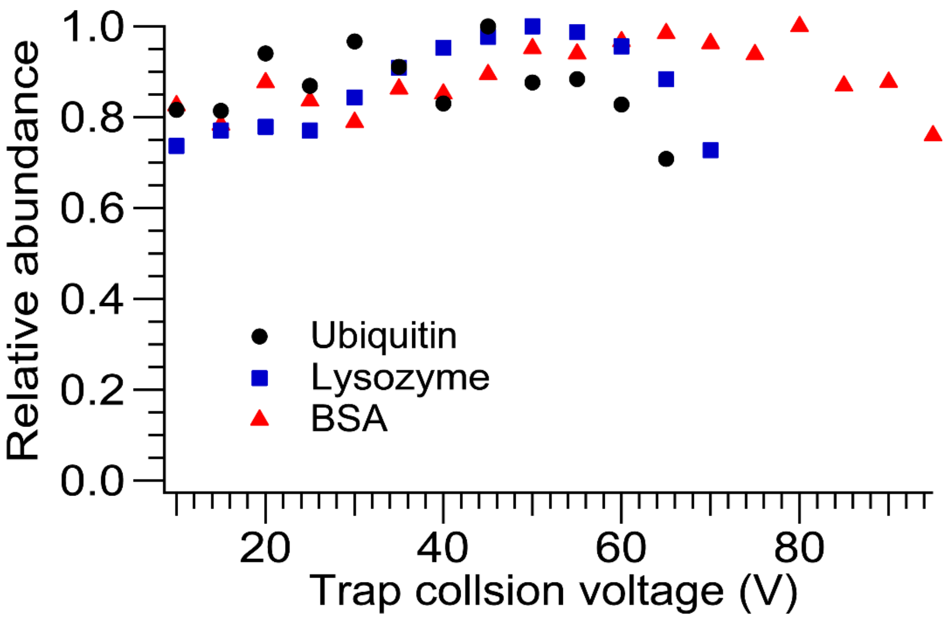

Figure C6. Variation in signal with collision voltage for selected protein monomers ranging from 8.5 kDa to 66 kDa in mass. The relative abundance varies by ±10% in the range studied.

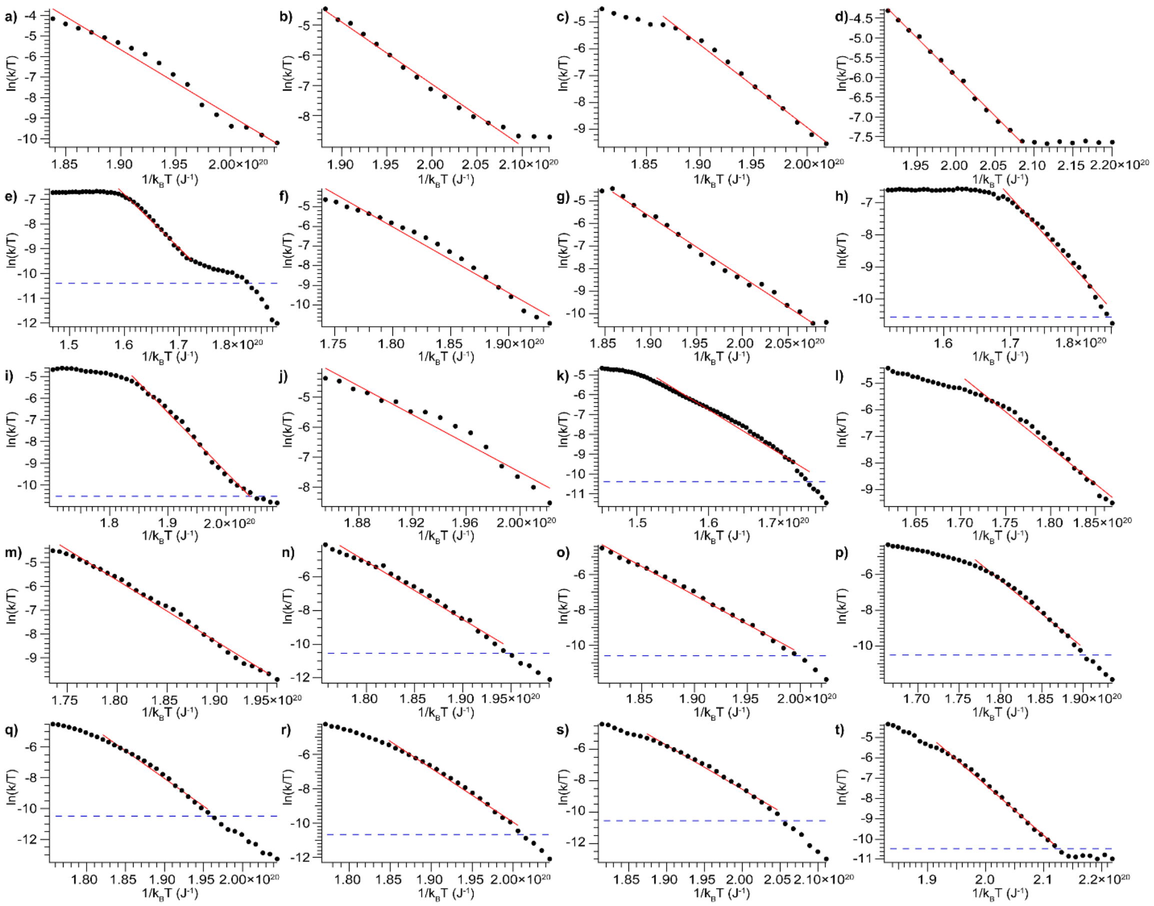

Figure C7. Plots of the natural logarithm of the effective rate constant divided by temperature versus inverse vibrational temperature for **(a)** β-lactoglobulin, 7+ **(b)** β-lactoglobulin, 8+ **(c)** concanavalin A, 9+ **(d)** concanavalin A, 10+ **(e)** carbonic anhydrase II, 8+ **(f)** carbonic anhydrase II, 9+ **(g)** carbonic anhydrase II, 10+ **(h)** alcohol dehydrogenase, 9+ **(i)** alcohol dehydrogenase, 10+ **(j)** alcohol dehydrogenase, 11+ **(k)** bovine serum albumin, 12+ **(l)** bovine serum albumin, 13+ **(m)** bovine serum albumin, 14+ **(n)** bovine serum albumin, 15+ **(o)** bovine serum albumin, 16+ **(p)** transferrin, 15+ **(q)** transferrin, 16+ **(r)** transferrin, 17+ **(s)** transferrin, 18+ and **(t)** transferrin, 19+. The blue dashed lines show the threshold for quantitation (>1% unfolded conformer family). The corresponding threshold for the disappearance of the compact conformer family (>99% unfolded conformer family) is not shown, as many of the data sets have no points in that range.

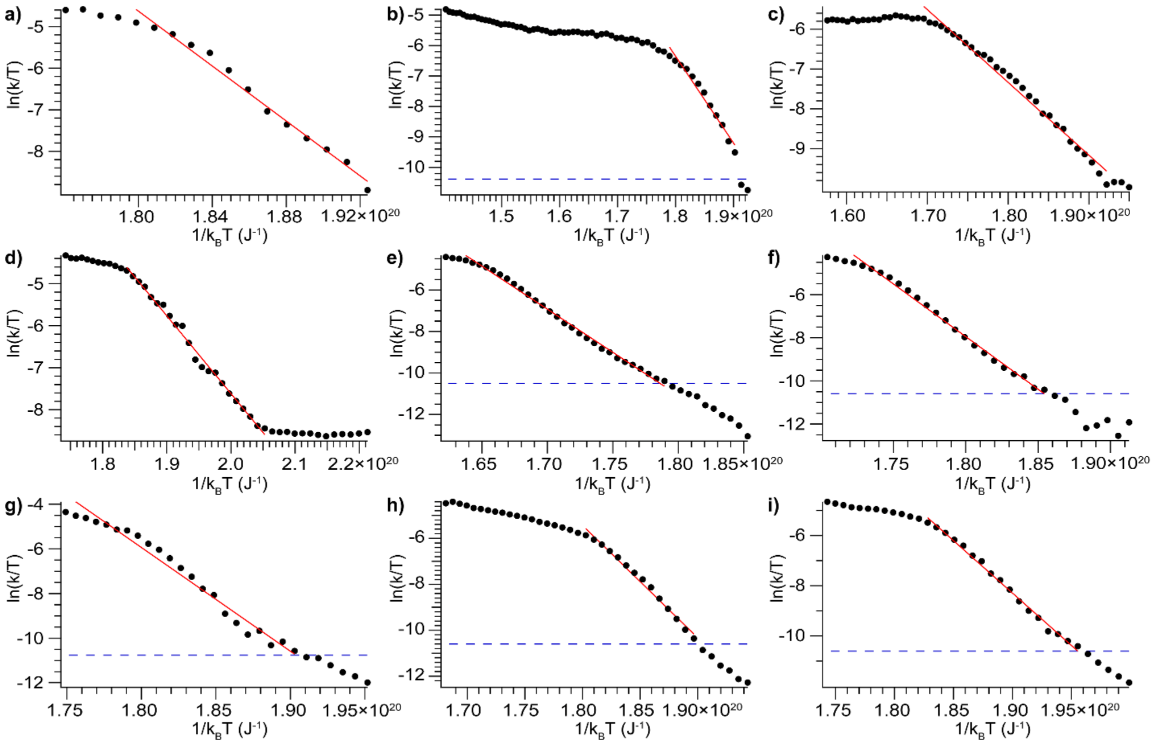

Figure C8. Plots of the natural logarithm of the effective rate constant divided by temperature versus inverse vibrational temperature for **(a)** carbonic anhydrase II, 9− **(b)** concanavalin A, 8− **(c)** alcohol dehydrogenase, 9− **(d)** alcohol dehydrogenase, 10− **(e)** bovine serum albumin, 12− **(f)** bovine serum albumin, 13− **(g)** bovine serum albumin, 14− **(h)** transferrin, 15− and **(i)** transferrin, 16−. The blue dashed lines show the threshold for quantitation (>1% unfolded conformer family). The corresponding threshold for the disappearance of the compact conformer family (>99% unfolded conformer family) is not shown, as many of the data sets have no points in that range.

Table C3. Activation parameters for unfolding of protein cations.

Protein	**Charge**	**ΔH‡ (kJ/mol)**	**ΔS‡ (J/mol·K)**	**ΔG‡ (kJ/mol)**
β-lactoglobulin	7+	205±13	353±16	73.4±16.0
β-lactoglobulin	8+	123±7	145±5	70.4±7.3
Concanavalin A	8+	140±10	141±6	83.3±11.0
Concanavalin A	9+	186±11	299±11	73.9±13.0
Concanavalin A	10+	119±6	140±3	67.8±6.2
Carbonic anhydrase	8+	131±11	93±4	90.1±11.6
Carbonic anhydrase	9+	192±15	289±15	77.2±17.4
Carbonic anhydrase	10+	160±9	235±6	73.6±9.8
Alcohol dehydrogenase	9+	141±11	135±6	85.2±11.7
Alcohol dehydrogenase	10+	165±9	239±6	75.0±10.6
Alcohol dehydrogenase	11+	149±12	211±15	71.6±13.6
Alcohol dehydrogenase	12+	135±7	171±4	71.4±8.0
Bovine serum albumin	12+	133±10	103±4	87.5±10.1
Bovine serum albumin	13+	163±12	207±8	79.0±13.5
Bovine serum albumin	14+	156±11	202±4	76.5±12.6
Bovine serum albumin	15+	207±14	335±11	76.5±16.2
Bovine serum albumin	16+	198±11	322±7	75.2±13.5
Transferrin	15+	227±15	373±12	79.1±18.5
Transferrin	16+	216±14	362±12	77.1±16.5
Transferrin	17+	189±11	302±9	75.6±12.9
Transferrin	18+	169±9	257±8	73.7±10.8
Transferrin	19+	149±7	213±5	72.5±7.8

Table C4. Activation parameters for unfolding of protein anions.

Protein	**Charge**	**$\Delta H^{\ddagger}$ (kJ/mol)**	**$\Delta S^{\ddagger}$ (J/mol·K)**	**$\Delta G^{\ddagger}$ (kJ/mol)**
Concanavalin A	8−	172±14	233±15	79.8±16.0
Carbonic anhydrase	9−	199±14	318±13	75.1±16.5
Alcohol dehydrogenase	9−	110±8	73.4±3	80.5±7.9
Alcohol dehydrogenase	10−	112±6	107±3	71.8±6.5
Bovine serum albumin	12−	250±19	394±7	83.4±22.7
Bovine serum albumin	13−	294±20	527±11	79.8±25.1
Bovine serum albumin	14−	280±20	507±21	78.2±25.3
Transferrin	15−	295±20	550±19	79.4±24.8
Transferrin	16−	251±15	452±10	77.9±18.1

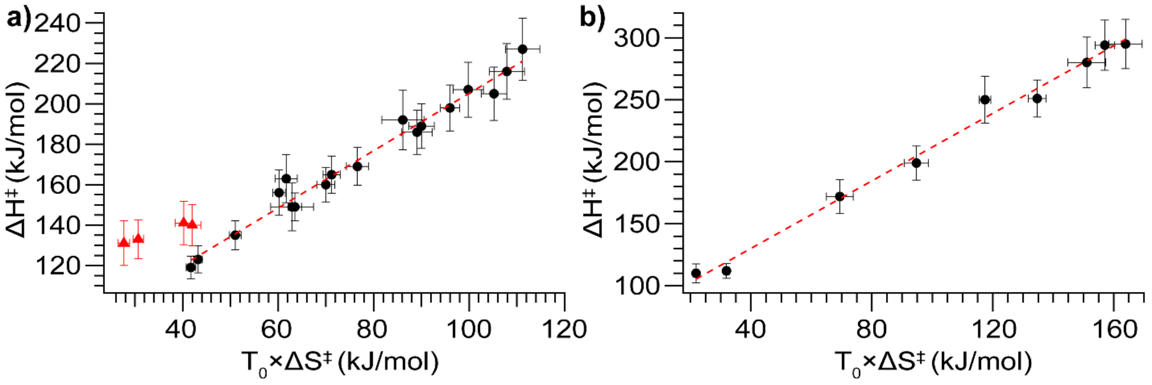

Figure C9. Plot of ΔH‡ versus $T_0 \times \Delta S^{\ddagger}$ (where T_0 = 298 K) for **(a)** positive and **(b)** negative ions. The black circles correspond to species that fully unfold, and the red triangles correspond to species that reach a quasi-equilibrium between compact and unfolded states. The red dotted lines are linear fits to the data, with slopes of 1.42±0.06 in **(a)** and 1.36±0.05 in **(b)**.

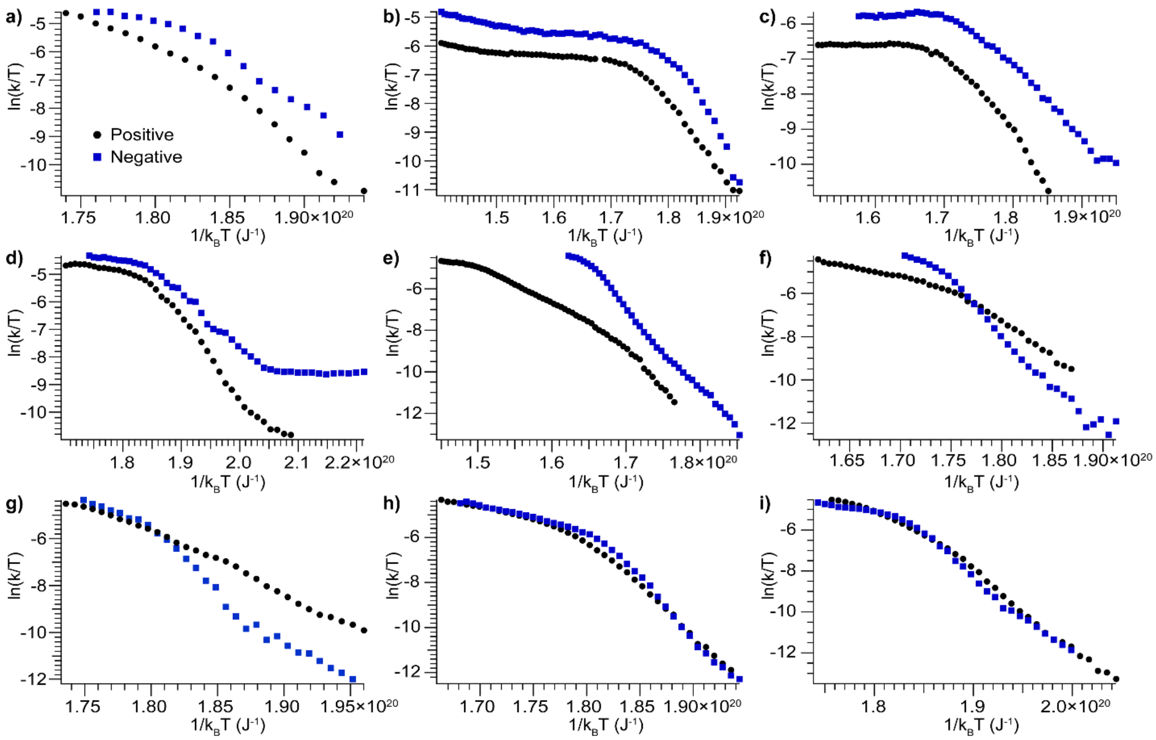

Figure C10. Plots comparing unfolding for protein cations (black circles) and anions (blue squares). **(a)** carbonic anhydrase II, 9+ and 9− **(b)** concanavalin A, 8+ and 8− **(c)** alcohol dehydrogenase, 9+ and 9− **(d)** alcohol dehydrogenase, 10+ and 10− **(e)** bovine serum albumin, 12+ and 12− **(f)** bovine serum albumin, 13+ and 13− **(g)** bovine serum albumin, 14+ and 14− **(h)** transferrin, 15+ and 15− and **(i)** transferrin, 16+ and 16−.

Instrumental Limitations on Accessible Energies

It is important to consider the effect of instrumental capabilities on the range of transitions that can be observed and quantified. This work uses a Waters Synapt G2-Si, which allows tuning of the collision voltage between 0-200 V (in practice I find that voltages below 10 V have no discernible effect) and has no control of reaction time. The estimated reaction time and the range of temperatures accessible (based on protein size and the instrumental range of collision voltages), were used to calculate the range of $\Delta G^{\ddagger}$ values that can be probed on a Synapt G2-Si. Ranges of $\Delta G^{\ddagger}$ values were determined by substituting the following expression, $k = \frac{\ln 2}{t}$, obtained from the first-order rate equation by assuming a ratio of precursor to total ion abundance of ½ (i.e. starting with 50% compact conformer at the low end, or ending with 50% unfolded conformer at the high end) into the Eyring equation, $k = \frac{k_B T}{h} e^{-\Delta G^{\ddagger}/RT}$, and solving for $\Delta G^{\ddagger}$ to give the following expression

$$\Delta G^{\ddagger} = RT \ln\left(\frac{t k_B T}{h \ln 2}\right) \tag{C1}$$

In the preceding expression t is the reaction time, h is Planck's constant, k_B is the Boltzmann constant, R is the gas constant, and T is the effective temperature. High and low bounds for $\Delta G^{\ddagger}$ were computed by calculating maximum and minimum T values, respectively, based on the high and low Trap collision voltages available and the characteristics of the protein ion in question.

Data computed following the above procedure are shown in Figure C11. The lower bound of the range falls at approximately 60 kJ/mol for small to very large proteins. The upper bound varies more with protein size, from almost 200 kJ/mol for a small protein such as ubiquitin (8.5 kDa), down to ~80 kJ/mol for a protein the size of GroEL (800 kDa). Practically, accessing lower energy transitions would require either cooling the ions below 298 K or finer control over ion initial and final internal energy distributions. Multiple groups have developed variable-temperature ion mobility devices,[266,267] and in principle the temperature of the collision cell used for activation could be similarly controlled. Increasing the upper bound of accessible energies could be accomplished either by increasing the laboratory frame energy of the collisions or increasing the available reaction time. The latter follows the operating principles of CID in an FT-ICR, in which ions can be heated and stored for many seconds before detection. While the reaction time in a Synapt G2-S*i* is both fairly short (tens of microseconds) and fixed, new developments in traveling wave ion guides such as Structures for Lossless Ion Manipulations (SLIMs) and cyclic ion mobility devices could enable much longer reaction times (milliseconds to many seconds) to be used, reducing the kinetic shift and thus making accurate determinations for higher-energy transitions accessible.

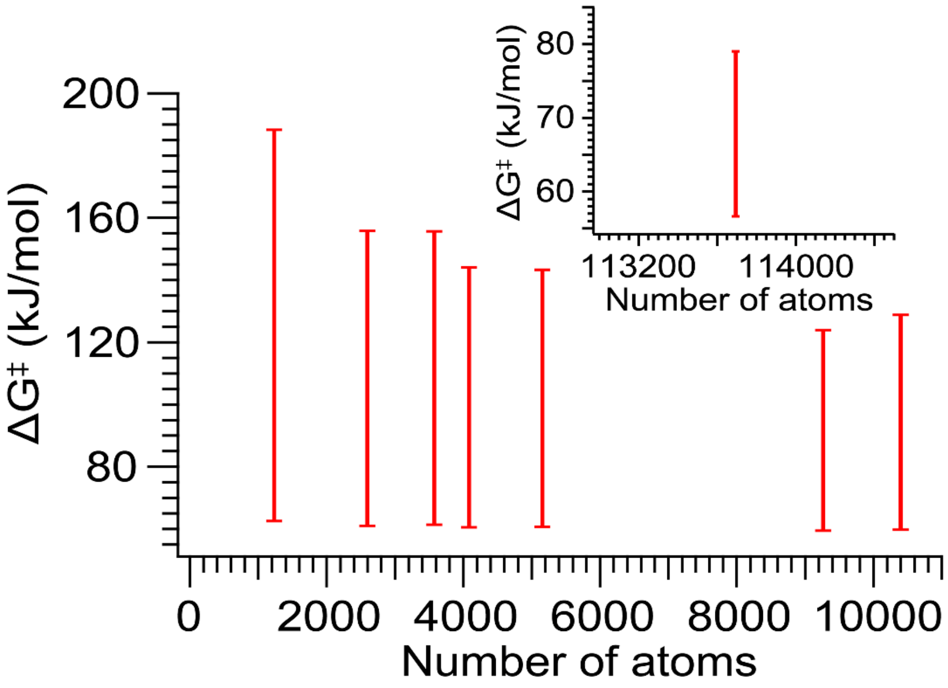

Figure C11. Plot of the estimated range of $\Delta G^{\ddagger}$ values that can be studied using a Waters Synapt G2-S*i* versus the number of atoms for selected protein ions. Inset shows data computed for GroEL.

APPENDIX D

SUPPLEMENTAL INFORMATION FOR CHAPTER V: EXTENT AND ENERGETICS OF NON-SPECIFIC BINDING BETWEEN LIPID HEAD GROUPS AND SOLUBLE PROTEINS

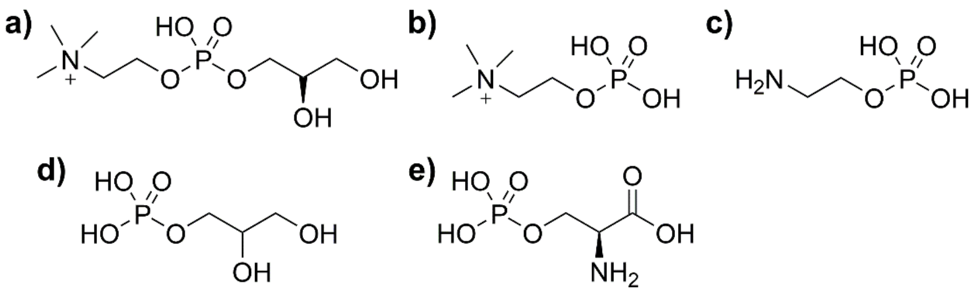

Figure D1. Structures of lipid head groups **(a)** glycerophosphorylcholine, GPC **(b)** phosphorylcholine, PC **(c)** phosphorylethanolamine, PE **(d)** glycerol 1-phosphate, PG and **(e)** phosphoserine, PS.

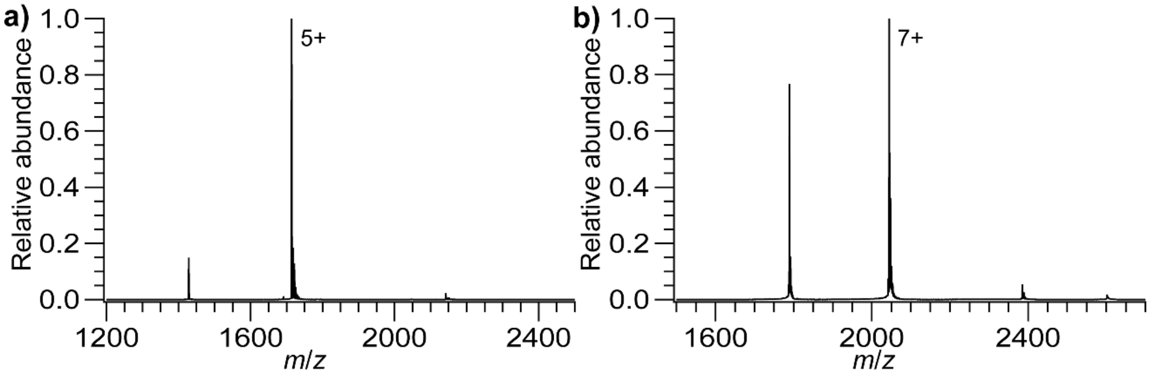

Figure D2. Mass spectra of **(a)** ubiquitin (Ubq) and **(b)** lysozyme (LZ). For both, the most abundant charge state, which was used for CID experiments, is labeled.

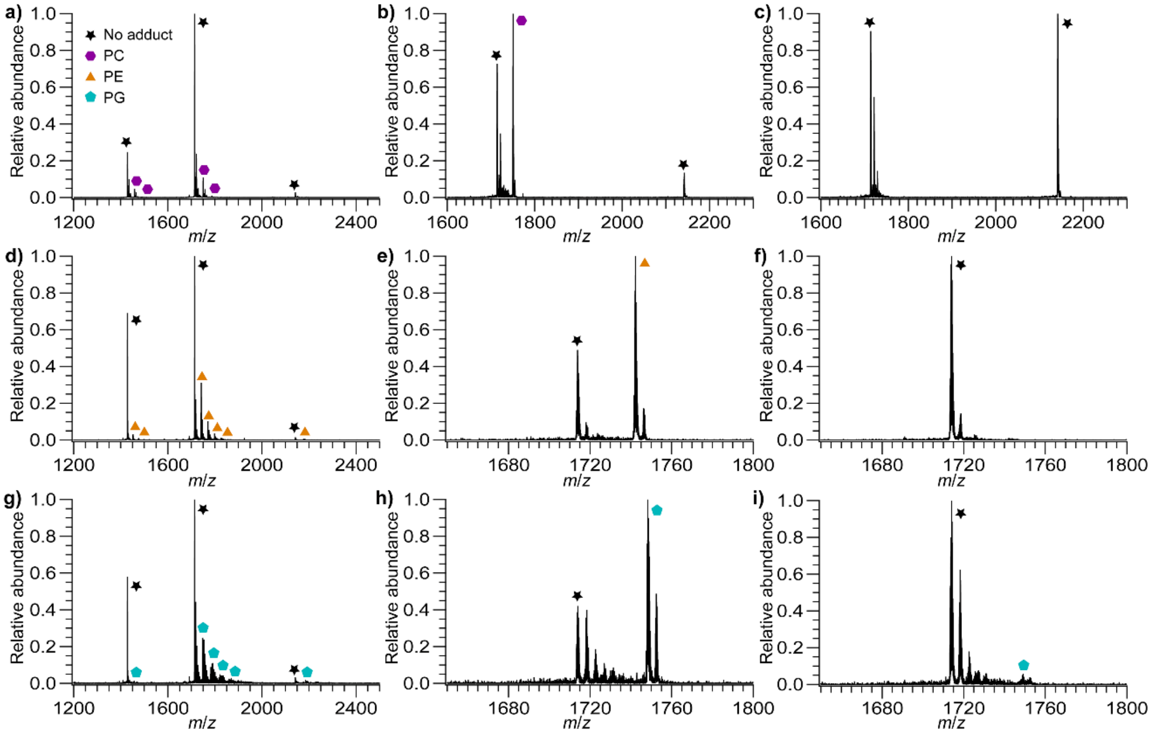

Figure D3. Mass spectra of PC, PE, and PG bound to Ubq. **(a)** Ubq with PC bound **(b)** isolated Ubq^{5+} with PC bound at low activation **(c)** isolated Ubq^{5+} with PC bound at high activation **(d)** Ubq with PE bound **(e)** isolated Ubq^{5+} with PE bound at low activation **(f)** isolated Ubq^{5+} with PE bound at high activation **(g)** Ubq with PG bound **(h)** isolated Ubq^{5+} with PG bound at low activation **(i)** isolated Ubq^{5+} with PG bound at high activation. PG and PE bind more extensively than does PC. In the isolated spectra at low activation there is some Ubq with no adducts present, due to a combination of imperfect mass selection (most prominent in the PC spectra) as well as dissociation due to the isolation (most prevalent in the PE and PG spectra).

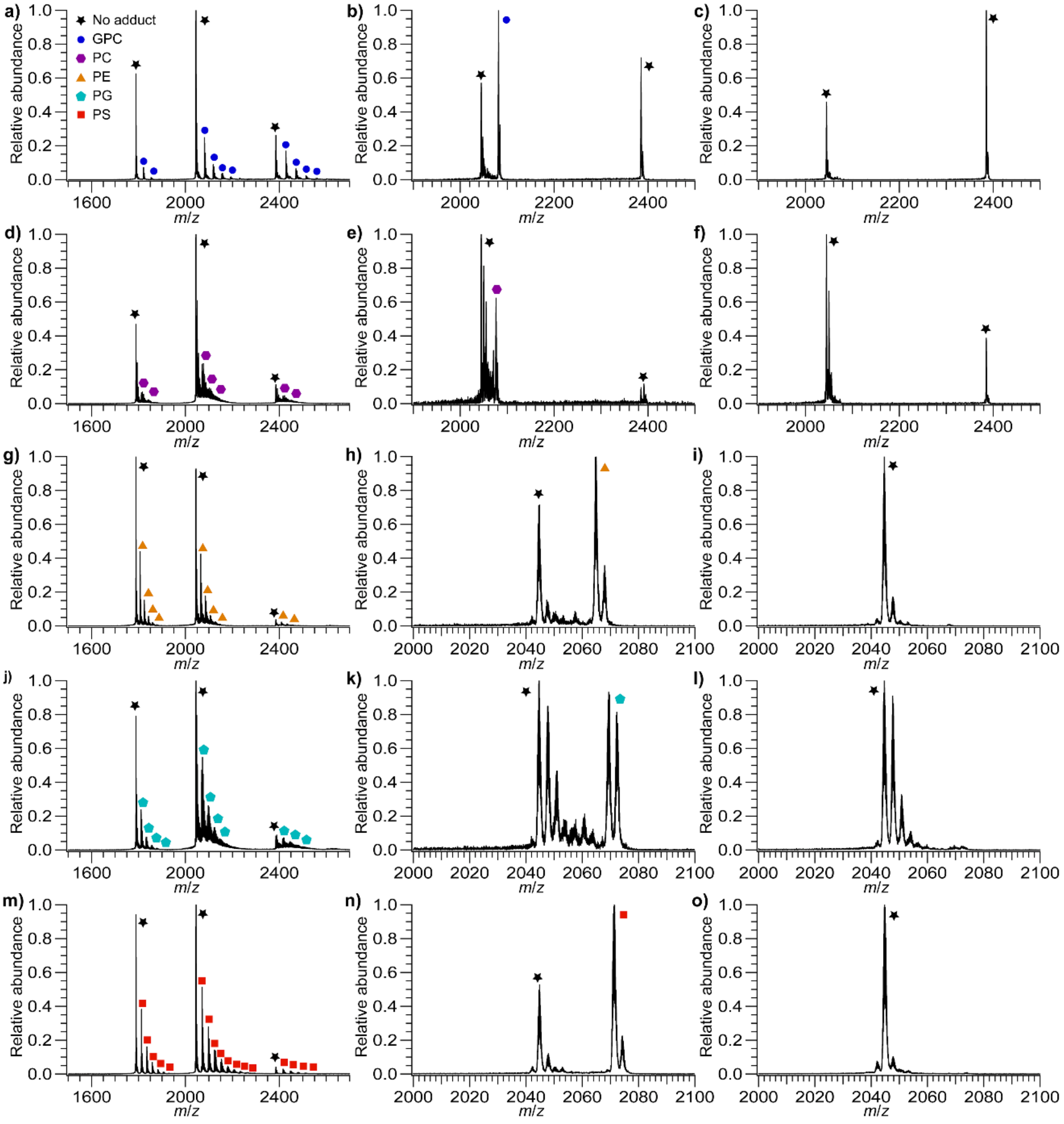

Figure D4. Mass spectra of GPC, PC, PE, PG, and PS bound to LZ. **(a)** LZ with GPC bound **(b)** isolated LZ^{7+} with GPC bound at low activation **(c)** isolated LZ^{7+} with GPC bound at high activation **(d)** LZ with PC bound **(e)** isolated LZ^{7+} with PC bound at low activation **(f)** isolated LZ^{7+} with PC bound at high activation **(g)** LZ with PE bound **(h)** isolated LZ^{7+} with PE bound at low activation **(i)** isolated LZ^{7+} with PE bound at high activation **(j)** LZ with PG bound **(k)** isolated LZ^{7+} with PG bound at low activation **(l)** isolated LZ^{7+} with PG bound at high activation **(m)** LZ with PS bound **(n)** isolated LZ^{7+} with PS bound at low activation **(o)** isolated LZ^{7+} with PS bound at high activation. PS binds the most extensively, PC the least, with GPC, PE, and PG falling in between. In the isolated spectra at low activation there is some LZ with no adducts, due to a combination of imperfect isolation and dissociation due to the isolation.

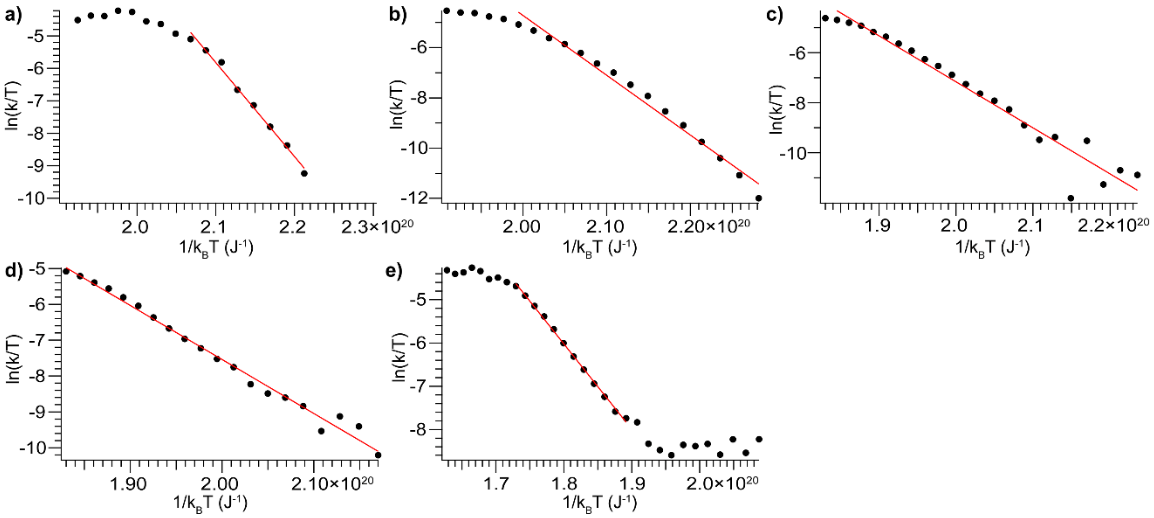

Figure D5. Eyring plots for CID of ubiquitin, 5+ losing bound lipid head groups **(a)** GPC **(b)** PC **(c)** PE **(d)** PG and **(e)** PS. The slope of the fit line gives the activation enthalpy and the intercept gives the activation entropy.

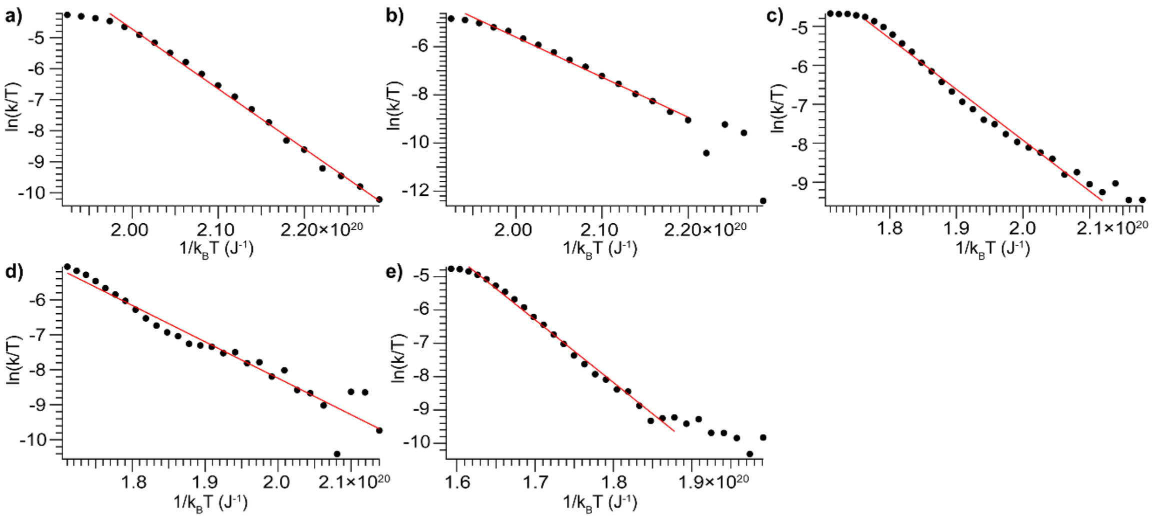

Figure D6. Eyring plots for CID of lysozyme, 7+ losing bound lipid head groups **(a)** GPC **(b)** PC **(c)** PE **(d)** PG and **(e)** PS. The slope of the fit line gives the activation enthalpy and the intercept gives the activation entropy.

Table D1. Activation enthalpies and entropies for lipid head group CID.

	Ubiquitin, 5+		Lysozyme, 7+	
Head group	$\Delta H^{\ddagger}$ (kJ/mol)	$\Delta S^{\ddagger}$ (J/mol·K)	$\Delta H^{\ddagger}$ (kJ/mol)	$\Delta S^{\ddagger}$ (J/mol·K)
GPC	194±12	377±22	116±4	144±4
PC	143±7	218±10	100±4	91.7±3.6
PE	111±7	108±7	78.6±4.5	13.0±2.5
PG	91±5	50.0±2.7	62.7±4.7	-33.6±3.7
PS	119±8	108±3	113±9	75.1±3.2

REFERENCES CITED

(1) Zhang, Y.; Fonslow, B. R.; Shan, B.; Baek, M.-C.; Yates, J. R. Protein Analysis by Shotgun/Bottom-up Proteomics. *Chem. Rev.* **2013**, *113*, 2343-2394.

(2) Rochfort, S. Metabolomics Reviewed: A New "Omics" Platform Technology for Systems Biology and Implications for Natural Products Research. *Journal of Natural Products* **2005**, *68*, 1813-1820.

(3) Brügger, B. Lipidomics: Analysis of the Lipid Composition of Cells and Subcellular Organelles by Electrospray Ionization Mass Spectrometry. *Annu. Rev. Biochem.* **2014**, *83*, 79-98.

(4) Kostyukevich, Y.; Acter, T.; Zherebker, A.; Ahmed, A.; Kim, S.; Nikolaev, E. Hydrogen/deuterium exchange in mass spectrometry. *Mass Spectrom. Rev.* **2018**, *37*, 811-853.

(5) Johnson, D. T.; Di Stefano, L. H.; Jones, L. M. Fast photochemical oxidation of proteins (FPOP): A powerful mass spectrometry–based structural proteomics tool. *J. Biol. Chem.* **2019**, *294*, 11969-11979.

(6) Gillet, L. C.; Leitner, A.; Aebersold, R. Mass Spectrometry Applied to Bottom-Up Proteomics: Entering the High-Throughput Era for Hypothesis Testing. *Annual Review of Analytical Chemistry* **2016**, *9*, 449-472.

(7) Greer, S. M.; Brodbelt, J. S. Top-Down Characterization of Heavily Modified Histones Using 193 nm Ultraviolet Photodissociation Mass Spectrometry. *J. Proteome Res.* **2018**, *17*, 1138-1145.

(8) Cleland, T. P.; DeHart, C. J.; Fellers, R. T.; VanNispen, A. J.; Greer, J. B.; LeDuc, R. D.; Parker, W. R.; Thomas, P. M.; Kelleher, N. L.; Brodbelt, J. S. High-Throughput Analysis of Intact Human Proteins Using UVPD and HCD on an Orbitrap Mass Spectrometer. *J. Proteome Res.* **2017**, *16*, 2072-2079.

(9) Toby, T. K.; Fornelli, L.; Kelleher, N. L. Progress in Top-Down Proteomics and the Analysis of Proteoforms. *Annual Review of Analytical Chemistry* **2016**, *9*, 499-519.

(10) Leney, A. C.; Heck, A. J. R. Native Mass Spectrometry: What is in the Name? *J. Am. Soc. Mass Spectrom.* **2017**, *28*, 5-13.

(11) Fenn, J.; Mann, M.; Meng, C.; Wong, S.; Whitehouse, C. Electrospray ionization for mass spectrometry of large biomolecules. *Science* **1989**, *246*, 64-71.

(12) Rayleigh, L. XX. On the equilibrium of liquid conducting masses charged with electricity. *The London, Edinburgh, and Dublin Philosophical Magazine and Journal of Science* **1882**, *14*, 184-186.

(13) Smith, J. N.; Flagan, R. C.; Beauchamp, J. L. Droplet Evaporation and Discharge Dynamics in Electrospray Ionization. *J. Phys. Chem. A* **2002**, *106*, 9957-9967.

(14) Kebarle, P.; Verkerk, U. H. Electrospray: From ions in solution to ions in the gas phase, what we know now. *Mass Spectrom. Rev.* **2009**, *28*, 898-917.

(15) Iribarne, J. V.; Thomson, B. A. On the evaporation of small ions from charged droplets. *J. Chem. Phys.* **1976**, *64*, 2287-2294.

(16) Thomson, B. A.; Iribarne, J. V. Field induced ion evaporation from liquid surfaces at atmospheric pressure. *J. Chem. Phys.* **1979**, *71*, 4451-4463.

(17) Gamero-Castaño, M.; Fernandez de la Mora, J. Kinetics of small ion evaporation from the charge and mass distribution of multiply charged clusters in electrosprays. *J. Mass Spectrom.* **2000**, *35*, 790-803.

(18) Loscertales, I. G.; Fernández de la Mora, J. Experiments on the kinetics of field evaporation of small ions from droplets. *J. Chem. Phys.* **1995**, *103*, 5041-5060.

(19) Dole, M.; Mack, L. L.; Hines, R. L.; Mobley, R. C.; Ferguson, L. D.; Alice, M. B. Molecular Beams of Macroions. *J. Chem. Phys.* **1968**, *49*, 2240-2249.

(20) Mack, L. L.; Kralik, P.; Rheude, A.; Dole, M. Molecular Beams of Macroions. II. *J. Chem. Phys.* **1970**, *52*, 4977-4986.

(21) Fernandez de la Mora, J. Electrospray ionization of large multiply charged species proceeds via Dole's charged residue mechanism. *Anal. Chim. Acta* **2000**, *406*, 93-104.

(22) Winger, B. E.; Light-Wahl, K. J.; Ogorzalek Loo, R. R.; Udseth, H. R.; Smith, R. D. Observation and implications of high mass-to-charge ratio ions from electrospray ionization mass spectrometry. *J. Am. Soc. Mass Spectrom.* **1993**, *4*, 536-545.

(23) Kaltashov, I. A.; Mohimen, A. Estimates of Protein Surface Areas in Solution by Electrospray Ionization Mass Spectrometry. *Anal. Chem.* **2005**, *77*, 5370-5379.

(24) McAllister, R. G.; Metwally, H.; Sun, Y.; Konermann, L. Release of Native-like Gaseous Proteins from Electrospray Droplets via the Charged Residue Mechanism: Insights from Molecular Dynamics Simulations. *J. Am. Chem. Soc.* **2015**, *137*, 12667-12676.

(25) Konermann, L.; Rodriguez, A. D.; Liu, J. On the Formation of Highly Charged Gaseous Ions from Unfolded Proteins by Electrospray Ionization. *Anal. Chem.* **2012**, *84*, 6798-6804.

(26) Ahadi, E.; Konermann, L. Modeling the Behavior of Coarse-Grained Polymer Chains in Charged Water Droplets: Implications for the Mechanism of Electrospray Ionization. *J. Phys. Chem. B* **2012**, *116*, 104-112.

(27) Khristenko, N.; Amato, J.; Livet, S.; Pagano, B.; Randazzo, A.; Gabelica, V. Native Ion Mobility Mass Spectrometry: When Gas-Phase Ion Structures Depend on the Electrospray Charging Process. *J. Am. Soc. Mass Spectrom.* **2019**, *30*, 1069-1081.

(28) Natalello, A.; Santambrogio, C.; Grandori, R. Are Charge-State Distributions a Reliable Tool Describing Molecular Ensembles of Intrinsically Disordered Proteins by Native MS? *J. Am. Soc. Mass Spectrom.* **2017**, *28*, 21-28.

(29) Sze, S. K.; Ge, Y.; Oh, H.; McLafferty, F. W. Top-down mass spectrometry of a 29-kDa protein for characterization of any posttranslational modification to within one residue. *Proc. Natl. Acad. Sci. U. S. A.* **2002**, *99*, 1774-1779.

(30) Miladinović, S. M.; Fornelli, L.; Lu, Y.; Piech, K. M.; Girault, H. H.; Tsybin, Y. O. In-Spray Supercharging of Peptides and Proteins in Electrospray Ionization Mass Spectrometry. *Anal. Chem.* **2012**, *84*, 4647-4651.

(31) Meyer, J. G.; Komives, E. A. Charge State Coalescence During Electrospray Ionization Improves Peptide Identification by Tandem Mass Spectrometry. *J. Am. Soc. Mass Spectrom.* **2012**, *23*, 1390-1399.

(32) Kafader, J. O.; Melani, R. D.; Schachner, L. F.; Ives, A. N.; Patrie, S. M.; Kelleher, N. L.; Compton, P. D. Native vs Denatured: An in Depth Investigation of Charge State and Isotope Distributions. *J. Am. Soc. Mass Spectrom.* **2020**, *31*, 574-581.

(33) Testa, L.; Brocca, S.; Santambrogio, C.; D'Urzo, A.; Habchi, J.; Longhi, S.; Uversky, V. N.; Grandori, R. Extracting structural information from charge-state distributions of intrinsically disordered proteins by non-denaturing electrospray-ionization mass spectrometry. *Intrinsically Disord. Proteins* **2013**, *1*, e25068.

(34) Beveridge, R.; Covill, S.; Pacholarz, K. J.; Kalapothakis, J. M. D.; MacPhee, C. E.; Barran, P. E. A Mass-Spectrometry-Based Framework To Define the Extent of Disorder in Proteins. *Anal. Chem.* **2014**, *86*, 10979-10991.

(35) Beveridge, R.; Chappuis, Q.; Macphee, C.; Barran, P. Mass spectrometry methods for intrinsically disordered proteins. *Analyst* **2013**, *138*, 32-42.

(36) Beveridge, R.; Phillips, A. S.; Denbigh, L.; Saleem, H. M.; MacPhee, C. E.; Barran, P. E. Relating gas phase to solution conformations: Lessons from disordered proteins. *PROTEOMICS* **2015**, *15*, 2872-2883.

(37) Zhong, Y.; Han, L.; Ruotolo, B. T. Collisional and Coulombic Unfolding of Gas-Phase Proteins: High Correlation to Their Domain Structures in Solution. *Angew. Chem., Int. Ed.* **2014**, *53*, 9209-9212.

(38) Pagel, K.; Hyung, S.-J.; Ruotolo, B. T.; Robinson, C. V. Alternate Dissociation Pathways Identified in Charge-Reduced Protein Complex Ions. *Anal. Chem.* **2010**, *82*, 5363-5372.

(39) Townsend, J. A.; Keener, J. E.; Miller, Z. M.; Prell, J. S.; Marty, M. T. Imidazole Derivatives Improve Charge Reduction and Stabilization for Native Mass Spectrometry. *Anal. Chem.* **2019**, *91*, 14765-14772.

(40) Zhou, M.; Dagan, S.; Wysocki, V. H. Impact of charge state on gas-phase behaviors of noncovalent protein complexes in collision induced dissociation and surface induced dissociation. *Analyst* **2013**, *138*, 1353-1362.

(41) Bornschein, R. E.; Ruotolo, B. T. Ion mobility-mass spectrometry of charge-reduced protein complexes reveals general trends in the collisional ejection of compact subunits. *Analyst* **2015**, *140*, 7020-7029.

(42) Zhou, M.; Dagan, S.; Wysocki, V. H. Protein Subunits Released by Surface Collisions of Noncovalent Complexes: Nativelike Compact Structures Revealed by Ion Mobility Mass Spectrometry. *Angew. Chem., Int. Ed.* **2012**, *51*, 4336-4339.

(43) Iavarone, A. T.; Williams, E. R. Mechanism of Charging and Supercharging Molecules in Electrospray Ionization. *J. Am. Chem. Soc.* **2003**, *125*, 2319-2327.

(44) Sterling, H. J.; Prell, J. S.; Cassou, C. A.; Williams, E. R. Protein Conformation and Supercharging with DMSO from Aqueous Solution. *J. Am. Soc. Mass Spectrom.* **2011**, *22*, 1178-1186.

(45) Lomeli, S. H.; Peng, I. X.; Yin, S.; Ogorzalek Loo, R. R.; Loo, J. A. New reagents for increasing ESI multiple charging of proteins and protein complexes. *J. Am. Soc. Mass Spectrom.* **2010**, *21*, 127-131.

(46) Valeja, S. G.; Tipton, J. D.; Emmett, M. R.; Marshall, A. G. New Reagents for Enhanced Liquid Chromatographic Separation and Charging of Intact Protein Ions for Electrospray Ionization Mass Spectrometry. *Anal. Chem.* **2010**, *82*, 7515-7519.

(47) Zenaidee, M. A.; Leeming, M. G.; Zhang, F.; Funston, T. T.; Donald, W. A. Highly Charged Protein Ions: The Strongest Organic Acids to Date. *Angew. Chem., Int. Ed.* **2017**, *56*, 8522-8526.

(48) Zenaidee, M. A.; Donald, W. A. Extremely supercharged proteins in mass spectrometry: profiling the pH of electrospray generated droplets, narrowing charge state distributions, and increasing ion fragmentation. *Analyst* **2015**, *140*, 1894-1905.

(49) Cassou, C. A.; Williams, E. R. Desalting protein ions in native mass spectrometry using supercharging reagents. *Analyst* **2014**, *139*, 4810-4819.

(50) Teo, C. A.; Donald, W. A. Solution Additives for Supercharging Proteins beyond the Theoretical Maximum Proton-Transfer Limit in Electrospray Ionization Mass Spectrometry. *Anal. Chem.* **2014**, *86*, 4455-4462.

(51) Zenaidee, M. A.; Donald, W. A. Electron capture dissociation of extremely supercharged protein ions formed by electrospray ionisation. *Anal. Methods* **2015**, *7*, 7132-7139.

(52) Sterling, H. J.; Williams, E. R. Real-Time Hydrogen/Deuterium Exchange Kinetics via Supercharged Electrospray Ionization Tandem Mass Spectrometry. *Anal. Chem.* **2010**, *82*, 9050-9057.

(53) Ogorzalek Loo, R. R.; Lakshmanan, R.; Loo, J. A. What Protein Charging (and Supercharging) Reveal about the Mechanism of Electrospray Ionization. *J. Am. Soc. Mass Spectrom.* **2014**, *25*, 1675-1693.

(54) Metwally, H.; McAllister, R. G.; Popa, V.; Konermann, L. Mechanism of Protein Supercharging by Sulfolane and m-Nitrobenzyl Alcohol: Molecular Dynamics Simulations of the Electrospray Process. *Anal. Chem.* **2016**, *88*, 5345-5354.

(55) Sterling, H. J.; Williams, E. R. Origin of supercharging in electrospray ionization of noncovalent complexes from aqueous solution. *J. Am. Soc. Mass Spectrom.* **2009**, *20*, 1933-1943.

(56) Sterling, H. J.; Kintzer, A. F.; Feld, G. K.; Cassou, C. A.; Krantz, B. A.; Williams, E. R. Supercharging Protein Complexes from Aqueous Solution Disrupts their Native Conformations. *J. Am. Soc. Mass Spectrom.* **2012**, *23*, 191-200.

(57) Sterling, H. J.; Daly, M. P.; Feld, G. K.; Thoren, K. L.; Kintzer, A. F.; Krantz, B. A.; Williams, E. R. Effects of supercharging reagents on noncovalent complex structure in electrospray ionization from aqueous solutions. *J. Am. Soc. Mass Spectrom.* **2010**, *21*, 1762-1774.

(58) Sterling, H. J.; Cassou, C. A.; Trnka, M. J.; Burlingame, A. L.; Krantz, B. A.; Williams, E. R. The role of conformational flexibility on protein supercharging in native electrospray ionization. *Phys. Chem. Chem. Phys.* **2011**, *13*, 18288-18296.

(59) Gabelica, V.; Marklund, E. Fundamentals of ion mobility spectrometry. *Curr. Opin. Chem. Biol.* **2018**, *42*, 51-59.

(60) Giles, K.; Pringle, S. D.; Worthington, K. R.; Little, D.; Wildgoose, J. L.; Bateman, R. H. Applications of a travelling wave-based radio-frequency-only stacked ring ion guide. *Rapid Commun. Mass Spectrom.* **2004**, *18*, 2401-2414.

(61) Shvartsburg, A. A.; Smith, R. D. Fundamentals of Traveling Wave Ion Mobility Spectrometry. *Anal. Chem.* **2008**, *80*, 9689-9699.

(62) Wojcik, R.; Nagy, G.; Attah, I. K.; Webb, I. K.; Garimella, S. V. B.; Weitz, K. K.; Hollerbach, A.; Monroe, M. E.; Ligare, M. R.; Nielson, F. F.; Norheim, R. V.; Renslow, R. S.; Metz, T. O.; Ibrahim, Y. M.; Smith, R. D. SLIM Ultrahigh Resolution Ion Mobility Spectrometry Separations of Isotopologues and Isotopomers Reveal Mobility Shifts due to Mass Distribution Changes. *Anal. Chem.* **2019**, *91*, 11952-11962.

(63) Shvartsburg, A. A.; Jarrold, M. F. An exact hard-spheres scattering model for the mobilities of polyatomic ions. *Chem. Phys. Lett.* **1996**, *261*, 86-91.

(64) Ewing, S. A.; Donor, M. T.; Wilson, J. W.; Prell, J. S. Collidoscope: An Improved Tool for Computing Collisional Cross-Sections with the Trajectory Method. *J. Am. Soc. Mass Spectrom.* **2017**, *28*, 587-596.

(65) Larriba, C.; Hogan, C. J. Ion Mobilities in Diatomic Gases: Measurement versus Prediction with Non-Specular Scattering Models. *J. Phys. Chem. A* **2013**, *117*, 3887-3901.

(66) Rolland, A. D.; Prell, J. S. Computational Insights into Compaction of Gas-Phase Protein and Protein Complex Ions in Native Ion Mobility-Mass Spectrometry. *Trends Anal. Chem.* **2019**, *116*, 282-291.

(67) Bleiholder, C.; Dupuis, N. F.; Wyttenbach, T.; Bowers, M. T. Ion mobility–mass spectrometry reveals a conformational conversion from random assembly to β-sheet in amyloid fibril formation. *Nat. Chem.* **2011**, *3*, 172-177.

(68) Koeniger, S. L.; Clemmer, D. E. Resolution and structural transitions of elongated states of ubiquitin. *J. Am. Soc. Mass Spectrom.* **2007**, *18*, 322-331.

(69) Silveira, J. A.; Fort, K. L.; Kim, D.; Servage, K. A.; Pierson, N. A.; Clemmer, D. E.; Russell, D. H. From Solution to the Gas Phase: Stepwise Dehydration and Kinetic Trapping of Substance P Reveals the Origin of Peptide Conformations. *J. Am. Chem. Soc.* **2013**, *135*, 19147-19153.

(70) Bleiholder, C.; Liu, F. C. Structure Relaxation Approximation (SRA) for Elucidation of Protein Structures from Ion Mobility Measurements. *J. Phys. Chem. B* **2019**, *123*, 2756-2769.

(71) Seo, J.; Hoffmann, W.; Warnke, S.; Bowers, M. T.; Pagel, K.; von Helden, G. Retention of Native Protein Structures in the Absence of Solvent: A Coupled Ion Mobility and Spectroscopic Study. *Angew. Chem., Int. Ed.* **2016**, *55*, 14173-14176.

(72) Warnke, S.; Ben Faleh, A.; Pellegrinelli, R. P.; Yalovenko, N.; Rizzo, T. R. Combining ultra-high resolution ion mobility spectrometry with cryogenic IR spectroscopy for the study of biomolecular ions. *Faraday Discussions* **2019**, *217*, 114-125.

(73) Pukala, T. L.; Ruotolo, B. T.; Zhou, M.; Politis, A.; Stefanescu, R.; Leary, J. A.; Robinson, C. V. Subunit Architecture of Multiprotein Assemblies Determined Using Restraints from Gas-Phase Measurements. *Structure* **2009**, *17*, 1235-1243.

(74) Eschweiler, J. D.; Farrugia, M. A.; Dixit, S. M.; Hausinger, R. P.; Ruotolo, B. T. A Structural Model of the Urease Activation Complex Derived from Ion Mobility-Mass Spectrometry and Integrative Modeling. *Structure* **2018**, *26*, 599-606.e593.

(75) Seffernick, J. T.; Harvey, S. R.; Wysocki, V. H.; Lindert, S. Predicting Protein Complex Structure from Surface-Induced Dissociation Mass Spectrometry Data. *ACS Cent. Sci.* **2019**, *5*, 1330-1341.

(76) Marklund, Erik G.; Degiacomi, Matteo T.; Robinson, Carol V.; Baldwin, Andrew J.; Benesch, Justin L. P. Collision Cross Sections for Structural Proteomics. *Structure* **2015**, *23*, 791-799.

(77) Bush, M. F.; Hall, Z.; Giles, K.; Hoyes, J.; Robinson, C. V.; Ruotolo, B. T. Collision Cross Sections of Proteins and Their Complexes: A Calibration Framework and Database for Gas-Phase Structural Biology. *Anal. Chem.* **2010**, *82*, 9557-9565.

(78) Testa, L.; Brocca, S.; Grandori, R. Charge-Surface Correlation in Electrospray Ionization of Folded and Unfolded Proteins. *Anal. Chem.* **2011**, *83*, 6459-6463.

(79) Hogan, C. J.; Carroll, J. A.; Rohrs, H. W.; Biswas, P.; Gross, M. L. Combined Charged Residue-Field Emission Model of Macromolecular Electrospray Ionization. *Anal. Chem.* **2009**, *81*, 369-377.

(80) Chen, X.; Raab, S. A.; Poe, T.; Clemmer, D. E.; Larriba-Andaluz, C. Determination of Gas-Phase Ion Structures of Locally Polar Homopolymers Through High-Resolution Ion Mobility Spectrometry–Mass Spectrometry. *J. Am. Soc. Mass Spectrom.* **2019**, *30*, 905-918.

(81) Trimpin, S.; Plasencia, M.; Isailovic, D.; Clemmer, D. E. Resolving Oligomers from Fully Grown Polymers with IMS−MS. *Anal. Chem.* **2007**, *79*, 7965-7974.

(82) Larriba, C.; Fernandez de la Mora, J. The Gas Phase Structure of Coulombically Stretched Polyethylene Glycol Ions. *J. Phys. Chem. B* **2012**, *116*, 593-598.

(83) Haler, J. R. N.; Morsa, D.; Lecomte, P.; Jérôme, C.; Far, J.; De Pauw, E. Predicting Ion Mobility-Mass Spectrometry trends of polymers using the concept of apparent densities. *Methods* **2018**, *144*, 125-133.

(84) Robinson, C. V.; Sali, A.; Baumeister, W. The molecular sociology of the cell. *Nature* **2007**, *450*, 973-982.

(85) Dixit, S. M.; Polasky, D. A.; Ruotolo, B. T. Collision induced unfolding of isolated proteins in the gas phase: past, present, and future. *Curr. Opin. Chem. Biol.* **2018**, *42*, 93-100.

(86) Benesch, J. L. P.; Aquilina, J. A.; Ruotolo, B. T.; Sobott, F.; Robinson, C. V. Tandem Mass Spectrometry Reveals the Quaternary Organization of Macromolecular Assemblies. *Chem. Biol.* **2006**, *13*, 597-605.

(87) Clemmer, D. E.; Russell, D. H.; Williams, E. R. Characterizing the Conformationome: Toward a Structural Understanding of the Proteome. *Acc. Chem. Res.* **2017**, *50*, 556-560.

(88) Wyttenbach, T.; Bowers, M. T. Structural Stability from Solution to the Gas Phase: Native Solution Structure of Ubiquitin Survives Analysis in a Solvent-Free Ion Mobility–Mass Spectrometry Environment. *J. Phys. Chem. B* **2011**, *115*, 12266-12275.

(89) Gologan, B.; Takáts, Z.; Alvarez, J.; Wiseman, J. M.; Talaty, N.; Ouyang, Z.; Cooks, R. G. Ion soft-landing into liquids: Protein identification, separation, and purification with retention of biological activity. *J. Am. Soc. Mass Spectrom.* **2004**, *15*, 1874-1884.

(90) Eschweiler, J. D.; Martini, R. M.; Ruotolo, B. T. Chemical Probes and Engineered Constructs Reveal a Detailed Unfolding Mechanism for a Solvent-Free Multidomain Protein. *J. Am. Chem. Soc.* **2017**, *139*, 534-540.

(91) McLuckey, S. A. Principles of collisional activation in analytical mass spectrometry. *J. Am. Soc. Mass Spectrom.* **1992**, *3*, 599-614.

(92) Zubarev, R. A. Electron-capture dissociation tandem mass spectrometry. *Curr. Opin. Biotechnol.* **2004**, *15*, 12-16.

(93) Syka, J. E. P.; Coon, J. J.; Schroeder, M. J.; Shabanowitz, J.; Hunt, D. F. Peptide and protein sequence analysis by electron transfer dissociation mass spectrometry. *Proc. Natl. Acad. Sci. U. S. A.* **2004**, *101*, 9528-9533.

(94) Brodbelt, J. S.; Wilson, J. J. Infrared multiphoton dissociation in quadrupole ion traps. *Mass Spectrom. Rev.* **2009**, *28*, 390-424.

(95) Brodbelt, J. S. Photodissociation mass spectrometry: new tools for characterization of biological molecules. *Chem. Soc. Rev.* **2014**, *43*, 2757-2783.

(96) McLuckey, S. A.; Goeringer, D. E. Slow Heating Methods in Tandem Mass Spectrometry. *J. Mass Spectrom.* **1997**, *32*, 461-474.

(97) Tian, Y.; Han, L.; Buckner, A. C.; Ruotolo, B. T. Collision Induced Unfolding of Intact Antibodies: Rapid Characterization of Disulfide Bonding Patterns, Glycosylation, and Structures. *Anal. Chem.* **2015**, *87*, 11509-11515.

(98) Tian, Y.; Lippens, J. L.; Netirojjanakul, C.; Campuzano, I. D. G.; Ruotolo, B. T. Quantitative collision-induced unfolding differentiates model antibody–drug conjugates. *Protein Sci.* **2019**, *28*, 598-608.

(99) Hyung, S.-J.; Robinson, C. V.; Ruotolo, B. T. Gas-Phase Unfolding and Disassembly Reveals Stability Differences in Ligand-Bound Multiprotein Complexes. *Chem. Biol.* **2009**, *16*, 382-390.

(100) Rabuck-Gibbons, J. N.; Keating, J. E.; Ruotolo, B. T. Collision induced unfolding and dissociation differentiates ATP-competitive from allosteric protein tyrosine kinase inhibitors. *Int. J. Mass Spectrom.* **2018**, *427*, 151-156.

(101) Niu, S.; Ruotolo, B. T. Collisional unfolding of multiprotein complexes reveals cooperative stabilization upon ligand binding. *Protein Sci* **2015**, *24*, 1272-1281.

(102) Jurchen, J. C.; Williams, E. R. Origin of Asymmetric Charge Partitioning in the Dissociation of Gas-Phase Protein Homodimers. *J. Am. Chem. Soc.* **2003**, *125*, 2817-2826.

(103) Wysocki, V. H.; Joyce, K. E.; Jones, C. M.; Beardsley, R. L. Surface-Induced Dissociation of Small Molecules, Peptides, and Non-covalent Protein Complexes. *J. Am. Soc. Mass Spectrom.* **2008**, *19*, 190-208.

(104) Zhou, M.; Wysocki, V. H. Surface Induced Dissociation: Dissecting Noncovalent Protein Complexes in the Gas phase. *Acc. Chem. Res.* **2014**, *47*, 1010-1018.

(105) Jones, C. M.; Beardsley, R. L.; Galhena, A. S.; Dagan, S.; Cheng, G.; Wysocki, V. H. Symmetrical Gas-Phase Dissociation of Noncovalent Protein Complexes via Surface Collisions. *J. Am. Chem. Soc.* **2006**, *128*, 15044-15045.

(106) Quintyn, R. S.; Yan, J.; Wysocki, V. H. Surface-Induced Dissociation of Homotetramers with D2 Symmetry Yields their Assembly Pathways and Characterizes the Effect of Ligand Binding. *Chem. Biol.* **2015**, *22*, 583-592.

(107) Harvey, S. R.; Seffernick, J. T.; Quintyn, R. S.; Song, Y.; Ju, Y.; Yan, J.; Sahasrabuddhe, A. N.; Norris, A.; Zhou, M.; Behrman, E. J.; Lindert, S.; Wysocki, V. H. Relative interfacial cleavage energetics of protein complexes revealed by surface collisions. *Proc. Natl. Acad. Sci. U. S. A.* **2019**, *116*, 8143-8148.

(108) Zhou, M.; Jones, C. M.; Wysocki, V. H. Dissecting the Large Noncovalent Protein Complex GroEL with Surface-Induced Dissociation and Ion Mobility–Mass Spectrometry. *Anal. Chem.* **2013**, *85*, 8262-8267.

(109) Song, Y.; Nelp, M. T.; Bandarian, V.; Wysocki, V. H. Refining the Structural Model of a Heterohexameric Protein Complex: Surface Induced Dissociation and Ion Mobility Provide Key Connectivity and Topology Information. *ACS Cent. Sci.* **2015**, *1*, 477-487.

(110) Ma, X.; Zhou, M.; Wysocki, V. H. Surface Induced Dissociation Yields Quaternary Substructure of Refractory Noncovalent Phosphorylase B and Glutamate Dehydrogenase Complexes. *J. Am. Soc. Mass Spectrom.* **2014**, *25*, 368-379.

(111) Ma, X.; Loo, J. A.; Wysocki, V. H. Surface induced dissociation yields substructure of Methanosarcina thermophila 20S proteasome complexes. *Int. J. Mass Spectrom.* **2015**, *377*, 201-204.

(112) Harvey, S. R.; Liu, Y.; Liu, W.; Wysocki, V. H.; Laganowsky, A. Surface induced dissociation as a tool to study membrane protein complexes. *Chem. Commun.* **2017**, *53*, 3106-3109.

(113) Sipe, S. N.; Brodbelt, J. S. Impact of charge state on 193 nm ultraviolet photodissociation of protein complexes. *Phys. Chem. Chem. Phys.* **2019**, *21*, 9265-9276.

(114) Dunbar, R. C. BIRD (blackbody infrared radiative dissociation): Evolution, principles, and applications. *Mass Spectrom. Rev.* **2004**, *23*, 127-158.

(115) Dunbar, R. C.; McMahon, T. B.; Thoelmann, D.; Tonner, D. S.; Salahub, D. R.; Wei, D. Zero-Pressure Thermal-Radiation-Induced Dissociation of Gas-Phase Cluster Ions: Comparison of Theory and Experiment for (H2O)2Cl- and (H2O)3Cl. *J. Am. Chem. Soc.* **1995**, *117*, 12819-12825.

(116) Price, W. D.; Schnier, P. D.; Williams, E. R. Binding Energies of the Proton-Bound Amino Acid Dimers Gly·Gly, Ala·Ala, Gly·Ala, and Lys·Lys Measured by Blackbody Infrared Radiative Dissociation. *J. Phys. Chem. B* **1997**, *101*, 664-673.

(117) Schnier, P. D.; Price, W. D.; Strittmatter, E. F.; Williams, E. R. Dissociation energetics and mechanisms of leucine enkephalin (M+H)+ and (2M+X)+ ions (X=H, Li, Na, K, and Rb) measured by blackbody infrared radiative dissociation. *J. Am. Soc. Mass Spectrom.* **1997**, *8*, 771-780.

(118) Schnier, P. D.; Price, W. D.; Jockusch, R. A.; Williams, E. R. Blackbody Infrared Radiative Dissociation of Bradykinin and Its Analogues: Energetics, Dynamics, and Evidence for Salt-Bridge Structures in the Gas Phase. *J. Am. Chem. Soc.* **1996**, *118*, 7178-7189.

(119) Price, W. D.; Schnier, P. D.; Williams, E. R. Tandem Mass Spectrometry of Large Biomolecule Ions by Blackbody Infrared Radiative Dissociation. *Anal. Chem.* **1996**, *68*, 859-866.

(120) Gross, D. S.; Zhao, Y.; Williams, E. R. Dissociation of heme-globin complexes by blackbody infrared radiative dissociation: Molecular specificity in the gas phase? *J. Am. Soc. Mass Spectrom.* **1997**, *8*, 519-524.

(121) Sinelnikov, I.; Kitova, E. N.; Klassen, J. S. Influence of coulombic repulsion on the dissociation pathways and energetics of multiprotein complexes in the gas phase. *J. Am. Soc. Mass Spectrom.* **2007**, *18*, 617-631.

(122) Price, W. D.; Williams, E. R. Activation of Peptide Ions by Blackbody Radiation: Factors That Lead to Dissociation Kinetics in the Rapid Energy Exchange Limit. *J. Phys. Chem. A* **1997**, *101*, 8844-8852.

(123) Price, W. D.; Schnier, P. D.; Jockusch, R. A.; Strittmatter, E. F.; Williams, E. R. Unimolecular Reaction Kinetics in the High-Pressure Limit without Collisions. *J. Am. Chem. Soc.* **1996**, *118*, 10640-10644.

(124) Schnier, P. D.; Jurchen, J. C.; Williams, E. R. The Effective Temperature of Peptide Ions Dissociated by Sustained Off-Resonance Irradiation Collisional Activation in Fourier Transform Mass Spectrometry. *J. Phys. Chem. B* **1999**, *103*, 737-745.

(125) Laskin, J.; Futrell, J. Internal Energy Distributions Resulting from Sustained Off-Resonance Excitation in Fourier Transform Ion Cyclotron Resonance Mass Spectrometry. II. Fragmentation of the 1-Bromonaphthalene Radical Cation. *J. Phys. Chem. A* **2000**, *104*, 5484-5494.

(126) Laskin, J.; Denisov, E.; Futrell, J. Comparative Study of Collision-Induced and Surface-Induced Dissociation. 2. Fragmentation of Small Alanine-Containing Peptides in FT-ICR MS. *J. Phys. Chem. B* **2001**, *105*, 1895-1900.

(127) Laskin, J.; Denisov, E.; Futrell, J. A Comparative Study of Collision-Induced and Surface-Induced Dissociation. 1. Fragmentation of Protonated Dialanine. *J. Am. Chem. Soc.* **2000**, *122*, 9703-9714.

(128) Laskin, J.; Byrd, M.; Futrell, J. Internal energy distributions resulting from sustained off-resonance excitation in FTMS. I. Fragmentation of the bromobenzene radical cation. *Int. J. Mass Spectrom.* **2000**, *195-196*, 285-302.

(129) Rakov, V. S.; Denisov, E. V.; Laskin, J.; Futrell, J. H. Surface-Induced Dissociation of the Benzene Molecular Cation in Fourier Transform Ion Cyclotron Resonance Mass Spectrometry. *J. Phys. Chem. A* **2002**, *106*, 2781-2788.

(130) Laskin, J.; Futrell, J. H. Surface-induced dissociation of peptide ions: Kinetics and dynamics. *J. Am. Soc. Mass Spectrom.* **2003**, *14*, 1340-1347.

(131) Armentrout, P. B. Threshold Collision-Induced Dissociations for the Determination of Accurate Gas-Phase Binding Energies and Reaction Barriers. In *Modern Mass Spectrometry*, Schalley, C. A., Ed.; Springer Berlin Heidelberg: Berlin, Heidelberg, 2003, pp 233-262.

(132) Rezaee, M.; McNary, C. P.; Armentrout, P. B. Threshold collision-induced dissociation and theoretical study of protonated azobenzene. *J. Chem. Phys.* **2017**, *147*, 164308.

(133) Rodgers, M. T.; Armentrout, P. B. Noncovalent metal–ligand bond energies as studied by threshold collision-induced dissociation. *Mass Spectrom. Rev.* **2000**, *19*, 215-247.

(134) McNary, C. P.; Armentrout, P. B. Threshold Collision-Induced Dissociation of Proton-Bound Hydrazine and Dimethylhydrazine Clusters. *J. Phys. Chem. A* **2016**, *120*, 9690-9701.

(135) Mookherjee, A.; Van Stipdonk, M. J.; Armentrout, P. B. Thermodynamics and Reaction Mechanisms of Decomposition of the Simplest Protonated Tripeptide, Triglycine: A Guided Ion Beam and Computational Study. *J. Am. Soc. Mass Spectrom.* **2017**, *28*, 739-757.

(136) Mirza, U. A.; Cohen, S. L.; Chait, B. T. Heat-induced conformational changes in proteins studied by electrospray ionization mass spectrometry. *Anal. Chem.* **1993**, *65*, 1-6.

(137) Benesch, J. L. P.; Sobott, F.; Robinson, C. V. Thermal Dissociation of Multimeric Protein Complexes by Using Nanoelectrospray Mass Spectrometry. *Anal. Chem.* **2003**, *75*, 2208-2214.

(138) Li, G.; Zheng, S.; Chen, Y.; Hou, Z.; Huang, G. Reliable Tracking In-Solution Protein Unfolding via Ultrafast Thermal Unfolding/Ion Mobility-Mass Spectrometry. *Anal. Chem.* **2018**, *90*, 7997-8001.

(139) El-Baba, T. J.; Woodall, D. W.; Raab, S. A.; Fuller, D. R.; Laganowsky, A.; Russell, D. H.; Clemmer, D. E. Melting Proteins: Evidence for Multiple Stable Structures upon Thermal Denaturation of Native Ubiquitin from Ion Mobility Spectrometry-Mass Spectrometry Measurements. *J. Am. Chem. Soc.* **2017**, *139*, 6306-6309.

(140) Woodall, D. W.; El-Baba, T. J.; Fuller, D. R.; Liu, W.; Brown, C. J.; Laganowsky, A.; Russell, D. H.; Clemmer, D. E. Variable-Temperature ESI-IMS-MS Analysis of Myohemerythrin Reveals Ligand Losses, Unfolding, and a Non-Native Disulfide Bond. *Anal. Chem.* **2019**, *91*, 6808-6814.

(141) Brown, C. J.; Woodall, D. W.; El-Baba, T. J.; Clemmer, D. E. Characterizing Thermal Transitions of IgG with Mass Spectrometry. *J. Am. Soc. Mass Spectrom.* **2019**, *30*, 2438-2445.

(142) El-Baba, T. J.; Clemmer, D. E. Solution thermochemistry of concanavalin A tetramer conformers measured by variable-temperature ESI-IMS-MS. *Int. J. Mass Spectrom.* **2019**, *443*, 93-100.

(143) Marchand, A.; Rosu, F.; Zenobi, R.; Gabelica, V. Thermal Denaturation of DNA G-Quadruplexes and Their Complexes with Ligands: Thermodynamic Analysis of the Multiple States Revealed by Mass Spectrometry. *J. Am. Chem. Soc.* **2018**, *140*, 12553-12565.

(144) Benesch, J. L. P.; Ruotolo, B. T. Mass Spectrometry: Come of Age for Structural and Dynamical Biology. *Curr. Opin. Struct. Biol.* **2011**, *21*, 641-649.

(145) Benesch, J. L. P.; Ruotolo, B. T.; Simmons, D. A.; Robinson, C. V. Protein Complexes in the Gas Phase: Technology for Structural Genomics and Proteomics. *Chem. Rev.* **2007**, *107*, 3544-3567.

(146) Baldwin, A. J.; Lioe, H.; Robinson, C. V.; Kay, L. E.; Benesch, J. L. P. αB-Crystallin Polydispersity Is a Consequence of Unbiased Quaternary Dynamics. *J. Mol. Biol.* **2011**, *413*, 297-309.

(147) Kintzer, A. F.; Thoren, K. L.; Sterling, H. J.; Dong, K. C.; Feld, G. K.; Tang, I. I.; Zhang, T. T.; Williams, E. R.; Berger, J. M.; Krantz, B. A. The Protective Antigen Component of Anthrax Toxin Forms Functional Octameric Complexes. *J. Mol. Biol.* **2009**, *392*, 614-629.

(148) Uetrecht, C.; Versluis, C.; Watts, N. R.; Roos, W. H.; Wuite, G. J. L.; Wingfield, P. T.; Steven, A. C.; Heck, A. J. R. High-resolution mass spectrometry of viral assemblies: Molecular composition and stability of dimorphic hepatitis B virus capsids. *Proc. Natl. Acad. Sci. U. S. A.* **2008**, *105*, 9216-9220.

(149) Xie, Y.; Zhang, J.; Yin, S.; Loo, J. A. Top-Down ESI-ECD-FT-ICR Mass Spectrometry Localizes Noncovalent Protein-Ligand Binding Sites. *J. Am. Chem. Soc.* **2006**, *128*, 14432-14433.

(150) Loo, J. A. Electrospray Ionization Mass Spectrometry: a Technology for Studying Noncovalent Macromolecular Complexes. *Int. J. Mass Spectrom.* **2000**, *200*, 175-186.

(151) Robinson, C. V.; Chung, E. W.; Kragelund, B. B.; Knudsen, J.; Aplin, R. T.; Poulsen, F. M.; Dobson, C. M. Probing the Nature of Noncovalent Interactions by Mass Spectrometry. A Study of Protein−CoA Ligand Binding and Assembly. *J. Am. Chem. Soc.* **1996**, *118*, 8646-8653.

(152) Loo, J. A.; Holsworth, D. D.; Root-Bernstein, R. S. Use of electrospray ionization mass spectrometry to probe antisense peptide interactions. *Biol. Mass Spectrom.* **1994**, *23*, 6-12.

(153) Uetrecht, C.; Barbu, I. M.; Shoemaker, G. K.; van Duijn, E.; Heck, A. J. R. Interrogating Viral Capsid Assembly with Ion Mobility–Mass Spectrometry. *Nat. Chem.* **2011**, *3*, 126-132.

(154) Scarff, C. A.; Thalassinos, K.; Hilton, G. R.; Scrivens, J. H. Travelling wave ion mobility mass spectrometry studies of protein structure: biological significance and comparison with X-ray crystallography and nuclear magnetic resonance spectroscopy measurements. *Rapid Commun. Mass Spectrom.* **2008**, *22*, 3297-3304.

(155) Hall, Z.; Politis, A.; Bush, M. F.; Smith, L. J.; Robinson, C. V. Charge-State Dependent Compaction and Dissociation of Protein Complexes: Insights from Ion Mobility and Molecular Dynamics. *J. Am. Chem. Soc.* **2012**, *134*, 3429-3438.

(156) Verkerk, U. H.; Peschke, M.; Kebarle, P. Effect of buffer cations and of H3O+ on the charge states of native proteins. Significance to determinations of stability constants of protein complexes. *J. Mass Spectrom.* **2003**, *38*, 618-631.

(157) Lemaire, D.; Marie, G.; Serani, L.; Laprévote, O. Stabilization of Gas-Phase Noncovalent Macromolecular Complexes in Electrospray Mass Spectrometry Using Aqueous Triethylammonium Bicarbonate Buffer. *Anal. Chem.* **2001**, *73*, 1699-1706.

(158) Catalina, M. I.; van den Heuvel, R. H. H.; van Duijn, E.; Heck, A. J. R. Decharging of Globular Proteins and Protein Complexes in Electrospray. *Chem. - Eur. J.* **2005**, *11*, 960-968.

(159) Sterling, H. J.; Cassou, C. A.; Susa, A. C.; Williams, E. R. Electrothermal Supercharging of Proteins in Native Electrospray Ionization. *Anal. Chem.* **2012**, *84*, 3795-3801.

(160) Yue, X.; Vahidi, S.; Konermann, L. Insights into the Mechanism of Protein Electrospray Ionization From Salt Adduction Measurements. *J. Am. Soc. Mass Spectrom.* **2014**, *25*, 1322-1331.

(161) Ruotolo, B. T.; Benesch, J. L. P.; Sandercock, A. M.; Hyung, S.-J.; Robinson, C. V. Ion Mobility-Mass Spectrometry Analysis of Large Protein Complexes. *Nat. Protoc.* **2008**, *3*, 1139-1152.

(162) Nesatyy, V. J.; Suter, M. J. F. On the conformation-dependent neutralization theory and charging of individual proteins and their non-covalent complexes in the gas phase. *J. Mass Spectrom.* **2004**, *39*, 93-97.

(163) Heck, A. J. R.; van den Heuvel, R. H. H. Investigation of Intact Protein Complexes by Mass Spectrometry. *Mass Spectrom. Rev.* **2004**, *23*, 368-389.

(164) Tolić, L. P.; Anderson, G. A.; Smith, R. D.; Brothers, H. M.; Spindler, R.; Tomalia, D. A. Electrospray ionization Fourier transform ion cyclotron resonance mass spectrometric characterization of high molecular mass Starburst™ dendrimers. *Int. J. Mass Spectrom. Ion Processes* **1997**, *165*, 405-418.

(165) Going, C. C.; Williams, E. R. Supercharging with m-Nitrobenzyl Alcohol and Propylene Carbonate: Forming Highly Charged Ions with Extended, Near-Linear Conformations. *Anal. Chem.* **2015**, *87*, 3973-3980.

(166) Donald, W. A.; McKenzie, C. J.; O'Hair, R. A. J. C-H Bond Activation of Methanol and Ethanol by a High-Spin $Fe^{IV}O$ Biomimetic Complex. *Angew. Chem., Int. Ed.* **2011**, *50*, 8379-8383.

(167) Donald, W. A.; O'Hair, R. A. J. Shapeshifting: Ligation by 1, 4-cyclohexadiene induces a structural change in Ag^{5+}. *Dalton Trans.* **2012**, *41*, 3185-3193.

(168) Donald, W. A.; Khairallah, G. N.; O'Hair, R. A. J. The effective temperature of ions stored in a linear quadrupole ion trap mass spectrometer. *J. Am. Soc. Mass Spectrom.* **2013**, *24*, 811-815.

(169) Schnier, P. D.; Gross, D. S.; Williams, E. R. Electrostatic Forces and Dielectric Polarizability of Multiply Protonated Gas-Phase Cytochrome c Ions Probed by Ion/Molecule Chemistry. *J. Am. Chem. Soc.* **1995**, *117*, 6747-6757.

(170) Williams, E. R. Proton transfer reactivity of large multiply charged ions. *J. Mass Spectrom.* **1996**, *31*, 831-842.

(171) Hanwell, M. D.; Curtis, D. E.; Lonie, D. C.; Vandermeersch, T.; Zurek, E.; Hutchison, G. R. Avogadro: an advanced semantic chemical editor, visualization, and analysis platform. *J. Cheminf.* **2012**, *4*, 17.

(172) Marchese, R.; Grandori, R.; Carloni, P.; Raugei, S. On the Zwitterionic Nature of Gas-Phase Peptides and Protein Ions. *PLoS Comput. Biol.* **2010**, *6*, e1000775.

(173) Popa, V.; Trecroce, D. A.; McAllister, R. G.; Konermann, L. Collision-Induced Dissociation of Electrosprayed Protein Complexes: An All-Atom Molecular Dynamics Model with Mobile Protons. *J. Phys. Chem. B* **2016**, *120*, 5114-5124.

(174) Wilkinson, K. D.; Mayer, A. N. Alcohol-induced conformational changes of ubiquitin. *Arch. Biochem. Biophys.* **1986**, *250*, 390-399.

(175) Schnier, P. D.; Gross, D. S.; Williams, E. R. On the maximum charge state and proton transfer reactivity of peptide and protein ions formed by electrospray ionization. *J. Am. Soc. Mass Spectrom.* **1995**, *6*, 1086-1097.

(176) Qi, X. L.; Holt, C.; McNulty, D.; Clarke, D. T.; Brownlow, S.; Jones, G. R. Effect of temperature on the secondary structure of beta-lactoglobulin at pH 6.7, as determined by CD and IR spectroscopy: a test of the molten globule hypothesis. *Biochem. J.* **1997**, *324*, 341-346.

(177) Suzukida, M.; Le, H. P.; Shahid, F.; McPherson, R. A.; Birnbaum, E. R.; Darnall, D. W. Resonance energy transfer between cysteine-34 and tryptophan-214 in human serum albumin. Distance measurements as a function of pH. *Biochemistry* **1983**, *22*, 2415-2420.

(178) El Kadi, N.; Taulier, N.; Le Huérou, J. Y.; Gindre, M.; Urbach, W.; Nwigwe, I.; Kahn, P. C.; Waks, M. Unfolding and Refolding of Bovine Serum Albumin at Acid pH: Ultrasound and Structural Studies. *Biophys. J.* **2006**, *91*, 3397-3404.

(179) Dockal, M.; Carter, D. C.; Rüker, F. Conformational Transitions of the Three Recombinant Domains of Human Serum Albumin Depending on pH. *J. Biol. Chem.* **2000**, *275*, 3042-3050.

(180) Susa, A. C.; Xia, Z.; Tang, H. Y. H.; Tainer, J. A.; Williams, E. R. Charging of Proteins in Native Mass Spectrometry. *J. Am. Soc. Mass Spectrom.* **2017**, *28*, 332-340.

(181) Lanucara, F.; Holman, S. W.; Gray, C. J.; Eyers, C. E. The power of ion mobility-mass spectrometry for structural characterization and the study of conformational dynamics. *Nat. Chem.* **2014**, *6*, 281-294.

(182) Resemann, A.; Wunderlich, D.; Rothbauer, U.; Warscheid, B.; Leonhardt, H.; Fuchser, J.; Kuhlmann, K.; Suckau, D. Top-Down de Novo Protein Sequencing of a 13.6 kDa Camelid Single Heavy Chain Antibody by Matrix-Assisted Laser Desorption Ionization-Time-of-Flight/Time-of-Flight Mass Spectrometry. *Anal. Chem.* **2010**, *82*, 3283-3292.

(183) Siuti, N.; Roth, M. J.; Mizzen, C. A.; Kelleher, N. L.; Pesavento, J. J. Gene-Specific Characterization of Human Histone H2B by Electron Capture Dissociation. *J. Proteome Res.* **2006**, *5*, 233-239.

(184) Shaw, J. B.; Li, W.; Holden, D. D.; Zhang, Y.; Griep-Raming, J.; Fellers, R. T.; Early, B. P.; Thomas, P. M.; Kelleher, N. L.; Brodbelt, J. S. Complete Protein Characterization Using Top-Down Mass Spectrometry and Ultraviolet Photodissociation. *J. Am. Chem. Soc.* **2013**, *135*, 12646-12651.

(185) Zubarev, R. A.; Kelleher, N. L.; McLafferty, F. W. Electron Capture Dissociation of Multiply Charged Protein Cations. A Nonergodic Process. *J. Am. Chem. Soc.* **1998**, *120*, 3265-3266.

(186) Coon, J. J.; Shabanowitz, J.; Hunt, D. F.; Syka, J. E. P. Electron transfer dissociation of peptide anions. *J. Am. Soc. Mass Spectrom.* **2005**, *16*, 880-882.

(187) Reilly, J. P. Ultraviolet photofragmentation of biomolecular ions. *Mass Spectrom. Rev.* **2009**, *28*, 425-447.

(188) Schwartz, B. L.; Bruce, J. E.; Anderson, G. A.; Hofstadler, S. A.; Rockwood, A. L.; Smith, R. D.; Chilkoti, A.; Stayton, P. S. Dissociation of tetrameric ions of noncovalent streptavidin complexes formed by electrospray ionization. *J. Am. Soc. Mass Spectrom.* **1995**, *6*, 459-465.

(189) Sciuto, S. V.; Liu, J.; Konermann, L. An Electrostatic Charge Partitioning Model for the Dissociation of Protein Complexes in the Gas Phase. *J. Am. Soc. Mass Spectrom.* **2011**, *22*, 1679.

(190) Beardsley, R. L.; Jones, C. M.; Galhena, A. S.; Wysocki, V. H. Noncovalent Protein Tetramers and Pentamers with “n” Charges Yield Monomers with n/4 and n/5 Charges. *Anal. Chem.* **2009**, *81*, 1347-1356.

(191) Yan, J.; Zhou, M.; Gilbert, J. D.; Wolff, J. J.; Somogyi, Á.; Pedder, R. E.; Quintyn, R. S.; Morrison, L. J.; Easterling, M. L.; Paša-Tolić, L.; Wysocki, V. H. Surface-Induced Dissociation of Protein Complexes in a Hybrid Fourier Transform Ion Cyclotron Resonance Mass Spectrometer. *Anal. Chem.* **2017**, *89*, 895-901.

(192) Laskin, J.; Denisov, E. V.; Shukla, A. K.; Barlow, S. E.; Futrell, J. H. Surface-Induced Dissociation in a Fourier Transform Ion Cyclotron Resonance Mass Spectrometer: Instrument Design and Evaluation. *Anal. Chem.* **2002**, *74*, 3255-3261.

(193) Galhena, A. S.; Dagan, S.; Jones, C. M.; Beardsley, R. L.; Wysocki, V. H. Surface-Induced Dissociation of Peptides and Protein Complexes in a Quadrupole/Time-of-Flight Mass Spectrometer. *Anal. Chem.* **2008**, *80*, 1425-1436.

(194) Žabka, J.; Dolejšek, Z.; Herman, Z. Energy Partitioning in Collisions of Slow Polyatomic Ions with Surfaces: Ethanol Molecular Ions on Surfaces Covered by Self-Assembled Monolayers (CF-SAM, CH-SAM, COOH-SAM). *J. Phys. Chem. A* **2002**, *106*, 10861-10869.

(195) Laskin, J.; Futrell, J. H. On the efficiency of energy transfer in collisional activation of small peptides. *J. Chem. Phys.* **2002**, *116*, 4302-4310.

(196) Meroueh, O.; Hase, W. L. Dynamics of Energy Transfer in Peptide−Surface Collisions. *J. Am. Chem. Soc.* **2002**, *124*, 1524-1531.

(197) Pratihar, S.; Kohale, S. C.; Bhakta, D. G.; Laskin, J.; Hase, W. L. Dynamics of energy transfer and soft-landing in collisions of protonated dialanine with perfluorinated self-assembled monolayer surfaces. *Phys. Chem. Chem. Phys.* **2014**, *16*, 23769-23778.

(198) Raz, T.; Levine, R. D. Fast translational thermalization of extreme disequilibrium induced by cluster impact. *Chem. Phys.* **1996**, *213*, 263-275.

(199) Laskin, J.; Bailey, T. H.; Futrell, J. H. Shattering of Peptide Ions on Self-Assembled Monolayer Surfaces. *J. Am. Chem. Soc.* **2003**, *125*, 1625-1632.

(200) Meroueh, S. O.; Wang, Y.; Hase, W. L. Direct Dynamics Simulations of Collision- and Surface-Induced Dissociation of N-Protonated Glycine. Shattering Fragmentation. *J. Phys. Chem. A* **2002**, *106*, 9983-9992.

(201) Park, K.; Deb, B.; Song, K.; Hase, W. L. Importance of Shattering Fragmentation in the Surface-Induced Dissociation of Protonated Octaglycine. *J. Am. Soc. Mass Spectrom.* **2009**, *20*, 939-948.

(202) Hendell, E.; Even, U.; Raz, T.; Levine, R. D. Shattering of Clusters Upon Surface Impact: An Experimental and Theoretical Study. *Phys. Rev. Lett.* **1995**, *75*, 2670-2673.

(203) Raz, T.; Levine, R. D. On the shattering of clusters by surface impact heating. *J. Chem. Phys.* **1996**, *105*, 8097-8102.

(204) Beck, R. D.; Warth, C.; May, K.; Kappes, M. M. Surface impact induced shattering of C6. Detection of small Cm fragments by negative surface ionization. *Chem. Phys. Lett.* **1996**, *257*, 557-562.

(205) Schultz, D. G.; Hanley, L. Shattering of SiMe3+ during surface-induced dissociation. *J. Chem. Phys.* **1998**, *109*, 10976-10983.

(206) Marzluff, E. M.; Campbell, S.; Rodgers, M. T.; Beauchamp, J. L. Collisional Activation of Large Molecules Is an Efficient Process. *J. Am. Chem. Soc.* **1994**, *116*, 6947-6948.

(207) Mortensen, D. N.; Susa, A. C.; Williams, E. R. Collisional Cross-Sections with T-Wave Ion Mobility Spectrometry without Experimental Calibration. *J. Am. Soc. Mass Spectrom.* **2017**, *28*, 1282-1292.

(208) Nesatyy, V. J.; Laskin, J. Dissociation of noncovalent protein complexes by triple quadrupole tandem mass spectrometry: comparison of Monte Carlo simulation and experiment. *Int. J. Mass Spectrom.* **2002**, *221*, 245-262.

(209) Douglas, D. J. Applications of Collision Dynamics in Quadrupole Mass Spectrometry. *J. Am. Soc. Mass Spectrom.* **1998**, *9*, 101-113.

(210) Hoxha, A.; Collette, C.; De Pauw, E.; Leyh, B. Mechanism of Collisional Heating in Electrospray Mass Spectrometry: Ion Trajectory Calculations. *J. Phys. Chem. A* **2001**, *105*, 7326-7333.

(211) Uggerud, E.; Derrick, P. J. Theory of collisional activation of macromolecules. Impulsive collisions of organic ions. *J. Phys. Chem.* **1991**, *95*, 1430-1436.

(212) Adamson, B. D.; Miller, M. E. C.; Continetti, R. E. The aerosol impact spectrometer: a versatile platform for studying the velocity dependence of nanoparticle-surface impact phenomena. *EPJ Tech. Instrum.* **2017**, *4*, 2.

(213) Han, L.; Hyung, S.-J.; Mayers, J. J. S.; Ruotolo, B. T. Bound Anions Differentially Stabilize Multiprotein Complexes in the Absence of Bulk Solvent. *J. Am. Chem. Soc.* **2011**, *133*, 11358-11367.

(214) Han, L.; Hyung, S.-J.; Ruotolo, B. T. Bound Cations Significantly Stabilize the Structure of Multiprotein Complexes in the Gas Phase. *Angew. Chem., Int. Ed.* **2012**, *51*, 5692-5695.

(215) Freeke, J.; Robinson, C. V.; Ruotolo, B. T. Residual counter ions can stabilise a large protein complex in the gas phase. *Int. J. Mass Spectrom.* **2010**, *298*, 91-98.

(216) Wagner, N. D.; Kim, D.; Russell, D. H. Increasing Ubiquitin Ion Resistance to Unfolding in the Gas Phase Using Chloride Adduction: Preserving More “Native-Like” Conformations Despite Collisional Activation. *Anal. Chem.* **2016**, *88*, 5934-5940.

(217) Meroueh, O.; Hase, W. L. Energy transfer pathways in the collisional activation of peptides. *Int. J. Mass Spectrom.* **2000**, *201*, 233-244.

(218) Baer, T.; Hase, W. L.; Hase, W. L.; Hase, W. L. *Unimolecular Reaction Dynamics: Theory and Experiments*; Oxford University Press, USA, 1996.

(219) Quintyn, R. S.; Zhou, M.; Yan, J.; Wysocki, V. H. Surface-Induced Dissociation Mass Spectra as a Tool for Distinguishing Different Structural Forms of Gas-Phase Multimeric Protein Complexes. *Anal. Chem.* **2015**, *87*, 11879-11886.

(220) Pratihar, S.; Kohale, S. C.; Vázquez, S. A.; Hase, W. L. Intermolecular Potential for Binding of Protonated Peptide Ions with Perfluorinated Hydrocarbon Surfaces. *J. Phys. Chem. B* **2014**, *118*, 5577-5588.

(221) Zhou, M.; Politis, A.; Davies, R. B.; Liko, I.; Wu, K.-J.; Stewart, A. G.; Stock, D.; Robinson, C. V. Ion mobility–mass spectrometry of a rotary ATPase reveals ATP-induced reduction in conformational flexibility. *Nat. Chem.* **2014**, *6*, 208-215.

(222) Allison, T. M.; Reading, E.; Liko, I.; Baldwin, A. J.; Laganowsky, A.; Robinson, C. V. Quantifying the stabilizing effects of protein–ligand interactions in the gas phase. *Nat. Commun.* **2015**, *6*, 8551.

(223) Wagner, N. D.; Clemmer, D. E.; Russell, D. H. ESI-IM-MS and Collision-Induced Unfolding That Provide Insight into the Linkage-Dependent Interfacial Interactions of Covalently Linked Diubiquitin. *Anal. Chem.* **2017**, *89*, 10094-10103.

(224) Laganowsky, A.; Reading, E.; Allison, T. M.; Ulmschneider, M. B.; Degiacomi, M. T.; Baldwin, A. J.; Robinson, C. V. Membrane proteins bind lipids selectively to modulate their structure and function. *Nature* **2014**, *510*, 172-175.

(225) Wysocki, V. H.; Kenttämaa, H. I.; Cooks, R. G. Internal energy distributions of isolated ions after activation by various methods. *Int. J. Mass Spectrom. Ion Processes* **1987**, *75*, 181-208.

(226) Leib, R. D.; Donald, W. A.; Bush, M. F.; O'Brie, J. T.; Williams, E. R. Internal Energy Deposition in Electron Capture Dissociation Measured Using Hydrated Divalent Metal Ions as Nanocalorimeters. *J. Am. Chem. Soc.* **2007**, *129*, 4894-4895.

(227) Donald, W. A.; Williams, E. R. Measuring the extent and width of internal energy deposition in ion activation using nanocalorimetry. *J. Am. Soc. Mass Spectrom.* **2010**, *21*, 615-625.

(228) Collette, C.; De Pauw, E. Calibration of the internal energy distribution of ions produced by electrospray. *Rapid Commun. Mass Spectrom.* **1998**, *12*, 165-170.

(229) Derwa, F.; de Pauw, E.; Natalis, P. New basis for a method for the estimation of secondary ion internal energy distribution in 'soft' ionization techniques. *Org. Mass Spectrom.* **1991**, *26*, 117-118.

(230) Rahrt, R.; Auth, T.; Demireva, M.; Armentrout, P. B.; Koszinowski, K. Benzhydrylpyridinium Ions: A New Class of Thermometer Ions for the Characterization of Electrospray-Ionization Mass Spectrometers. *Anal. Chem.* **2019**, *91*, 11703-11711.

(231) Sztáray, J.; Memboeuf, A.; Drahos, L.; Vékey, K. Leucine enkephalin—A mass spectrometry standard. *Mass Spectrom. Rev.* **2011**, *30*, 298-320.

(232) Gabelica, V.; De Pauw, E.; Karas, M. Influence of the capillary temperature and the source pressure on the internal energy distribution of electrosprayed ions. *Int. J. Mass Spectrom.* **2004**, *231*, 189-195.

(233) Price, W. D.; Jockusch, R. A.; Williams, E. R. Is Arginine a Zwitterion in the Gas Phase? *J. Am. Chem. Soc.* **1997**, *119*, 11988-11989.

(234) Price, W. D.; Jockusch, R. A.; Williams, E. R. Binding Energies of Protonated Betaine Complexes: A Probe of Zwitterion Structure in the Gas Phase. *J. Am. Chem. Soc.* **1998**, *120*, 3474-3484.

(235) Donor, M. T.; Mroz, A. M.; Prell, J. S. Experimental and theoretical investigation of overall energy deposition in surface-induced unfolding of protein ions. *Chem. Sci.* **2019**, *10*, 4097-4106.

(236) Allen, S. J.; Schwartz, A. M.; Bush, M. F. Effects of Polarity on the Structures and Charge States of Native-Like Proteins and Protein Complexes in the Gas Phase. *Anal. Chem.* **2013**, *85*, 12055-12061.

(237) Steinfeld, J. I.; Francisco, J. S.; Hase, W. L. *Chemical kinetics and dynamics*, 2nd ed.; Prentice Hall: Upper Saddle River, N.J., 1999.

(238) Haynes, S. E.; Polasky, D. A.; Dixit, S. M.; Majmudar, J. D.; Neeson, K.; Ruotolo, B. T.; Martin, B. R. Variable-Velocity Traveling-Wave Ion Mobility Separation Enhancing Peak Capacity for Data-Independent Acquisition Proteomics. *Anal. Chem.* **2017**, *89*, 5669-5672.

(239) Hong, S.; Bush, M. F. Collision-Induced Unfolding Is Sensitive to the Polarity of Proteins and Protein Complexes. *J. Am. Soc. Mass Spectrom.* **2019**.

(240) Bythell, B. J.; Suhai, S.; Somogyi, Á.; Paizs, B. Proton-Driven Amide Bond-Cleavage Pathways of Gas-Phase Peptide Ions Lacking Mobile Protons. *J. Am. Chem. Soc.* **2009**, *131*, 14057-14065.

(241) Zhou, M.; Liu, W.; Shaw, J. B. Charge Movement and Structural Changes in the Gas-Phase Unfolding of Multimeric Protein Complexes Captured by Native Top-Down Mass Spectrometry. *Anal. Chem.* **2019**.

(242) Miller, Z. M.; Zhang, J. D.; Donald, W. A.; Prell, J. S. Gas-Phase Protonation Thermodynamics of Biological Lipids: Experiment, Theory, and Implications. *Anal. Chem.* **2020**, in revision.

(243) Marcoux, J.; Robinson, Carol V. Twenty Years of Gas Phase Structural Biology. *Structure* **2013**, *21*, 1541-1550.

(244) Hooker, B. S.; Bigelow, D. J.; Lin, C.-T. Methods for mapping of interaction networks involving membrane proteins. *Biochemical and Biophysical Research Communications* **2007**, *363*, 457-461.

(245) Barrera, N. P.; Di Bartolo, N.; Booth, P. J.; Robinson, C. V. Micelles Protect Membrane Complexes from Solution to Vacuum. *Science* **2008**, *321*, 243-246.

(246) Landreh, M.; Liko, I.; Uzdavinys, P.; Coincon, M.; Hopper, J. T. S.; Drew, D.; Robinson, C. V. Controlling release, unfolding and dissociation of membrane protein complexes in the gas phase through collisional cooling. *Chem. Commun.* **2015**, *51*, 15582-15584.

(247) Walker, L. R.; Marzluff, E. M.; Townsend, J. A.; Resager, W. C.; Marty, M. T. Native Mass Spectrometry of Antimicrobial Peptides in Lipid Nanodiscs Elucidates Complex Assembly. *Anal. Chem.* **2019**, *91*, 9284-9291.

(248) Marty, M. T.; Wilcox, K. C.; Klein, W. L.; Sligar, S. G. Nanodisc-solubilized membrane protein library reflects the membrane proteome. *Anal. Bioanal. Chem.* **2013**, *405*, 4009-4016.

(249) Marty, M. T.; Hoi, K. K.; Gault, J.; Robinson, C. V. Probing the Lipid Annular Belt by Gas-Phase Dissociation of Membrane Proteins in Nanodiscs. *Angew. Chem.-Int. Edit.* **2016**, *55*, 550-554.

(250) Laganowsky, A.; Reading, E.; Hopper, J. T. S.; Robinson, C. V. Mass Spectrometry of Intact Membrane Protein Complexes. *Nat. Protoc.* **2013**, *8*, 639-651.

(251) Zhou, M.; Morgner, N.; Barrera, N. P.; Politis, A.; Isaacson, S. C.; Matak-Vinkovic, D.; Murata, T.; Bernal, R. A.; Stock, D.; Robinson, C. V. Mass Spectrometry of Intact V-Type ATPases Reveals Bound Lipids and the Effects of Nucleotide Binding. *Science* **2011**, *334*, 380-385.

(252) Barrera, N. P.; Robinson, C. V. Advances in the Mass Spectrometry of Membrane Proteins: From Individual Proteins to Intact Complexes. *Annu. Rev. Biochem.* **2011**, *80*, 247-271.

(253) Gupta, K.; Li, J.; Liko, I.; Gault, J.; Bechara, C.; Wu, D.; Hopper, J. T. S.; Giles, K.; Benesch, J. L. P.; Robinson, C. V. Identifying key membrane protein lipid interactions using mass spectrometry. *Nat. Protoc.* **2018**, *13*, 1106-1120.

(254) Lee, A. G. Biological membranes: the importance of molecular detail. *Trends Biochem. Sci.* **2011**, *36*, 493-500.

(255) Poveda, J. A.; Giudici, A. M.; Renart, M. L.; Molina, M. L.; Montoya, E.; Fernández-Carvajal, A.; Fernández-Ballester, G.; Encinar, J. A.; González-Ros, J. M. Lipid modulation of ion channels through specific binding sites. *Biochimica et Biophysica Acta (BBA) - Biomembranes* **2014**, *1838*, 1560-1567.

(256) Bogdanov, M.; Dowhan, W.; Vitrac, H. Lipids and topological rules governing membrane protein assembly. *Biochimica et Biophysica Acta (BBA) - Molecular Cell Research* **2014**, *1843*, 1475-1488.

(257) Saliba, A.-E.; Vonkova, I.; Gavin, A.-C. The systematic analysis of protein–lipid interactions comes of age. *Nat. Rev. Mol. Cell Biol.* **2015**, *16*, 753-761.

(258) Patrick, J. W.; Boone, C. D.; Liu, W.; Conover, G. M.; Liu, Y.; Cong, X.; Laganowsky, A. Allostery revealed within lipid binding events to membrane proteins. *Proc. Natl. Acad. Sci. U. S. A.* **2018**, *115*, 2976-2981.

(259) Cong, X.; Liu, Y.; Liu, W.; Liang, X.; Russell, D. H.; Laganowsky, A. Determining Membrane Protein–Lipid Binding Thermodynamics Using Native Mass Spectrometry. *J. Am. Chem. Soc.* **2016**, *138*, 4346-4349.

(260) Kitova, E. N.; El-Hawiet, A.; Schnier, P. D.; Klassen, J. S. Reliable Determinations of Protein–Ligand Interactions by Direct ESI-MS Measurements. Are We There Yet? *J. Am. Soc. Mass Spectrom.* **2012**, *23*, 431-441.

(261) Li, M.; Guha, S.; Zangmeister, R.; Tarlov, M. J.; Zachariah, M. R. Quantification and Compensation of Nonspecific Analyte Aggregation in Electrospray Sampling. *Aerosol Science and Technology* **2011**, *45*, 849-860.

(262) Sun, J.; Kitova, E. N.; Sun, N.; Klassen, J. S. Method for Identifying Nonspecific Protein−Protein Interactions in Nanoelectrospray Ionization Mass Spectrometry. *Anal. Chem.* **2007**, *79*, 8301-8311.

(263) Kitov, P. I.; Han, L.; Kitova, E. N.; Klassen, J. S. Sliding Window Adduct Removal Method (SWARM) for Enhanced Electrospray Ionization Mass Spectrometry Binding Data. *J. Am. Soc. Mass Spectrom.* **2019**, *30*, 1446-1454.

(264) Roscioli, J. R.; McCunn, L. R.; Johnson, M. A. Quantum Structure of the Intermolecular Proton Bond. *Science* **2007**, *316*, 249-254.

(265) Hunter, E. P. L.; Lias, S. G. Evaluated Gas Phase Basicities and Proton Affinities of Molecules: An Update. *Journal of Physical and Chemical Reference Data* **1998**, *27*, 413-656.

(266) May, J. C.; Russell, D. H. A Mass-Selective Variable-Temperature Drift Tube Ion Mobility-Mass Spectrometer for Temperature Dependent Ion Mobility Studies. *J. Am. Soc. Mass Spectrom.* **2011**, *22*, 1134.

(267) Ujma, J.; Giles, K.; Morris, M.; Barran, P. E. New High Resolution Ion Mobility Mass Spectrometer Capable of Measurements of Collision Cross Sections from 150 to 520 K. *Anal. Chem.* **2016**, *88*, 9469-9478.